In-Plane Seismic Capacity of Interlocking CSEB and Fired Clay Brick Masonry Piers: A Comparative Numerical Study

Cornelia Lydin & Ingrid Johansson

Division of Structural Engineering
LTH, Faculty of Engineering
Lund University, 2026

TVBK-5313

Abstract

Nepal is located in one of the most seismically active regions in the world, and the 2015 Gorkha earthquake clearly demonstrated the vulnerability of non-engineered masonry buildings. In the reconstruction efforts following the earthquake, interlocking Compressed Stabilised Earth Blocks (CSEB) have been highlighted as a potentially more seismically robust and at the same time more sustainable alternative to conventional fired clay brick masonry. Despite practical experience from their use, systematic engineering comparisons between interlocking CSEB and fired clay brick masonry under comparable conditions remain limited.

In this master's thesis, the in-plane seismic response of masonry wall panels, also referred to as piers, made of interlocking CSEB and fired clay brick is compared through non-linear finite element analyses. The models were developed in ABAQUS using detailed micro-modelling, in which all materials were modelled explicitly and contacts and interactions allowed separation, re-contact, and sliding. The piers were analysed using static displacement-controlled pushover analyses. Two idealised support conditions were considered: cantilever and fixed at both ends. These were chosen to represent limited and strong restraint at the top of the wall, respectively. The effect of vertical pre-compression is examined through one low and one high pre-compression level, and selected cases also include vertical reinforcement based on the principles of the Nepal Building Code (NBC).

The results are presented in the form of pushover curves (base shear, V, versus top lateral displacement) and through interpretation of damage patterns and governing failure mechanisms. The comparison shows how geometry (slenderness), support conditions, and pre-compression influence capacity, stiffness, drift capacity, ductility, energy absorption, and governing failure mechanisms, including the difference between shear-dominated mechanisms (diagonal localisation) and flexural- or rocking-dominated mechanisms. The influence of reinforcement is discussed in terms of how it modifies the failure process and post-peak response, and how this relates to the prescriptive recommendations in the NBC. Overall, the study provides a mechanistic basis at pier level for understanding the differences between the systems and for guiding continued work towards building-level analysis and future validation against experimental data.

Sammanfattning

Nepal ligger i ett av världens mest jordbävningsutsatta områden, och jordbävningen i Gorkha 2015 visade tydligt hur sårbara murverksbyggnader utan ingenjörsmässig dimensionering kan vara. I återuppbyggnadsarbetet har interlocking Compressed Stabilised Earth Blocks (CSEB) lyfts fram som ett möjligt alternativ till traditionellt murverk av bränt lertegel. Detta eftersom systemet både kan vara mer motståndskraftigt vid jordbävning och mer hållbart ur miljösynpunkt. Trots detta finns fortfarande få systematiska ingenjörsmässiga jämförelser mellan interlocking CSEB och konventionellt tegelmurverk under likvärdiga förutsättningar.

I detta examensarbete jämförs den seismiska responsen i planet hos vertikala väggpartier av interlocking CSEB respektive bränt lertegel. Jämförelsen genomförs med hjälp av icke-linjära analyser med finita elementmetoden. Modellerna utvecklades i ABAQUS med detaljerad mikromodellering, där samtliga material modellerades separat och där kontakter och interaktioner gjorde det möjligt att beskriva separering, återkontakt och glidning mellan olika delar. Väggpartierna analyserades med statiska pushover-analyser under en förskjutningskontroll. Två idealiserade upplagsfall studerades: konsolfall samt väggar inspända i båda ändar. Dessa valdes för att representera begränsad respektive stark fasthållning vid väggens överkant. Effekten av vertikal förkompression undersöks genom en låg och en hög lastnivå, och i utvalda fall inkluderas även vertikal armering enligt principerna i Nepal Building Code (NBC).

Resultaten redovisas med last-förskjutningskurvor från pushover-analyserna, där basskjuvkraften relateras till lateral toppförskjutning, samt genom tolkning av skademönster och dominerande brottmekanismer. Jämförelsen visar hur geometri, upplagsförhållanden och förkompression påverkar kapacitet, styvhet, deformationsförmåga, duktilitet, energiabsorption och dominerande brottmekanismer. Särskild uppmärksamhet riktas mot skillnaden mellan skjuvdominerade mekanismer med diagonal sprickbildning och böj- eller vältningsdominerade mekanismer. Armeringens inverkan diskuteras utifrån hur den förändrar brottförloppet och beteendet efter maximal last, samt hur detta förhåller sig till de preskriptiva rekommendationerna i NBC. Sammantaget ger studien ett mekanistiskt underlag på väggpartinivå för att förstå skillnader mellan systemen och för att vägleda fortsatt arbete på byggnadsnivå samt framtida validering mot experimentella resultat.

Acknowledgements

We would like to express our sincere gratitude to Engineers Without Borders for giving us the opportunity to carry out this thesis in collaboration with them.

We would also like to thank Aavash Shrestha at Build up Nepal for his valuable help with the experimental work, including the testing of the materials used in this study.

Special thanks go to our supervisor, Leandro Iannacone, for his guidance throughout the project, for his constructive feedback, and for the many valuable ideas that helped shape the work.

Finally, we would like to thank our families for their patience, support, and encouragement during this period.

Notations and Symbols

Latin symbols

A - cross-sectional area
d_c - compressive damage variable (CDP)
d_t - tensile damage variable (CDP)
$d_{\max}$ - maximum capped damage value used for numerical stability
E - Young's modulus
E_0 - initial (undamaged) Young's modulus
E_c - unloading-reloading modulus in compression
E_t - unloading-reloading modulus in tension
E_{abs} - absorbed energy (area under the force-displacement curve up to the adopted failure point)
F - yield function (CDP)
f_c - compressive strength
G - plastic potential function (CDP)
G_f - fracture energy
G_s - shear modulus
g - gravitational acceleration
h_{pier} - pier height
h_m - mortar joint thickness
K_c - CDP deviatoric-plane shape parameter
K_{nn} - normal interface stiffness
K_{ss} - tangential interface stiffness in shear direction 1
K_{tt} - tangential interface stiffness in shear direction 2
p - hydrostatic pressure / mean stress / compressive contact pressure (depending on context)
q - von Mises equivalent stress
q_{tot} - total vertical line load per unit wall length
RF - reaction force at the loading reference point
t - thickness
t_n - normal traction at an interface
t_s - tangential traction at an interface (direction 1)
t_t - tangential traction at an interface (direction 2)
u - displacement
u_y - yield displacement used in ductility evaluation
u_f - failure/ultimate displacement used in ductility evaluation
$u_{\max}$ - drift-based displacement limit
U - displacement output variable in ABAQUS
V - lateral reaction force / base shear from the pushover curve
V_p - peak lateral load
V_{80} - lateral load corresponding to 80% of the peak load on the descending branch

Greek symbols

Δ_p - lateral displacement at peak load V_p
Δ_f - lateral displacement at the adopted failure point
δ_n - normal separation at an interface
δ_s - tangential slip at an interface (direction 1)
δ_t - tangential slip at an interface (direction 2)
ϵ - eccentricity parameter in the CDP plastic potential
ε - strain
$\varepsilon_{\mathrm{ax}}$ - axial strain
$\varepsilon_{\mathrm{lat}}$ - lateral strain
ε_t - total tensile strain
ε_c - total compressive strain
ε_t^{ck} - tensile cracking strain (CDP convention)
ε_c^{in} - compressive inelastic strain (CDP convention)
ε_0^{el} - elastic strain of undamaged material
ε_{0t}^{el} - elastic tensile strain of undamaged material
ε_{0c}^{el} - elastic compressive strain of undamaged material
ε_t^p - plastic strain in tension (CDP convention)
ε_c^p - plastic strain in compression (CDP convention)
μ - displacement ductility
μ_f - friction coefficient (Coulomb)
μ_v - viscosity parameter in CDP
ν - Poisson's ratio
ρ - density
σ - uniaxial stress
σ_t - uniaxial tensile stress
σ_c - uniaxial compressive stress
σ_{t0} - peak tensile strength
σ_{cu} - peak compressive strength
$\sigma_{\max}$ - maximum principal effective stress
σ_{b0}/σ_{c0} - biaxial-to-uniaxial compressive yield stress ratio (CDP)
τ - interface shear traction
θ_f - drift at failure
θ_{lim} - adopted drift limit
ψ - dilation angle
φ - internal friction angle

Contents

1 Introduction

1.1 Background

Nepal is located in one of the most seismically active regions in the world. On 25 April 2015, the Gorkha earthquake struck central Nepal with a moment magnitude of M_w 7.8, followed by a major aftershock of M_w 7.3 on 12 May (Rastogi, 2024). The event highlighted the vulnerability of Nepal's building stock and the need for safer construction methods. It caused severe human and material losses, with around 800,000 houses destroyed or damaged in total (Government of Nepal, National Planning Commission et al., 2015).

The earthquake also showed the consequences of widespread structural vulnerability. Many masonry buildings in Nepal have historically been constructed with limited seismic detailing, which increases their vulnerability during strong earthquakes (Government of Nepal, National Planning Commission et al., 2015; Shrestha, 2012b). This makes the question of safer and more robust wall systems especially relevant.

After the earthquake, reconstruction became a major priority. This created a need not only to rebuild damaged housing, but also to identify construction methods that could be safer, more affordable, and suitable for rural contexts. Build up Nepal (BUN) was established in this post-earthquake context and works with low-cost, earthquake-resistant construction using locally available resources (Build Up Nepal (BUN), n.d.).

The construction system promoted by Build up Nepal is based on interlocking Compressed Stabilised Earth Blocks (CSEB), also referred to by the organisation as interlocking eco-bricks (Build Up Nepal (BUN), 2026). These blocks are produced from local soil- or sand-based materials with a limited cement content. They are stacked in an interlocking pattern and include vertical channels for grout and reinforcement. The system is intended to simplify construction, reduce dependence on fired clay bricks, and make safer masonry construction more accessible in rural areas (Build Up Nepal (BUN), n.d. 2026).

Since fired clay brick masonry remains a common construction method in Nepal, it is relevant to compare the structural response of interlocking CSEB and fired brick masonry under similar conditions. Although CSEB has received increasing attention in Nepal, systematic engineering comparisons between interlocking CSEB and fired clay brick masonry under equivalent idealised seismic loading conditions are still limited. This creates a clear motivation for a comparative numerical study.

1.2 Aim

The aim of this thesis was to investigate whether interlocking Compressed Stabilised Earth Block (CSEB) masonry can provide a more favourable in-plane seismic response than conventional fired clay brick masonry. The study was based on a practical question relevant to Build up Nepal, namely whether CSEB walls can be expected to perform better than fired brick walls when subjected to earthquake loading.

Since this broad question could not be studied at full building scale within the scope of the project, the work was limited to numerical analyses of masonry piers under a small number of idealised conditions. The wall systems were compared in terms of lateral load capacity, deformation capacity, energy absorption, and governing failure modes, while also considering the influence of wall slenderness, boundary conditions, and vertical pre-compression. A limited set of reinforced CSEB cases was also included, based on the vertical reinforcement detailing recommended by Build up Nepal.

The intention is that the findings from this study can support future numerical and experimental work at the building scale by providing improved understanding of governing response mechanisms at the pier/wall level. The work should therefore primarily be understood as a comparative numerical investigation of wall systems, material behaviour, and boundary conditions, rather than as a complete design method or a validation of reinforced CSEB construction in general.

1.2.1 Research questions

1. Under the studied idealised pier-level conditions, does interlocking CSEB masonry, with and without vertical steel reinforcment, show a more favourable in-plane seismic response than conventional fired clay brick masonry in terms of lateral load capacity, deformation capacity, energy absorption, and failure mode?

2. How do slenderness, boundary conditions, and pre-compression influence lateral load capacity, deformation capacity, energy absorption, and governing failure mode in the studied pier configurations?

3. How does the inclusion of a selected vertical steel reinforcement layout affect the response of the studied CSEB piers, and what indications does this provide regarding the role of reinforcement in these wall configurations?

1.3 Limitations and scope

This study is limited to detailed finite element analyses of isolated masonry piers/wall panels in order to capture local in-plane failure mechanisms. The results therefore describe behaviour at pier level and should not be interpreted as a full seismic assessment of an entire building system. Global structural behaviour such as diaphragm action, box action, torsional effects, wall-to-wall interaction, and full three-dimensional

response are not included explicitly. In the same way, only in-plane behaviour is considered, which means that out-of-plane instability, overturning of complete wall assemblies, and combined in-plane/out-of-plane interaction fall outside the scope of the work.

The loading was idealised through static displacement-controlled pushover analysis. The models therefore do not capture the effects of realistic cyclic earthquake loading. The study is further restricted to a limited number of wall typologies and modelling assumptions, namely squat and slender pier geometries, two idealised boundary conditions (cantilever and fixed-fixed), and two vertical pre-compression levels.

The reinforced part of the study is also limited in scope. Only one selected vertical reinforcement layout was investigated in the CSEB system. Since only the reinforcement arrangement recommended and used by Build up Nepal was studied, the reinforced results should primarily be interpreted as representative of this specific configuration. However, they still provide an indication of how vertical reinforcement may influence the response of the studied wall types more generally. Other reinforcement ratios, bar diameters, layouts, anchorage details, horizontal bands, and alternative detailing strategies were not investigated within the scope of the thesis.

In addition, the constitutive descriptions and interface models are idealised. Material parameters are based on available tests, literature data, and engineering assumptions, and not all input parameters were calibrated against dedicated experiments for the exact masonry systems studied. In particular, tensile properties, interface behaviour, and bond conditions remain important sources of uncertainty. Construction-related variability was also not modelled explicitly. Variations in workmanship, geometric imperfections, joint thickness, unit quality, curing conditions, and local defects are instead treated qualitatively as possible sources of uncertainty.

The results should therefore primarily be interpreted comparatively, that is, as a basis for understanding relative differences in response and governing mechanisms between the studied systems, rather than as exact predictions of full-scale structural performance.

2 Theoretical framework

2.1 Earthquakes

An earthquake is a sudden ground motion that occurs when accumulated stresses in the Earth's crust are rapidly released, typically through rupture or sliding along a fault (Nationalencyklopedin, n.d).

2.1.1 The Earth's inner structure

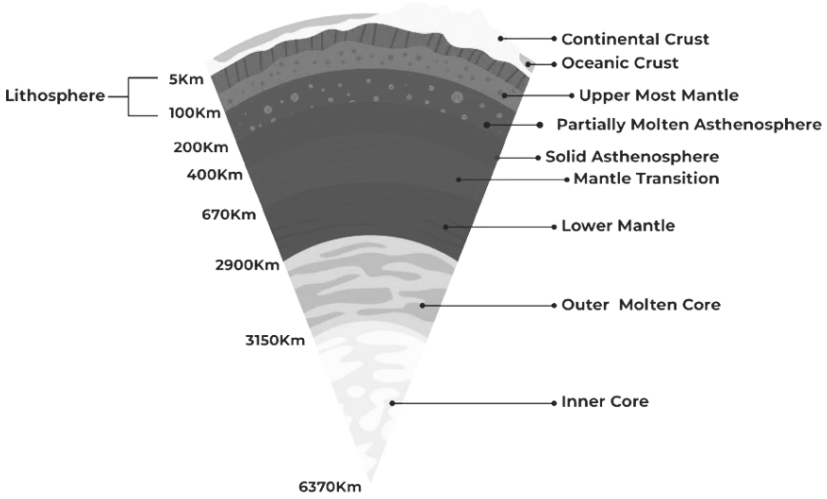

Figure 2.1: Illustration of the Earth's inner structure (Azevedo and Hagen, 2025).

To understand how earthquakes occur and the mechanisms behind them, it is necessary to first describe the structure of the Earth. Simplified, Earth can be divided into three main layers: the core, the mantle, and the crust (SGU, 2020). The core constitutes the innermost part and consists of a solid inner core and a liquid outer core (see 2.1), composed primarily of iron and nickel. Above the core lies the mantle, which is the thickest layer. The mantle is predominantly solid, but near the crust and the core it exhibits more plastic properties. These plastic properties form the basis for the movements associated with plate tectonics. Finally comes the crust, the outermost layer that forms the solid surface where all life and human activity take place (SGU, 2020). The crust, together with the upper part of the mantle, forms the lithosphere (see Figure 2.1). This layer is divided into a number of tectonic plates that continuously move relative to one another, (see Figure 2.2).

In summary, it is the movements of the tectonic plates within the lithosphere that generate the stresses and enable the fracture processes responsible for most earthquakes. The following section describes the main types of earthquakes.

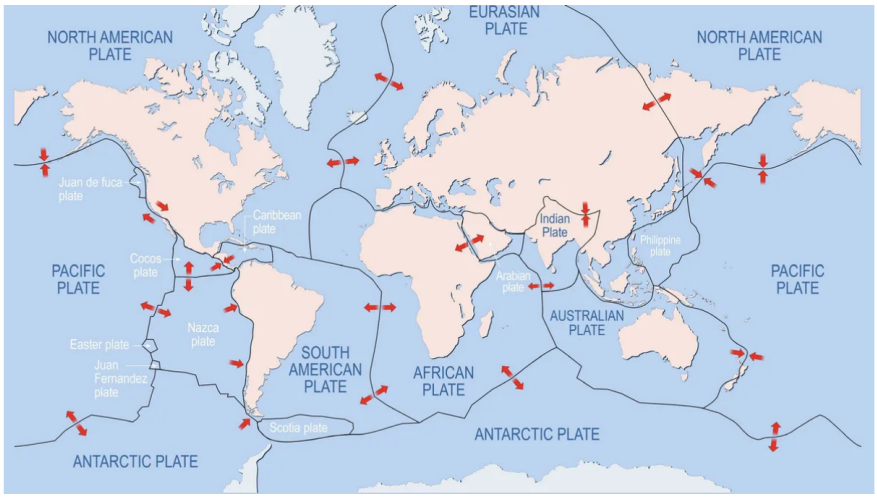

Figure 2.2: Tectonic plates of the Earth. Source: Bryce (2023), image credit: iStock/Getty Images Plus.

2.1.2 Types of earthquakes

Earthquakes can primarily be divided into three types: tectonic, volcanic, and induced (Maïni, 2005; Shrestha, 2012b).

Tectonic earthquakes are the most common and at the same time the most destructive type (Maïni, 2005; Shrestha, 2012b). They occur as a result of plate movements. When tectonic plates collide, separate, or slide past one another, stress gradually builds up in the bedrock. Because the bedrock has plastic properties, it can store large amounts of energy over long periods before failure occurs. Once the stresses exceed the strength of the Earth's crust, the stored energy is suddenly released in the form of seismic waves, resulting in an earthquake (Maïni, 2005; Shrestha, 2012b).

Volcanic earthquakes, on the other hand, are caused by magma movements beneath the Earth's crust (Maïni, 2005; Shrestha, 2012b). They can occur when rising magma pushes against or fractures the surrounding rock. Volcanic earthquakes may also develop when underground cavities formed by magma movements collapse, after volcanic eruptions, or due to shallow explosions. In general, volcanic earthquakes are more local and significantly less destructive than tectonic earthquakes (Maïni, 2005; Shrestha, 2012b).

Induced earthquakes are caused by human activities rather than natural geological processes. These earthquakes are less destructive than the previously mentioned types (Maïni, 2005; Shrestha, 2012b). They may occur, for example, near large dams, where the weight of the water alters the stress conditions in the bedrock, or in connection with extensive mining and tunneling that leads to the collapse of underground voids. Powerful explosions, such as underground nuclear tests, can also trigger local earthquakes (Shrestha, 2012b).

Despite differences in how they originate, the common denominator is that all types lead to a sudden release of energy in the Earth's crust, which propagates in the form of seismic waves.

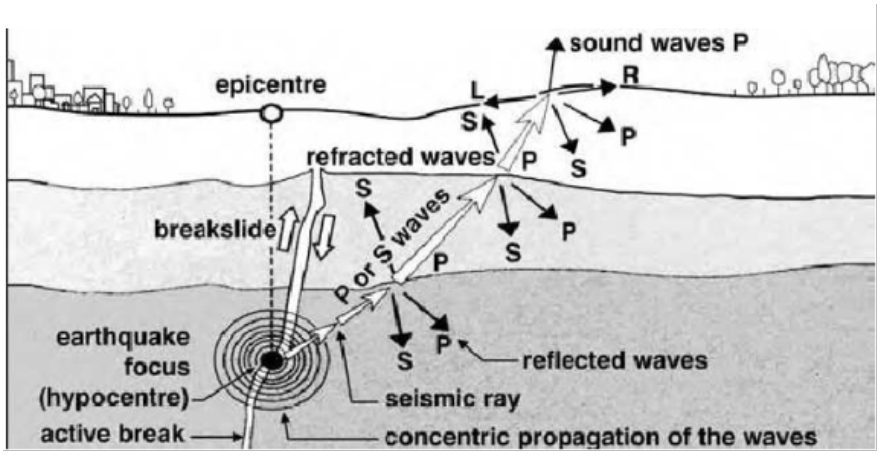

Figure 2.3: Schematic illustration of seismic wave propagation from the hypocentre, including the epicentre, body waves, and surface waves (Shrestha, 2012b).

2.1.3 Seismic waves

Seismic waves are generated when a rupture occurs in the Earth's crust, and the stored energy is released (Shrestha, 2012b). The place where this happens is called the hypocentre or focus (see Figure 2.3). The location on the ground surface directly above the focus is called the epicenter (Maïni, 2005). Shaking is usually experienced as strongest at the epicenter.

From the hypocentre, the waves propagate through the ground and are divided into two main groups: body waves, which travel through the interior of the Earth, and surface waves, which propagate along the surface (Tomaževič, 1999).

Body waves

Body waves can be divided into P-waves and S-waves. P-waves, or primary waves, are compressional waves in which the ground is pushed together and pulled apart in the direction of the wave's propagation (Maïni, 2005; Shrestha, 2012b). Primary waves have the highest velocity, between 5 and 8 km/s, and can travel through solids, liquids, and gasses (Encyclopaedia Britannica Editors, 2025). In the air, they behave in the same way as sound waves. S-waves are shear waves in which the ground moves perpendicular to the direction of propagation. These waves are slower, travelling at about 3 to 5 km/s, but can cause more damage because they induce a strong lateral ground motion (Maïni, 2005; Shrestha, 2012b). Unlike P waves, S waves can propagate only through solid materials (Encyclopaedia Britannica Editors, 2025).

Surface waves

When body waves reach the surface of the Earth, part of the energy is converted to the surface (Maïni, 2005; Shrestha, 2012b). These waves are often experienced as the most destructive because they act directly on the ground surface. Love waves

(L-waves) cause the ground to move horizontally from side to side, perpendicular to the direction of wave propagation, and have approximately the same velocity as S-waves. Rayleigh waves (R-waves), on the other hand, generate an elliptical motion in the ground, with both vertical and horizontal components. They are slightly slower than S-waves but are highly damaging to buildings because of their combined motion pattern (Swiss Seismological Service, n.d).

For buildings, it is not the specific types of seismic waves that are of primary importance, but rather the ground motion they generate at a given location, since this ground motion governs the response of the structure. The following section describes how earthquakes are measured and how their "intensity" is expressed in engineering terms.

2.1.4 Measurements of Earthquakes

Earthquakes are commonly described both by their size at the source (magnitude) and by the shaking they produce at a specific site (intensity or ground motion) (Shrestha, 2012b). For structural response and seismic design, the site-specific ground motion is the more important parameter, since it directly governs inertial forces and deformation demand.

Instrumental measures of site shaking commonly include peak values such as Peak Ground Acceleration (PGA) and Peak Ground Velocity (PGV). PGA is defined as

$$\mathrm{PGA} = \max |a(t)| \tag{2.1}$$

where $a(t)$ is the time-dependent ground acceleration. PGA is often expressed as a fraction of the gravitational acceleration g and provides an intuitive link to force demand through $F = ma$ (U.S. Geological Survey, 2019).

PGV is defined as

$$\mathrm{PGV} = \max |v(t)| , \qquad v(t) = \int a(t)\, \mathrm{d}t \tag{2.2}$$

and is often used as a complementary measure when deformation demand is of interest (U.S. Geological Survey, 2019; Wald et al., 1999).

Since structural demand also depends on the frequency content of the motion and the dynamic properties of the structure, response spectra are used to describe period-dependent demand. Spectral acceleration $S_a(T)$ represents the peak acceleration response of an idealised damped single-degree-of-freedom oscillator with natural period T, commonly assuming 5% damping (U.S. Geological Survey, n.d. Ventura, 2007). This concept forms the basis for code-based seismic design, where the demand is typically evaluated at the fundamental period T_1.

In NBC 105:2020, the zone factor Z represents the peak ground acceleration for a given return period and is used, together with the site spectral shape, to define the elastic design spectrum. In this thesis, these parameters are relevant as part of the seismic context and for the interpretation of the code-based load levels introduced in Section 2.3.

Figure 2.4: Author-generated schematic map, adapted from Oxfam (Oxfam, 2015), showing the approximate locations of the 25 April 2015 Gorkha earthquake (M_w 7.8) and the 12 May 2015 aftershock (M_w 7.3).

2.1.5 Seismicity in Nepal

The measures introduced above describe how earthquakes are characterized. The following section outlines why these measures are important in practice by briefly describing the seismic context of Nepal.

Nepal is located in one of the most seismically active regions in the world due to the ongoing collision between the Indian and Eurasian tectonic plates, as seen in Figure 2.2, (Rastogi, 2024). The Indian plate moves northwards at approximately 4-5 cm per year, which leads to significant accumulation of tectonic stresses along the Himalayan arc. When these stresses are released, large earthquakes can occur with severe consequences (Shrestha, 2012b).

One of the most important recent events was the Gorkha earthquake of 25 April 2015 (M_w 7.8), with an epicentre located approximately 77 km northwest of Kathmandu (see Figure 2.4). It was followed by a major aftershock of M_w 7.3 on 12 May (Rastogi, 2024). The earthquake caused extensive destruction, with around 9,000 fatalities, more than 20,000 injured, and approximately 800,000 houses destroyed or damaged. Several UNESCO World Heritage sites were also severely affected. The economic losses were estimated at around 10 billion USD, corresponding to roughly half of Nepal's annual GDP at the time (Rastogi, 2024).

Nepal has continued to experience substantial seismic activity after 2015. During 2022 and 2023, several earthquakes with magnitudes between M_w 5.1 and M_w 6.6 caused both casualties and material damage. According to the National Earthquake Monitoring and Research Centre (NEMRC), Nepal has recorded 1,237 earthquakes of magnitude 4.0 or higher since 1994 (Paudel, 2025). Seismic activity in Nepal is therefore continuous and not limited to a few isolated major events.

As a result, large parts of Nepal are classified as high-seismic-hazard zones according to the Nepal National Building Code (NBC 105:2020). Buildings must therefore be able to resist substantial lateral loads. This makes material choice, masonry detailing, and structural configuration especially important, particularly in rural areas where masonry construction remains common.

Together, these conditions show that Nepal is exposed to a high and persistent seismic hazard. They also underline the importance of understanding how different masonry systems respond to earthquake loading, and why construction details can strongly influence structural safety in practice.

2.2 Buildings in Seismic Regions

Given Nepal's seismicity described above, the following section summarises key building-level concepts that govern seismic performance.

2.2.1 Design considerations for buildings in seismic areas

During seismic loading, structures commonly develop cracking and inelastic deformations. Seismic performance can therefore not be described solely by maximum strength, but must also account for the post-damage response: whether degradation is stable or abrupt, and how much deformation can be sustained before collapse or unacceptable loss of function. Accordingly, ductility and energy dissipation capacity are commonly used to characterise deformation and damage development under earthquake actions (Armouti, 2015).

Ductility

Ductility refers to a structure's ability to sustain load beyond the elastic range by developing inelastic deformations without an immediate and significant loss of load-carrying capacity (NBC 105:2020). Under seismic actions, this means that the structure can accommodate deformation demands without brittle, uncontrolled failure, which distinguishes ductile behaviour from brittle behaviour (Armouti, 2015). In seismic design provisions in Nepal, ductility is treated as a key requirement to satisfy fundamental safety objectives, particularly life safety and collapse prevention (NBC 105:2020).

Energy dissipation

Energy dissipation capacity describes the ability of a structural system to reduce earthquake input energy through irreversible mechanisms such as cracking, frictional sliding and inelastic deformations (Armouti, 2015). The portion of the input energy that is not dissipated is temporarily stored as elastic energy, which can contribute to continued vibrations and increased response demands. In practice, energy dissipation is

closely linked to the stability of the post-elastic response: systems with stable inelastic deformation typically show a gradual degradation of stiffness and strength, whereas brittle mechanisms may lead to rapid loss of capacity once a critical damage mode is activated (Armouti, 2015).

A related concept is toughness, which describes a material's ability to absorb energy before failure. Toughness can be expressed as the energy absorbed during loading, corresponding to the area under the load–deformation or stress–strain curve (Mehta and Monteiro, 2014). In structural analysis, this concept can also be applied to force-displacement curves obtained from numerical simulations or experiments. The area under such curves represents the work performed on the structure and can therefore be used as an indicator of the structural energy absorption capacity. This parameter reflects both the load-carrying capacity and the deformation capacity of the system and can be useful when comparing different materials or structural configurations.

2.2.2 General seismic design requirements

Satisfactory seismic performance requires that earthquake-induced inertial forces can be transferred through a continuous and robust load path, while avoiding configurations that promote unstable global response (e.g. torsion) (NBC 105:2020; Tomaževič, 1999). In masonry buildings, floors and roofs are critical because they act as diaphragms that distribute horizontal actions to the vertical resisting walls and enable so-called box action. Insufficient wall-diaphragm connection is a frequent cause of separation cracks at wall junctions (see Figure 2.9) and can trigger local out-of-plane collapses even when in-plane wall capacity is not exhausted (NBC 105:2020; Tomaževič, 1999).

In addition to load path integrity, plan and elevation regularity strongly influence seismic response. Simple and approximately symmetric layouts, as illustrated in Figure 2.5, reduce torsional amplification and uneven demand among walls (NBC 105:2020; Tomaževič, 1999). Practical recommendations include limiting eccentricity between centre of mass, CG, and centre of stiffness, CR, to reduce torsional effects and avoid concentration of drift in a subset of walls (Mellegård and Steinert, 2016; Shrestha, 2012a).

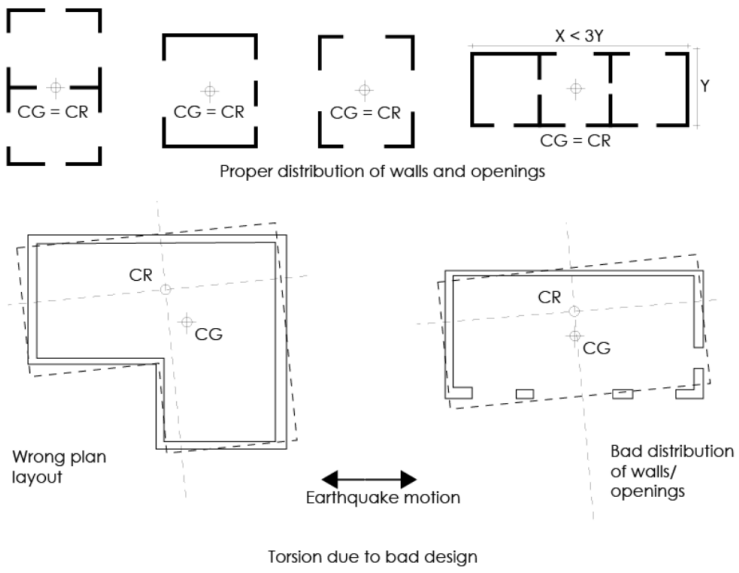

Figure 2.5: Illustration of torsional response due to irregular wall distribution. Adopted from Thudén and Toivonen (2018), based on Maïni (2005).

2.3 NBC 105:2020 Seismic Analysis Methods

NBC 105:2020 specifies requirements for seismic analysis and design of building structures to be constructed in Nepal. The code is applicable to buildings designed with reinforced concrete, structural steel, steel-concrete composite construction, timber, and masonry. Minimum design earthquake loads for buildings, structures, or parts of structures shall be determined in accordance with NBC 105:2020.

NBC 105:2020 states that the seismic analysis for design earthquake loads shall be carried out using at least one of the following methods:

- Equivalent Static Method (ESM)
- Linear dynamic methods: Modal Response Spectrum Method or Elastic Time History Analysis
- Nonlinear methods: Nonlinear Static Analysis (pushover) or Nonlinear Time History Analysis

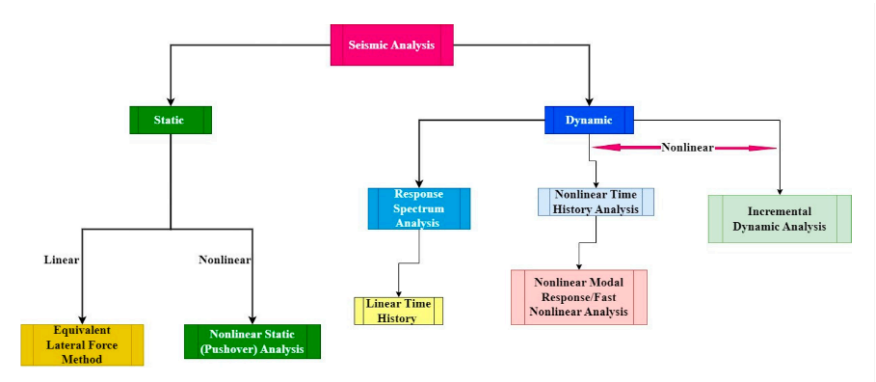

Figure 2.6: Overview of common seismic analysis methods, including static and dynamic approaches and the position of pushover analysis among nonlinear structural assessment techniques (Kuria and Kegyes-Brassai, 2023).

According to NBC 105:2020, the Equivalent Static Method can be used to determine the design values of the serviceability limit state (SLS) irrespective of the configuration and properties of the building. For the ultimate limit state (ULS), the use of ESM is restricted by criteria related to building height, fundamental period and structural irregularity (NBC 105:2020).

The Modal Response Spectrum Method is a linear dynamic method that can be used for all types of structures, including cases where ESM is not applicable (NBC 105:2020). Elastic time history analysis is also a linear dynamic method and may be used to verify that selected response parameters remain within the acceptance limits assumed in design (NBC 105:2020).

Nonlinear static (pushover) and nonlinear dynamic analyses are, according to NBC 105:2020, primarily intended for performance evaluation of existing or retrofitted structures. These methods are used to verify the structural response against the seismic demand established using linear analysis methods such as ESM or the Modal Response Spectrum Method (NBC 105:2020).

2.4 Masonry in seismic regions

Having established the seismic demand and the general principles of earthquake-resistant design, the discussion is here narrowed to masonry. The following section outlines load transfer in masonry walls and the governing failure mechanisms under seismic actions, which are used as a reference for the wall-level analyses later in the thesis.

2.4.1 Load paths in masonry structures

Masonry buildings can often be idealised as shear-wall systems, where lateral actions are resisted by load-bearing walls in two orthogonal directions through a combination of in-plane shear and flexural actions (Tomaževič, 1999). Openings create discontinuities

that modify load paths and stress distributions and therefore influence where damage initiates and how it propagates.

For analysis and interpretation, walls are commonly subdivided into piers and spandrels (see Figure 2.7), since these components may develop different mechanisms and interact through force redistribution during lateral loading (Bothara and Brzev, 2011; Tomaževič, 1999). Damage often initiates locally in piers (see Figure 2.8) and may govern the global in-plane response of the wall, while spandrels influence coupling and the redistribution of forces among piers.

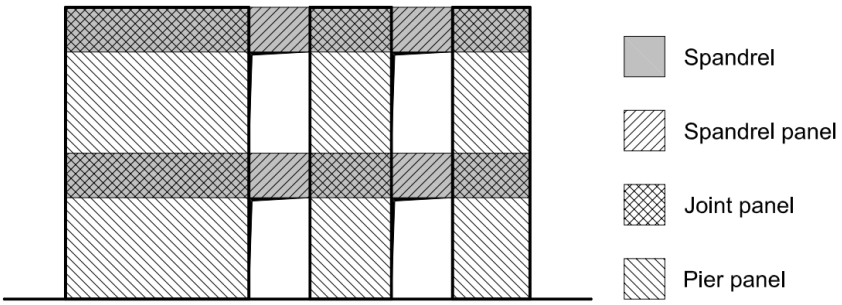

Figure 2.7: Common subdivision of masonry walls into piers and spandrels for structural interpretation, based on Parisi and Augenti (2014).

Failures in masonry can be categorised as local or global (Celano et al., 2021). Local failures dominate within a limited region (e.g. a single pier or around an opening), whereas global failures involve overall loss of capacity or stability of the wall or structure. The distinction is important because local mechanisms may precipitate disproportionate global collapse if load paths are not redundant or if box action is insufficient.

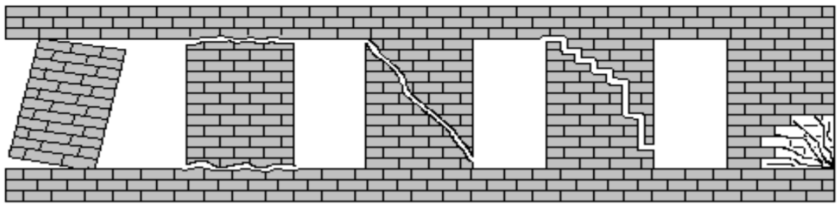

Figure 2.8: Example of pier-dominated damage in masonry (Augenti and Parisi, 2006).

2.4.2 Failure modes

Failure modes in masonry subjected to seismic loading are often governed by a distinct failure mechanism (Bothara and Brzev, 2011; Tomaževič, 1999). Which mechanism develops depends primarily on the wall geometry and on how the wall is connected to the rest of the building, i.e. the available restraint and the level of out-of-plane support. Whether the masonry is unreinforced (URM) or reinforced (RM) also influences the response, where URM generally exhibits more brittle behaviour and a lower deformation capacity.

Masonry failure is commonly classified into in-plane failure (within the wall plane) and out-of-plane failure (perpendicular to the wall plane) (See Figure 2.9). The following sections describe these mechanisms in more detail and conclude with a summary of the key parameters governing the expected failure mode.

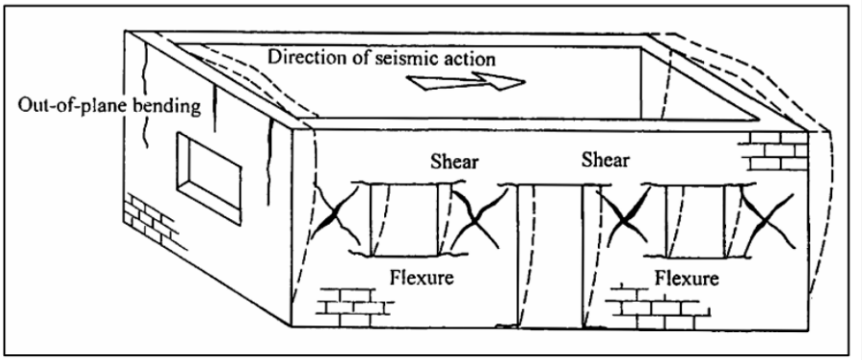

Figure 2.9: Typical failure modes in masonry subjected to seismic actions (Tomaževič, 1999).

In-plane failure

In-plane failure occurs when the wall is subjected to lateral loading within its plane. Common failure mechanisms include diagonal shear failure, sliding shear failure, and flexural (rocking) failure (Tomaževič, 1999).

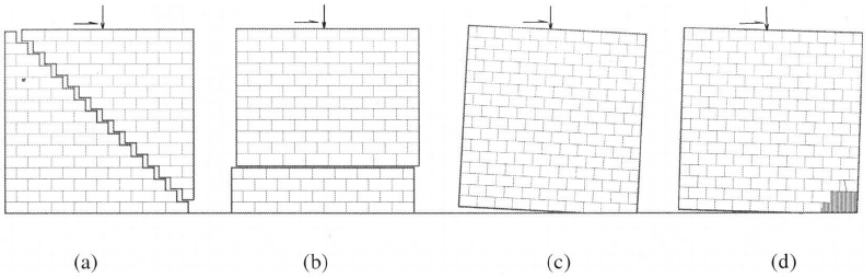

Figure 2.10: In-plane failure modes of masonry: (a) diagonal shear, (b) sliding shear, (c) rocking, (d) rocking with toe crushing. Reproduced from ElGawady et al. (2007).

Diagonal shear failure is characterised by a diagonal crack pattern in the wall (See Figure 2.10(a)). Cracks often initiate near corners, around openings, or in the central region, depending on the wall geometry, boundary conditions and stress distribution (Tomaževič, 1999).

The mechanism develops when tensile stresses exceed the tensile capacity of the masonry. These tensile stresses arise from the combined action of shear and compression (Tomaževič, 1999). The level of vertical load (precompression) affects how the cracking develops. Higher precompression increases the normal stress across bed joints, which tends to restrict joint slip and concentrate the response into a clearer diagonal cracking pattern. The crack may propagate through mortar joints, through the units,

or as a mixed path, depending on the relative properties of units, joints and interfaces (Tomaževič, 1999).

Diagonal shear failure is typically brittle and may lead to rapid loss of lateral capacity, which makes it important to identify in URM (Tomaževič, 1999).

Sliding shear failure occurs when in-plane shear demand exceeds the shear resistance of bed joints, causing relative sliding between units, often along one or multiple horizontal joints (See Figure 2.10(b)). Sliding is more common at low precompression since reduced normal force lowers frictional resistance. Compared to diagonal shear, sliding can be more deformation-driven and may dissipate energy through controlled frictional slip before complete loss of capacity (Tomaževič, 1999).

In rocking (flexural) failure, the in-plane response is governed by wall rotation and joint opening, i.e. a flexural mechanism rather than a shear-controlled one (See Figure 2.10(c)). This response is most common for slender walls and at low levels of precompression, and it may occur with or without local toe crushing (Celano et al., 2021; Tomaževič, 1999). As the wall rotates about a lower edge, joints open on the tension side while compressive stresses concentrate at the compression toe, which can lead to local crushing (See Figure 2.10(d)). Compared with brittle shear failures, rocking can accommodate larger lateral displacements provided that overall stability is maintained; however, repeated opening and closing under cyclic loading contributes to stiffness degradation and influences energy dissipation (Celano et al., 2021).

Out-of-plane failure

Out-of-plane failure refers to response and potential collapse when seismic loading is applied perpendicular to the wall plane, causing bending about the weak axis. In URM, this behaviour is often critical because of the low tensile capacity, meaning that cracking and loss of stability can occur quickly if adequate lateral support is not provided (Bothara and Brzev, 2011; Tomaževič, 1999). The out-of-plane behaviour is strongly governed by the available supports and anchorage. Depending on the structural layout, a wall may span vertically between floor/roof diaphragms or horizontally between transverse walls, and the boundary conditions and connection detailing therefore become decisive for both strength and stability (Bothara and Brzev, 2011).

Several out-of-plane failure mechanisms may develop depending on how the wall is supported and anchored. One of the most severe is overturning (toppling), where a wall segment loses stability and rotates out of plane, typically about its base or along a weak anchorage line. The risk increases for slender walls and when lateral restraint is insufficient. Good box action and robust wall-diaphragm connections are therefore important to provide lateral support and maintain a continuous load path for horizontal seismic actions (Bothara and Brzev, 2011; Tomaževič, 1999).

2.4.3 Reinforced masonry

Reinforcement in masonry (RM) is primarily used to reduce the risk of brittle earthquake-induced failures and to improve post-cracking integrity. By enabling tensile force transfer and maintaining continuity after cracking, reinforcement can shift the response from sudden, mechanism-dominated failures typical of URM towards more stable and ductile behaviour with improved deformation capacity (Armouti, 2015; Tomaževič, 1999).

In Nepalese practice, seismic strengthening of masonry is commonly achieved through horizontal seismic bands (ring beams) and vertical bars at corners, junctions and around openings. Prescriptive detailing guidance for such measures is provided in NBC 202 and NBC 203 (NBC 202:2015; NBC 203:2015). These measures enhance continuity, improve box action, and reduce the risk of local out-of-plane collapses by tying walls and diaphragms together and by strengthening critical discontinuities.

In seismic regions, building codes therefore emphasise constructive measures that enhance continuity and reduce the risk of local collapses. NBC 105 highlights strengthening requirements for masonry, including reinforcement and reinforced concrete bands (RCC bands), particularly for important structures and in higher seismic hazard zones (NBC 105:2020).

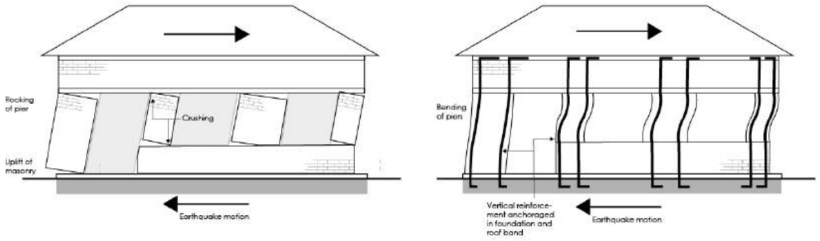

Figure 2.11: Pier response with and without reinforcement (schematic/illustrative) adopted from Thudén and Toivonen (2018), based on Murty (2002).

Horizontal reinforcement

Horizontal reinforcement (RCC bands) is commonly placed at selected levels (plinth, floor levels, above openings/lintel level, under openings and roof level). Bands act as continuous elements that tie walls together, improve box action, and reduce separation cracks and out-of-plane instability by strengthening wall-diaphragm interaction (Bothara and Brzev, 2011).

Vertical reinforcement

Vertical reinforcement is typically placed in corners, intersections in walls and around openings (NBC 105:2020). Since openings divide walls into piers and spandrels, local pier mechanisms often govern the URM response and may fail due to rocking or brittle shear. Vertical reinforcement anchored into the foundation and tied to horizontal

bands stabilises these regions, reduces sliding and local crushing, and promotes a more favourable post-elastic response by maintaining integrity after cracking (NBC 105:2020; Tomaževič, 1999).

2.4.4 Factors governing failure mechanisms

The in-plane response of URM under seismic loading has been investigated extensively through laboratory testing and complementary analytical studies (Celano et al., 2021). Across this literature, four parameters repeatedly govern the response: wall geometry (especially slenderness), boundary conditions (degree of rotational restraint and lateral support), the level of vertical load (precompression) and openings (Tomaževič, 1999). These parameters influence not only which failure mechanism develops, but also the lateral strength (peak base shear), stiffness degradation, and drift capacity prior to significant strength loss (Magenes and Calvi, 1997; Petry and Beyer, 2014).

Geometry (slenderness)

Wall slenderness (H/L) affects the balance between shear demand and flexural demand and therefore governs both failure mode and capacity. Squat walls (low H/L) are more likely to develop shear-dominated responses and can reach relatively higher peak base shear, but they often exhibit a more abrupt post-peak strength drop once a dominant diagonal crack localises (Abrams and Shah, 1992; Magenes and Calvi, 1997). Slender walls (high H/L), in contrast, tend to be flexure-dominated (rocking/toe crushing) and typically reach lower peak base shear, while sustaining larger drift before severe strength loss (Abrams and Shah, 1992; Magenes and Calvi, 1997). Increasing slenderness typically reduces peak base shear. At the same time, the wall can often sustain larger drift before major strength loss (Magenes and Calvi, 1997).

Boundary conditions

Boundary conditions control the moment profile and shear distribution along the wall height and therefore affect where cracking initiates, how damage spreads, and how quickly stiffness and strength degrade. This is primarily a capacity issue rather than only a change in the observed failure mechanism. Changes in rotational restraint and coupling can significantly affect peak strength, stiffness degradation, and drift capacity at common limit states. For example, cyclic tests with systematically varied restraint show that increased restraint (shorter effective shear span and/or higher imposed end moments) tends to reduce drift capacity and can shift the wall towards more brittle behaviour even when geometry and materials are unchanged (Petry and Beyer, 2014).

Vertical load (precompression)

Precompression increases the normal force across bed joints and therefore the available frictional resistance, which typically increases initial stiffness and peak shear resistance up to practical limits. At the same time, higher axial stress can reduce deformation capacity because damage localises earlier (e.g. faster diagonal crack development and earlier crushing), leading to lower drift capacity at a given strength-drop criterion (Abrams and Shah, 1992; Petry and Beyer, 2014). Cyclic wall test programmes that vary vertical compressive stress show that axial load level can change both lateral strength and drift capacity, and may alter the governing failure mode from sliding at low precompression to diagonal cracking/crushing mechanisms at higher precompression (Abrams and Shah, 1992; Tomaževič, 1999).

Openings

Openings modify the stress field by introducing local stress concentrations; cracking therefore often initiates at opening corners, and both the crack pattern and the global capacity become sensitive to opening geometry. In general, increasing opening size reduces stiffness and peak base shear and may also reduce drift capacity due to earlier localisation around the opening (Liu and Crewe, 2020). Beyond size, opening position is critical: parametric studies show that openings located unfavourably relative to the compression diagonal can cause a disproportionate reduction in both strength and displacement capacity compared to openings with the same area placed elsewhere (Liu and Crewe, 2020). Experimental and numerical comparisons of walls with and without openings likewise show reductions in lateral strength and clear changes in damage progression when openings are present (Doran et al., 2023).

In this study, geometry and support conditions are varied to quantify their influence on failure mode and capacity. The vertical load is kept as constant as practical to limit the parameter space and enable clear comparisons between cases.

2.5 Materials

This thesis compares traditional fired clay brick masonry with interlocking compressed stabilised earth block (CSEB) masonry with and without vertical reinforcement. The purpose of this chapter is to (i) summarise the construction context and material characteristics relevant for Nepal, and (ii) provide the background for the representative material parameters and modelling assumptions adopted in the numerical analyses.

2.5.1 Fired bricks

Burnt clay bricks are one of the most dominant construction materials in Nepal and have been used for several centuries (Mukai et al., 2022; Thapaliya et al., 2024). The characteristic red brick façades shape much of Nepalese architecture and appear in

everything from historic temples to schools and residential buildings. Approximately 80% of the country's buildings are estimated to be constructed using some form of stone or brick masonry, often without formal engineering supervision (National Statistics Office, 2024).

The central role of bricks in Nepal's building culture is largely explained by local availability and an established production infrastructure. Suitable clay resources are widely available, particularly in the Kathmandu Valley and the Terai region (Thapaliya et al., 2024). The manufacturing process, which mainly requires clay, fuel, and labour, is relatively simple and cost-effective. Nepal has more than 1500 active brick kilns and an annual production on the order of billions of bricks (Eil et al., 2020). The brick sector is also a major employer, with several hundred thousand seasonal workers engaged in brick production (International Labour Organization, 2020).

From a structural point of view, fired brick units commonly exhibit relatively high compressive strength compared to many locally available alternatives. However, the overall masonry system remains brittle in tension and shear, and seismic performance is often governed by mortar quality, joint integrity and unit-mortar interface behaviour rather than unit compressive strength alone (Bothara and Brzev, 2011; Mishra et al., 2019; Tomaževič, 1999). This is particularly relevant for numerical modelling, where representative parameters must reflect the masonry assemblage and not only the units.

In addition to structural considerations, brick production in Nepal is associated with substantial environmental impacts. Annual emissions have been estimated at approximately 1.2 million tonnes of CO_2-equivalents (United Nations Development Programme (UNDP), 2024). Brick kilns also emit particulate matter (including black carbon) as well as sulphur dioxide and nitrogen oxides, which deteriorate air quality, particularly in regions with high kiln density such as the Kathmandu Valley (Eil et al., 2020; United Nations Development Programme (UNDP), 2024). Further reported impacts include degraded soil quality and evidence of heavy metal accumulation in agricultural land adjacent to kiln clusters (Koirala et al., 2025). These aspects motivate interest in alternative masonry systems with lower embodied emissions while maintaining or improving structural performance.

Material composition and variability

Fired bricks are manufactured from clay with varying proportions of sand, silt, and mineral constituents. The raw materials are mixed with water, shaped into units, dried, and fired. Variations in clay composition and firing conditions influence porosity and water absorption, and consequently density, compressive strength and stiffness (Subedi, 2020). Since raw materials and production conditions can vary between sites, fired bricks produced in Nepal may exhibit significant variability in mechanical properties (Subedi, 2020). This variability should be considered when selecting representative material parameters for numerical modelling and when interpreting capacity and drift predictions.

Fired brick masonry

Fired clay brick masonry should be treated as a heterogeneous composite system governed by the interaction between brick units, mortar, and unit-mortar interfaces/joints (Lourenço et al., 1995). While brick and mortar are often idealised as homogeneous and isotropic at the material scale, masonry is anisotropic at the assemblage level because the arrangement of bed joints and head joints introduces a directional fabric and preferential planes of weakness (Lourenço et al., 1995).

In Nepalese practice, national guidance typically places joint thickness within 10-20 mm (horizontal and vertical), and a value of about 10 mm is commonly adopted as a representative thickness in description and modelling (NBC 109:1994). Mortar quality and workmanship can vary substantially. For Nepalese historical masonry, component testing has shown that mud mortar can exhibit markedly lower material properties than the bricks, implying that global stiffness and lateral resistance may be governed by joint and interface behaviour (Mishra et al., 2019). In-situ characterisation in the Kathmandu Valley has also reported very low shear strength levels for some historical brick masonry, illustrating how lateral capacity can be controlled early by weak mortar and contact zones (Giri et al., 2024).

Overall, the seismic performance of fired brick masonry in Nepal should therefore be assessed at the masonry level, not solely from the compressive strength of the bricks, with explicit attention to joint thickness, mortar quality, and interface behaviour (Giri et al., 2024; Mishra et al., 2019; NBC 109:1994).

2.5.2 Interlocking compressed stabilised earth blocks

The use of earth as a construction material is long-established in many regions globally (Resilient Structures Private Limited, 2022). Compressed stabilised earth blocks (CSEB) were developed as a modern evolution of traditional earth construction. Although CSEB are similar in function to fired bricks, they differ fundamentally in production: rather than being kiln-fired, they are formed by mechanical compaction and curing (Build Up Nepal (BUN), 2026; Resilient Structures Private Limited, 2022).

Figure 2.12: Interlocking compressed stabilised earth blocks (CSEB) adopted from Build Up Nepal (BUN) (2026).

In Nepal, interlocking CSEB were promoted following the 2015 Gorkha earthquake, driven by the demand for construction methods that are both resource-efficient and potentially more seismically resilient. Build Up Nepal has been a central actor in implementing interlocking CSEB systems in reconstruction and new construction (Build Up Nepal (BUN), n.d.).

Reported advantages of CSEB include reduced embodied emissions and energy use compared to fired clay bricks. Shrestha (2012a) reports substantially lower carbon emissions and energy consumption for CSEB relative to fired bricks, and Fordham (2021) similarly reports large reductions in CO_2 emissions per unit mass of product. Economic and local-capacity benefits are also commonly highlighted, since production and construction can be organised locally with comparatively simple equipment (Build Up Nepal (BUN), 2026; Center for Research & Development (CERAD), 2025; Resilient Structures Private Limited, 2022).

CSEB are manufactured in several configurations. In this study, the blocks correspond to those commonly produced and implemented by Build Up Nepal, featuring an interlocking geometry and being available in full and half-unit formats.

Material composition

Interlocking CSEB are typically produced from soil or stone dust mixed with cement and water (Shrestha, 2012a). A suitable soil composition includes a balance of gravel, sand, silt and clay fractions, while cement content for high-quality blocks is commonly within the range of 5-10% by mass (Shrestha, 2012a). After mixing, the material is compacted using a press and cured (commonly 28 days). Strength development primarily occurs through cement hydration. Consequently, mechanical properties are governed by cement content, moisture during pressing, degree of compaction, and

curing quality (Shrestha, 2012a).

In this study, the analyses adopt the conservative Class A block type with a cement content of 5% in accordance with project requirements.

CSEB masonry

Similar to fired bricks, CSEB are brittle heterogeneous materials with substantially higher compressive strength than tensile strength (Bothara and Brzev, 2011; Shrestha, 2012a). In interlocking systems, shear resistance may be enhanced by mechanical keying between units compared with conventional brick masonry under low to moderate normal stress (Maïni, 2005; Sturm et al., 2014). Load transfer in CSEB masonry occurs through a combination of contact pressure, friction and interlock effects at the interfaces, while grout and/or thin bedding layers may serve as stress-equalising media and improve force transfer where geometric imperfections exist.

When vertical steel reinforcement is introduced into grouted cores, the deformation capacity and residual strength can be improved by providing tensile force transfer and maintaining integrity after cracking, which is particularly relevant under cyclic lateral loading (Bothara and Brzev, 2011; Shrestha, 2012a).

2.5.3 Mortar and grout (role and modelling relevance)

Mortar and grout are included here only to clarify where force transfer and integrity are expected to be governed by joint- and interface behaviour in the two masonry systems. For fired clay brick masonry, mortar joints provide geometric tolerance and bonded shear transfer; therefore, joint properties and workmanship can govern in-plane mechanisms such as sliding along bed joints and diagonal cracking (Lourenço et al., 1995; Tomaževič, 1999). In Nepalese practice, NBC 109 defines the standard brick dimensions for a 10 mm mortar joint, which motivates adopting a representative joint thickness in the description and modelling (NBC 109:1994).

For the interlocking CSEB system, the present study idealises bed-joint behaviour as dry-stacked contact in accordance with project requirements; hence, no tensile bond or cohesive mortar layer is assumed between units, and interface resistance is represented through contact pressure and friction (see Section **??**) (Sturm et al., 2014). Grout is instead treated as a separate cementitious material in the block cavities, primarily relevant for stress equalisation in the cores and, where applicable, for interaction with vertical reinforcement (Shrestha, 2012a).

2.5.4 Reinforcement (Nepalese detailing for modelling)

For load-bearing masonry buildings constructed without full engineering design, Nepal provides prescriptive earthquake-resistant detailing rules through NBC 202 (Guidelines on Load Bearing Masonry) and NBC 203 (Guidelines for Earthquake Resistant Building Construction: Low Strength Masonry) (NBC 202:2015; NBC 203:2015). The

detailing aims to (i) improve box action and load-path continuity through horizontal seismic bands, and (ii) reduce the probability of brittle local failures—particularly out-of-plane collapses—by providing vertical reinforcement at discontinuities such as corners, junctions and opening jambs (NBC 202:2015; NBC 203:2015).

Horizontal bands (ring beams) — prescriptive minimum detailing

NBC 203 specifies reinforced concrete (RC) bands at plinth, sill, lintel (or floor) and roof levels, with minimum reinforcement as summarised below (NBC 203:2015):

- **Plinth band:** thickness 150 mm, 4 bars 12 mm. For hard soil, thickness may be reduced to 75 mm using 2 bars 12 mm.
- **Sill band:** thickness 75 mm, 2 bars 10 mm.
- **Lintel band:** for small openings ($\leq$ 1.0 m) with masonry height above opening $\leq$ 0.9 m, a 75 mm lintel band is sufficient with longitudinal reinforcement placed at the bottom face and a 25 mm cover from the bottom (NBC 203:2015). For openings up to 1.5 m and masonry height above opening up to 1.2 m, a 150 mm lintel band is required.
- **Roof band:** thickness 75 mm, 2 bars 12 mm.
- **Dowel (stitch):** thickness 75 mm, 2 bars 8 mm.

Department of Urban Development and Building Construction (DUDBC) (NBC 203:2015) notes that the specified reinforcement refers to high strength deformed bars (Fe415), while mild steel bars of equivalent area may also be used.

Department of Urban Development and Building Construction (DUDBC) (NBC 202:2015) provides equivalent prescriptive band detailing and additionally states that the concrete for RC bands should be at least grade M20.

Vertical reinforcement — location, spacing and bar sizes

Department of Urban Development and Building Construction (DUDBC) (NBC 203:2015) states that vertical reinforcements shall be located at all corners and junctions of walls, starting from the foundation and continued to the roof band. The same guideline provides typical reinforcement sizes and spacing rules (NBC 203:2015):

- **Bar diameters:** 12 mm or 10 mm (typically using deformed bars).
- **Spacing along wall length:** vertical reinforcement placed at 1.2 - 1.5 m spacing.
- **Around openings:** additional vertical reinforcement within approximately 500 mm of openings.

3 Numerical modelling framework of masonry

This chapter defines the numerical modelling framework used to evaluate the in-plane seismic response of masonry wall panels and interlocking compressed stabilised earth block (CSEB) systems. Although research on numerical modelling of interlocking, dry-stacked CSEB is limited, the main response mechanisms are common to masonry assemblies in general, including stress redistribution, cracking and crushing in compression, and sliding or rocking along discontinuities (Celano et al., 2021; Magenes and Calvi, 1997; Maïni, 2005; Sturm et al., 2014; Tomaževič, 1999). Therefore, established masonry modelling concepts are adopted, with explicit consideration of two defining features of the CSEB system examined in this study: (i) dry-stacked, non-cohesive interfaces and (ii) geometric interlocking (Build Up Nepal (BUN), 2026; Maïni, 2005; Sturm et al., 2014).

The analyses focus on local failure mechanisms in wall panels and piers, rather than the global dynamic response of an entire building. Accordingly, the modelling strategy is formulated to resolve (a) material nonlinearity within masonry units and mortar, and (b) deformation driven by discontinuities through contact at interfaces (Lourenço, 1996; Lourenço et al., 1995). This approach motivates the use of a continuum-based finite element discretisation, coupled with constitutive laws and interface descriptions, as detailed in the following sections (Lourenço, 1996; Lourenço et al., 1995).

3.1 Finite Element Method

The Finite Element Method (FEM) is a numerical method used to solve the partial differential equations that describe physical systems. The method is based on subdividing the studied domain into a number of smaller subdomains, called elements, which are connected at points called nodes. The nodes represent the locations in the model where displacements (and, in some formulations, rotations) can develop, and are therefore central for describing the structural response. Each node is assigned a number of degrees of freedom (DOF), which define the ways in which the node can translate and/or rotate. The number of degrees of freedom is determined both by the chosen element type and by the boundary conditions applied to the analysed structure.

In seismic analysis, a structure can often be idealised into a simplified model that captures the global response using a limited number of degrees of freedom. The purpose of such an idealisation is to reduce model complexity while retaining the deformations and motions that govern the seismic response (Paultre, 2011). Consequently, simplified models are commonly used in which the global lateral displacement constitutes the dominant response quantity (Fajfar, 2000).

In this thesis, FEM is used to resolve localised stress and deformation fields that are needed to capture masonry-specific failure mechanisms. This is consistent with established masonry modelling literature, where the choice of modelling strategy depends on whether the objective is global response or local mechanisms, and where micro-modelling approaches are commonly adopted to study cracking/crushing and interface-driven behaviour (Lourenço, 1996; Lourenço et al., 1995). Accordingly, the nonlinear response in the analyses primarily stems from (i) material nonlinearity within units and mortar/grout and (ii) contact and frictional interaction along discontinuities and interfaces, which are treated explicitly in the adopted modelling framework.

3.2 Numerical modelling strategies for masonry

Masonry exhibits a pronounced heterogeneity and discontinuity due to the presence of units, mortar joints and interfaces. As a consequence, different numerical idealisations are used depending on whether the objective is global capacity or local failure mechanisms. Following Lourenço et al. (1995) and Lourenço (1996), three principal strategies are commonly distinguished: macro-modelling, simplified micro-modelling, and detailed micro-modelling (Figure 3.1).

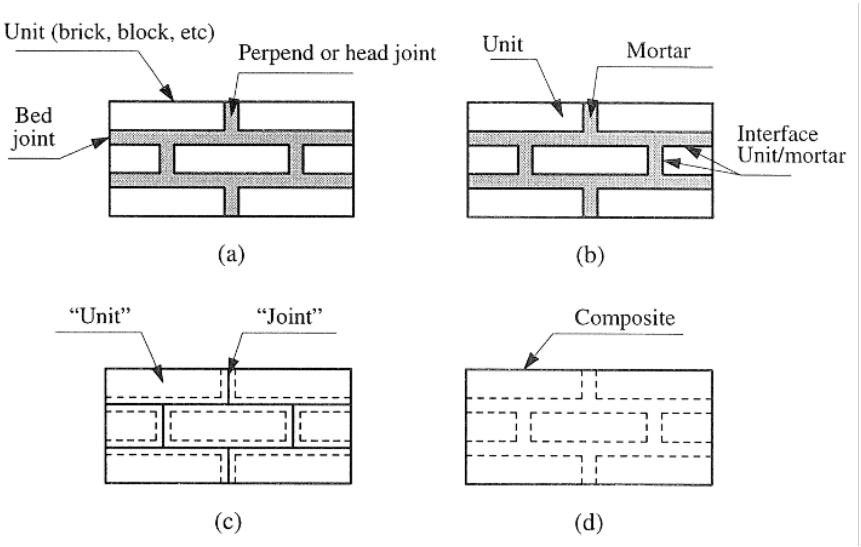

Figure 3.1: Modelling strategies for masonry: (a) masonry sample; (b) detailed micro-modelling; (c) simplified micro-modelling; (d) macro-modelling (Lourenço et al., 1995).

3.2.1 Macro-modelling

In macro-modelling, masonry is represented as an equivalent homogeneous continuum, without explicitly distinguishing units, mortar and interfaces. The approach is computationally efficient and is therefore attractive for large structural models, but it relies on empirical parameter calibration at the masonry assemblage level rather than on constituent-level properties (Lourenço et al., 1995). For the present study, this is a decisive limitation: the investigated systems are governed by discontinuity-driven

mechanisms (joint sliding, rocking and local crushing) and, for interlocking CSEB, by dry-stacked, non-cohesive contact. These mechanisms cannot be represented explicitly in a purely homogenised description and would be embedded indirectly into "effective" parameters, reducing interpretability of the predicted failure modes.

3.2.2 Simplified micro-modelling

In simplified micro-modelling, units are modelled as continuum solids, while the joints are idealised as zero-thickness interfaces that represent the combined behaviour of mortar and the unit-mortar bond (Lourenço et al., 1995). To preserve the overall geometry, the unit dimensions are typically expanded to account for mortar thickness, and cracking/sliding is assumed to localise primarily in the joint interfaces (Lourenço, 1996). This strategy provides an efficient compromise when the response is dominated by joint behaviour and when the joint can be meaningfully represented by an interface law. However, for interlocking dry-stacked CSEB, the physical joint is not a bonded mortar layer but a contact interface with friction and geometric interlock. A simplified interface representation that effectively "replaces" the joint by a cohesive/bonded law risks imposing an artificial initial cohesion or tension transfer that is not present in the system. Therefore, simplified micro-modelling is not adopted as the primary strategy for the interlocking CSEB panels considered herein.

3.2.3 Detailed micro-modelling

In detailed micro-modelling (DMM), units and mortar are modelled explicitly as separate continuum domains, and their interaction is described at the interfaces (Lourenço et al., 1995). This enables constituent-specific material behaviour and discontinuity-driven mechanisms to develop naturally, including cracking in mortar and units, sliding along joints, and mixed failure modes (Lourenço, 1996). The main disadvantage is the substantially increased computational cost and the increased sensitivity to interface modelling choices.

In this work, DMM is adopted to resolve the local mechanisms that are central to the comparison between systems: (i) dry-stacked frictional contact and interlocking action for CSEB, and (ii) mortar-mediated interaction and cracking for fired brick masonry. The consequence of this choice is that the predicted post-peak response may become sensitive to mesh resolution and to the assumed interface parameters; therefore, the study emphasises comparative trends and clearly separates conclusions drawn from peak capacity versus those drawn from post-peak softening response.

3.3 Constitutive material modelling

Within the detailed micro-modelling (DMM) framework adopted in this work, the global panel response is governed by local mechanisms developing within the constituents (units and mortar/grout) and at their interfaces. A constitutive description is therefore required to (i) represent load-carrying capacity in compression, (ii) represent

loss of stiffness/strength due to cracking and crushing, and (iii) interact consistently with interface/contact formulations such that the predicted failure mode remains physically interpretable.

Masonry is characterised by a strong asymmetry between compression and tension, limited tensile capacity, and progressive stiffness degradation as cracking develops. Consequently, analyses intended to study peak capacity and failure mechanisms require nonlinear material behaviour; a purely linear elastic idealisation can only describe the initial stiffness and stress distribution prior to cracking (Lourenço, 2002). In particular, linear elasticity does not introduce a tensile strength limit and cannot represent damage-induced stiffness reduction, which makes it unsuitable for assessing ultimate capacity or mechanism development in masonry (Lourenço, 2002).

In the present study, nonlinear constitutive behaviour is introduced to capture damage progression within the constituents under increasing in-plane loading, including cracking-induced stiffness degradation and compressive crushing at highly stressed regions (e.g. near the toe and around interlocking features). It is emphasised that the post-peak response of softening quasi-brittle materials is generally sensitive to discretisation and softening regularisation; therefore, the numerical results are interpreted with a clear distinction between (a) peak strength and governing failure mode, and (b) detailed post-peak softening characteristics. The specific nonlinear constitutive model adopted herein is the Concrete Damaged Plasticity (CDP) model, introduced in the next section.

3.3.1 Concrete Damage Plasticity (CDP)

To represent nonlinear behaviour of quasi-brittle materials in the detailed micro-modelling (DMM) framework, a continuum damage-plasticity model (CDP) was adopted. The Concrete Damaged Plasticity (CDP) model was originally developed by Lubliner et al. (1989) and later extended by Lee and Fenves (1998). The model combines (i) isotropic plasticity in tension and compression with (ii) an isotropic elastic damage formulation to describe nonlinear concrete behavior. The model considers stiffness degradation due to plastic deformation in tension and compression, as well as stiffness recovery under cyclic loading. The model is also based on the assumption that damage is equal in all directions, which makes it applicable under arbitrary loading conditions, including cyclic loading (Xiao et al., 2017). Although the CDP model was originally developed for concrete, it is also used to model the tensile and compressive response of brittle materials such as masonry (Doran et al., 2023). In this study, the CDP model is used to capture tensile cracking and compressive crushing in the quasi-brittle materials including CSEB, mortar/grout, and fired clay brick.

In ABAQUS, described in Chapter 3.5, the material input for the CDP model is defined through two main components: concrete plasticity parameters and concrete damage parameters. These are presented in the following sections.

Concrete plasticity parameters

In ABAQUS, the CDP model requires the definition of five plasticity parameters: the dilation angle (ψ), the eccentricity (ϵ), the ratio (σ_{b0}/σ_{c0}), the parameter (K_c), and a viscosity parameter (μ). These parameters define (i) the shape and development of the yield surface and (ii) the plastic flow potential, which together govern the pressure-dependent inelastic response of the material (SIMULIA, 2024d).

Yield surface The CDP yield function, proposed by Lee and Fenves (1998), is expressed as:

$$F = \frac{1}{1-\alpha}\left(q - 3\alpha\rho + \beta(\varepsilon^{pl})\sigma_{\max} - \gamma(-\sigma_{\max})\right) - \sigma_c(\varepsilon_c^{pl}) = 0 \tag{3.1}$$

where ρ is the hydrostatic pressure stress, q is the von Mises equivalent effective stress, and $\sigma_{\max}$ is the maximum principal effective stress. The formulation includes both normal stress and shear stress components, meaning that yielding and failure are governed by the combined effect of normal and shear stresses. The term "shape of the yield surface" refers to the geometry of this failure boundary in stress space, while "development of the yield surface" describes how the boundary changes as plastic deformation develops through hardening and/or softening. The dimensionless parameters α, β, and γ control the yield surface. They are defined as:

$$\alpha = \frac{(\sigma_{b0}/\sigma_{c0}) - 1}{2\,(\sigma_{b0}/\sigma_{c0}) - 1}, \qquad 0 \leq \alpha \leq 0.5 \tag{3.2}$$

$$\beta = \frac{\sigma_c(\varepsilon_c^{pl})}{\sigma_t(\varepsilon_t^{pl})}(1-\alpha) - (1+\alpha) \tag{3.3}$$

$$\gamma = \frac{3(1-K_c)}{2K_c - 1} \tag{3.4}$$

The ratio σ_{b0}/σ_{c0} is the ratio between the initial biaxial compressive yield stress and the initial uniaxial compressive yield stress. The parameter K_c controls the shape of the yield surface, and it's values is between 0.5 and 1. When $K_c = 1$, the yield surface becomes circular, corresponding to the classical Drucker-Prager criterion. Lower values for K_c are commonly used to better represent quasi-brittle materials. The influence of K_c on the yield surface is illustrated in Figure 3.2

Plastic flow potential In CDP, plastic deformation follows a non-associated flow rule. This means that the plastic flow develops along the normal to the plastic potential surface and not along the normal to the yield surface. In ABAQUS, the flow potential is defined using a hyperbolic Drucker-Prager function as:

$$G = \sqrt{(\epsilon\sigma_{t0}\tan(\psi))^2 + q^2} - p \cdot \tan(\psi), \tag{3.5}$$

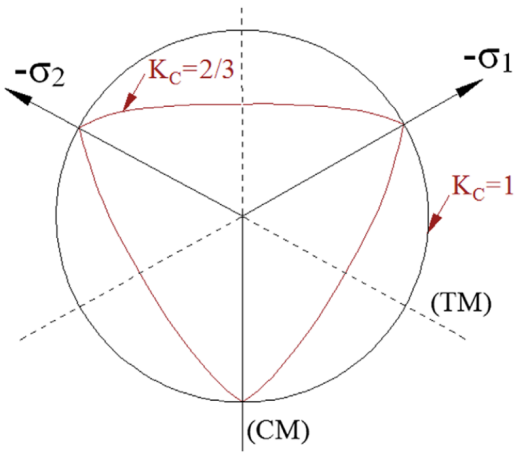

Figure 3.2: Drucker-Prager yield criteria in the deviatoric plane for different K_c (Bui et al., 2020).

where σ_{t0} is the tensile strength, p is the effective pressure stress, ψ is the dilation angle, and ϵ is the eccentricity parameter (SIMULIA, 2024d). The hyperbolic shape of the Drucker-Prager flow potential in the p-q plane, including the definition of the dilation angle, ψ, and the eccentricity, ϵ, is illustrated in Figure 3.3. The dilation angle ψ controls the volumetric expansion (dilatancy) during plastic shear; larger values lead to greater volumetric plastic strain. The influence of the dilation angle on deformation and separation between units is illustrated in Figure 3.4. The eccentricity ϵ controls the shape of the hyperbolic function and determines how quickly the flow potential approaches its asymptote in the p-q plane .

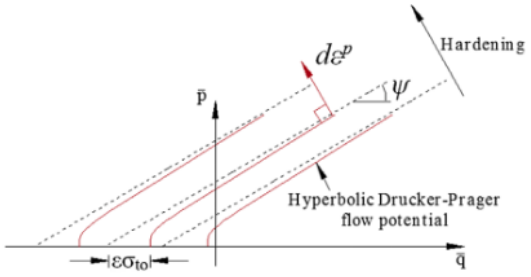

Figure 3.3: Drucker-Prager flow potential in the p-q plane (Bui et al., 2020).

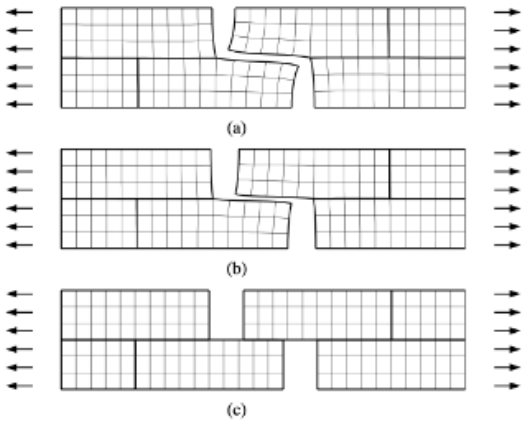

Figure 3.4: Influence of dilatancy angle ψ in tension. Deformed mesh at ultimate stage: (a) $\tan\psi = 0.75$; (b) $\tan\psi = 0.2$; (c) $\tan\psi = 0$ (Lourenço, 1996).

Viscosity parameter When material strength and stiffness decrease in the softening regime, numerical convergence problems may occur. To improve numerical stability, the CDP model in ABAQUS includes a viscosity parameter μ, which allows the

stress state to temporarily exceed the yield surface through viscoplastic regularisation (Doran et al., 2023).

Concrete damage parametrar

In addition to the plasticity parameters, the CDP model requires the definition of concrete damage parameters in ABAQUS. The input consists of the stress-strain relationships σ_t-ε_t^{ck} in tension and σ_c-ε_c^{in} in compression, together with the corresponding damage variables d_t and d_c. The damage variables are defined over the same strain intervals as the respective tensile and compressive behaviour. They describe the progressive degradation of the material response due to cracking in tension and crushing in compression.

For both tension and compression, the inelastic strain, ε^{in}, and the cracking strain, ε^{ck}, is calculated as the difference between the total strain, ε, and the elastic strain, ε_0^{el}, of the undamaged material (Wang et al., 2023), see Equation 3.6.

$$\varepsilon^{(in/ck)} = \varepsilon - \varepsilon_0^{el} \tag{3.6}$$

where the elastic strain is given as:

$$\varepsilon_0^{el} = \frac{\sigma}{E_0}, \tag{3.7}$$

where σ is the current stress and E_0 is the young's modulus of the undamaged material. The inelastic strain is then converted into plastic strain, ε^{pl}, according to:

$$\varepsilon^{pl} = \varepsilon^{(in/ck)} - \frac{d}{1-d}\frac{\sigma}{E_0} \tag{3.8}$$

where the damage variables d_t and d_c are defined as functions of cracking strain and inelastic strain, respectively. The decomposition of total strain into elastic, inelastic (or cracking), and plastic components, as well as the degradation of stiffness through the damage variable d, is illustrated in Figure 3.5 for compression and in Figure 3.6 for tension.

The damage parameter varies between 0 to 1, where $d = 0$ represents undamaged material and $d = 1$ represents complete loss of stiffness, see Figure 3.7. The damage variables can be determined from experimental or analytical relationships as:

$$d = 1 - \frac{E}{E_0} \tag{3.9}$$

where E is the degraded elastic modulus obtained from unloading-reloading tests. When such data are not available, the damage variable may alternatively be approximated as:

$$d = 1 - \frac{\sigma}{\sigma_u} \tag{3.10}$$

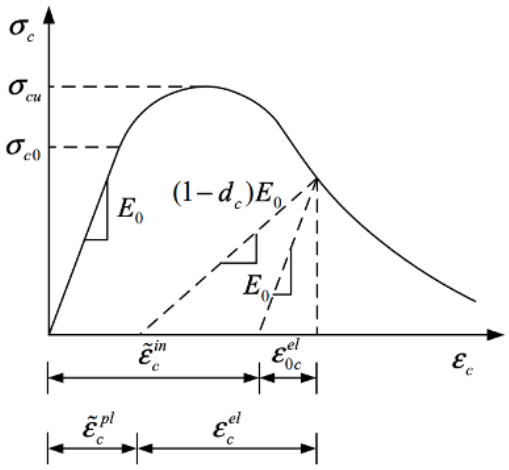

Figure 3.5: Uniaxial compressive stress-strain curve (Wang et al., 2023).

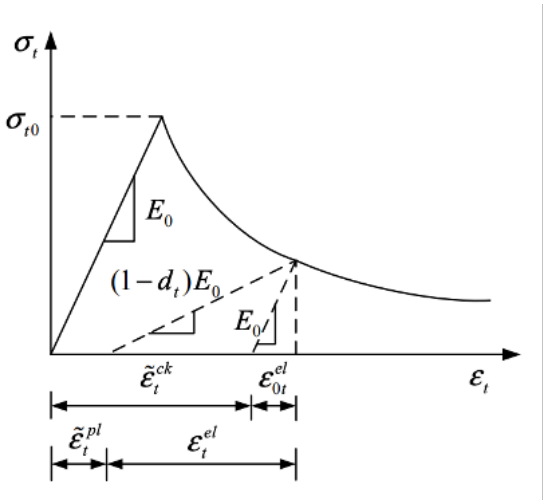

Figure 3.6: Uniaxial tensile stress-strain curve (Wang et al., 2023).

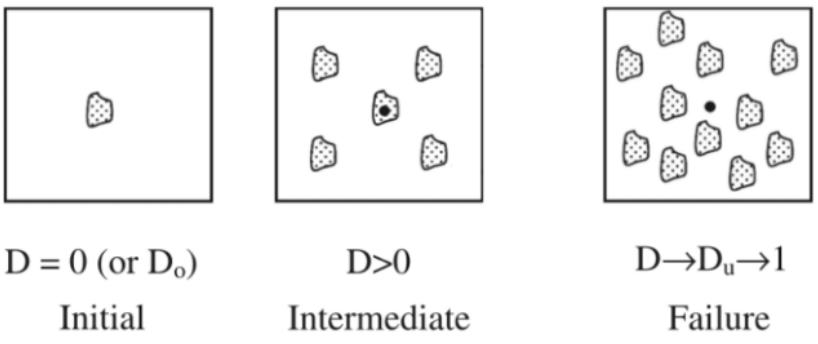

Figure 3.7: Schematic illustration of damage evolution in the material, from the initial state to intermediate damage and final failure, adapted from Akhaveissy and Milani (2012).

3.3.2 Steel reinforcement model in ABAQUS

In ABAQUS, steel reinforcement can be modelled using an elastic-plastic material law combined with ductile damage initiation and evolution. This makes it possible to capture yielding, strain hardening, softening, and fracture of the reinforcement. The elastic response is defined by Young's modulus E and Poisson's ratio ν.

Plasticity is defined by a stress-plastic strain relation. ABAQUS uses plastic strain as the inelastic part of the total strain. It is obtained by subtracting the elastic strain from the total strain, i.e.

$$\varepsilon_{pl} = \varepsilon_{tot} - \sigma/E, \tag{3.11}$$

where ε_{tot} is the total strain, σ is the current stress, and E is Young's modulus (SIMULIA, 2024b). The plastic input is therefore given as stress versus ε_{pl}.

To allow fracture, ductile damage initiation can be used. In ABAQUS, the ductile damage criterion requires the fracture (damage initiation) plastic strain ε_D^{pl}, the stress triaxiality η, and the plastic strain rate $\dot{\varepsilon}^{pl}$ (SIMULIA, 2024c). Stress triaxiality is defined as

$$\eta = \sigma_m/\sigma_{eq}, \tag{3.12}$$

where σ_m is the mean stress and σ_{eq} is the von Mises equivalent stress (SIMULIA, 2024c).

After damage initiation, damage evolution can be defined. A displacement-based formulation relates the equivalent plastic displacement to the equivalent plastic strain as

$$\bar{u}^{pl} = L_c\, \bar{\varepsilon}^{pl}, \tag{3.13}$$

where L_c is the characteristic mesh element length and $\bar{\varepsilon}^{pl}$ is the equivalent plastic strain(figuuur) (SIMULIA, 2024a). The equivalent plastic strain capacity after damage initiation is computed as

$$\bar{\varepsilon}_{pl} = \bar{\varepsilon}_f^{pl} - \bar{\varepsilon}_D^{pl}, \tag{3.14}$$

where $\bar{\varepsilon}_D^{pl}$ is the plastic strain at damage initiation and $\bar{\varepsilon}_f^{pl}$ is the ultimate plastic strain at failure. Complete failure occurs when $\bar{u}^{pl}$ reaches the specified value $\bar{u}_f^{pl}$ (SIMULIA, 2024a).

3.3.3 Contact modelling in masonry

Within the detailed micro-modelling (DMM) strategy, interfaces govern key deformation and failure mechanisms in masonry through (i) unilateral normal contact (opening/closing) and (ii) tangential slip under shear. A realistic model must therefore allow separation in the normal direction and sliding in the tangential direction, since joint opening and sliding are frequently observed as dominant mechanisms in masonry (Lourenço, 1996; Lourenço et al., 1995).

Interface behaviour is commonly decomposed into normal and tangential components (Lourenço, 2002): in the normal direction, load transfer is compression-only (no tensile resistance) to permit opening; in the tangential direction, shear resistance is governed by friction and, where relevant, an initial cohesion/bond contribution.

In the present work, cohesive/bonded interface behaviour is *not* included in the baseline models. This is a deliberate choice driven by lack of reliable interface parameters (tensile/shear strengths and fracture energies) for the specific brick-mortar system considered. Accordingly, all interfaces are idealised as frictional contact, which corresponds to modelling the joints primarily in a post-debonded state. This choice is conservative with respect to initial stiffness and peak strength when intact bond would otherwise contribute to load transfer; the implication is that predicted capacity may be underestimated and that early joint separation/slip may be promoted. However, the frictional contact model remains physically appropriate for the dry-stacked interlocking CSEB system and provides a consistent basis for comparative assessment of mechanism development across the two wall types.

Perfect bond

A perfect bond assumption enforces displacement continuity across the interface (no opening and no sliding), typically via *tie* constraints (Lourenço, 1996). This idealisation is computationally efficient but cannot reproduce joint-governed mechanisms and is therefore not suitable when sliding/opening dominates the response.

Frictional contact

For dry or debonded interfaces, contact is defined by: (i) *hard* (unilateral) normal contact preventing interpenetration in compression and allowing separation in tension, and (ii) *tangential* behaviour governed by Coulomb friction. In its simplest form, the shear limit is

$$\tau \leq \mu\, p, \tag{3.15}$$

where τ is the interface shear traction, p is the compressive contact pressure, and μ is the friction coefficient. This formulation captures separation, re-contact and sliding under compressive normal stress, but it does not represent initial bond or its progressive degradation; it therefore corresponds primarily to post-debonding behaviour (Lourenço et al., 1995).

Cohesive traction-separation

The concept of cohesive zone modelling was originally proposed by Dugdale (1960) and later extended by Barenblatt (1962). In masonry analysis, the response of interfaces such as bed and head joints is commonly represented using either cohesive elements or cohesive contact formulations. In this study, the surface-based cohesive behaviour available in ABAQUS was adopted to represent the cohesive interface response. This formulation accounts for the two primary failure mechanisms: tensile opening/debonding (Mode I) and shear sliding in-plane and out-of-plane (Modes II-III). The constitutive response follows a traction-separation law with three sequential stages: (i) linear elastic traction-separation, (ii) damage initiation, and (iii) damage evolution.

In the initial elastic regime, the response is defined by a penalty stiffness relation,

$$\begin{bmatrix} t_n \\ t_s \\ t_t \end{bmatrix} = \begin{bmatrix} K_{nn} & 0 & 0 \\ 0 & K_{ss} & 0 \\ 0 & 0 & K_{tt} \end{bmatrix} \begin{bmatrix} \delta_n \\ \delta_s \\ \delta_t \end{bmatrix}, \tag{3.16}$$

where K_{nn} is the normal stiffness, and K_{ss} and K_{tt} are the shear stiffness components in the two tangential directions. Here, $\mathbf{t}$ are the nominal tractions and $\boldsymbol{\delta}$ are the separations in the normal and two shear directions across the interface.

Damage initiation is commonly defined by a traction-based criterion. In practice, this means that damage starts when an effective traction reaches the adopted interface strength (SIMULIA, 2024h). After damage initiation, the interface stiffness is degraded through a scalar damage variable D. The penalty relation can then be written as

$$\mathbf{t} = (1 - D)\,\mathbf{K}\,\boldsymbol{\delta}, \tag{3.17}$$

where $D = 0$ corresponds to an intact interface and $D = 1$ corresponds to complete loss of cohesive capacity.

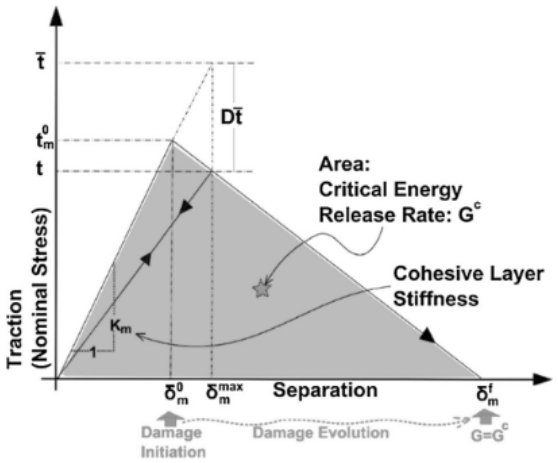

Figure 3.8: Traction-separation law for a cohesive zone model with linear softening and fracture energy G_c (Haddad and Sepehrnoori, 2016).

In ABAQUS, damage evolution can be defined using a fracture-energy-based formulation with linear softening (Figure 3.8) (SIMULIA, 2024h). In that case, D is conveniently expressed in terms of an effective separation measure,

$$D = \frac{\delta_m^f \left(\delta_m^{\max} - \delta_m^0\right)}{\delta_m^{\max}\left(\delta_m^f - \delta_m^0\right)}, \tag{3.18}$$

where δ_m^0 is the effective separation at the onset of damage, $\delta_m^{\max}$ is the maximum effective separation reached during loading, and δ_m^f is the effective separation at failure.

For an energy-based law with linear softening, the failure separation is related to the critical fracture energy G_c and the effective traction at damage initiation, T_{eff}^0 (denoted

t_m^0 in Figure 3.8), as

$$\delta_m^f = \frac{2G_c}{T_{\text{eff}}^0}. \tag{3.19}$$

The fracture energy G_c represents the area under the traction-separation curve for the selected softening law (SIMULIA, 2024h).

3.3.4 Practical considerations and modelling choice

The choice of interface stiffness and softening parameterisation influences both the mechanical response and numerical stability. High stiffness values reduce elastic compliance and may be needed to avoid unrealistically large separations prior to damage, but excessively stiff interfaces can cause poor conditioning when combined with material softening and contact.

The specific interface/contact idealisation adopted in the present study, together with the chosen parameter values, is defined in the subsequent method section.

3.4 Boundary conditions and loading idealisations

The in-plane response of masonry wall panels is strongly affected by boundary restraint provided by adjacent structural components (e.g. diaphragms and ring beams). Since the degree of diaphragm coupling in practice is uncertain and varies between buildings, two limiting boundary condition cases are considered to bracket the likely response: a *cantilever* condition (weak restraint) and a *fixed-fixed* condition (strong restraint) (Government of Nepal et al., 2016; Lourenço, 1996).

In the cantilever idealisation, the panel is fully restrained at the base while the top edge is free to rotate, representing limited diaphragm coupling. This boundary condition promotes a single-curvature deformation shape, with maximum bending demand near the base, and therefore tends to accentuate toe crushing/rocking-type mechanisms and base-region damage localisation.

In the fixed-fixed idealisation, both the base and the top edge are restrained against rotation, representing strong coupling to surrounding structural elements. This condition promotes a double-curvature deformation shape, alters the moment distribution and increases restraint-induced shear demand, which may shift damage localisation away from the base and modify the governing failure mechanism.

These two idealisations are used as bounding cases to evaluate sensitivity of capacity and failure mode to boundary restraint. Real buildings are expected to exhibit intermediate behaviour between these extremes depending on diaphragm stiffness, anchorage details and ring-beam action (Government of Nepal et al., 2016; Petry and Beyer, 2014).

3.5 FE-software

Finite element simulations are performed in ABAQUS. The solution procedure (implicit versus explicit) is not a cosmetic software choice; it directly affects numerical robustness for problems dominated by contact, stiffness degradation and softening. ABAQUS distinguishes between ABAQUS/Standard (implicit) and ABAQUS/Explicit (explicit time integration) procedures (SIMULIA, 2024g).

3.5.1 Implicit solution procedure (ABAQUS/Standard)

Implicit procedures solve for equilibrium at each increment through an iterative scheme and are efficient for many quasi-static problems when the stiffness remains well-conditioned. However, in strongly nonlinear problems involving changing contact status and softening damage, the global equilibrium iterations may experience convergence difficulties and repeated cut-backs, potentially preventing completion of the analysis (SIMULIA, 2024g). For DMM masonry models with frictional contact interfaces and damage-based constitutive laws, these difficulties are a practical limitation.

3.5.2 Explicit time integration (ABAQUS/Explicit)

ABAQUS/Explicit advances the solution using conditionally stable explicit time integration without global equilibrium iterations. This makes it well suited for severe nonlinearities such as complex contact interactions and progressive stiffness degradation, at the cost of small stable time increments controlled by element size and material properties (SIMULIA, 2024l). Given that the present models include multiple contacting interfaces and softening behaviour, ABAQUS/Explicit is adopted as the baseline solver to improve robustness of the nonlinear simulations.

Quasi-static use of an explicit solver

Although explicit integration is inherently dynamic, it can be used to approximate quasi-static response by applying loading sufficiently slowly such that inertial effects remain negligible compared with the internal resisting mechanisms. In this work, quasi-static conditions are verified by monitoring the energy balance during the analysis: the kinetic energy is kept small relative to the internal energy throughout the loading history, and the response is checked for the absence of significant oscillations (SIMULIA, 2024k,n; Huang et al., 2023). Accordingly, time is used as a numerical load-control parameter rather than as a representation of the real earthquake time history.

4 Method

4.1 Overview of numerical procedure

This chapter describes the finite element modelling workflow adopted to evaluate the in-plane capacity and governing failure mechanisms of masonry piers constructed in interlocking CSEB and fired clay brick systems. All models are implemented in ABAQUS within a detailed micro-modelling (DMM) framework. To analyse the seismic behaviour of the masonry piers a displacement-controlled nonlinear static loading idealisation (pushover analysis) is employed.

4.1.1 Summary of workflow analysed configurations

The numerical study followed a consistent modelling workflow. First, the wall geometry was defined and discretised, and the masonry constituents were represented explicitly using a detailed micro-modelling approach. Material models were then assigned to the units, mortar joints and, where applicable, grout, while the interaction between adjacent constituents was defined through the selected interface formulation. Subsequently, boundary conditions and the vertical precompression were applied, and the lateral response was obtained by imposing a prescribed displacement history in ABAQUS/Explicit under quasi-static conditions. Finally, the response was post-processed in terms of base shear and drift, and the governing mechanisms were identified from the resulting damage patterns.

As discussed in Section 2.4.4, the in-plane response of masonry depends on several key parameters. To capture these effects, a set of analyses was carried out in ABAQUS. All analyses are summarised in Table 4.1. Each case ID in Table 4.1 correspond to one ABAQUS model (one geometry, one material system and one boundary-condition idealisation) and one monotonic pushover run.

Table 4.1: Summary of the numerical model matrix. Each row corresponds to one ABAQUS model configuration and one pushover analysis.

Model / specimen	Material system	Reinforcement	Width L (mm)	Height h (mm)	h/L	Pre-compression	Boundary condition
FF URM LOW	CSEB	No	1650	1600	0.97	Low	Fixed-fixed
CL URM LOW	CSEB	No	1650	1600	0.97	Low	Cantilever
FF URM HIGH	CSEB	No	1650	1600	0.97	High	Fixed-fixed
CL URM HIGH	CSEB	No	1650	1600	0.97	High	Cantilever
FF RM LOW	CSEB	Yes	1650	1600	0.97	Low	Fixed-fixed
CL RM LOW	CSEB	Yes	1650	1600	0.97	Low	Cantilever
FF RM HIGH	CSEB	Yes	1650	1600	0.97	High	Fixed-fixed
CL RM HIGH	CSEB	Yes	1650	1600	0.97	High	Cantilever
FF URM LOW	CSEB	No	900	1800	2.00	Low	Fixed-fixed
CL URM LOW	CSEB	No	900	1800	2.00	Low	Cantilever
FF URM HIGH	CSEB	No	900	1800	2.00	High	Fixed-fixed
CL URM HIGH	CSEB	No	900	1800	2.00	High	Cantilever
FF RM LOW	CSEB	Yes	900	1800	2.00	Low	Fixed-fixed
CL RM LOW	CSEB	Yes	900	1800	2.00	Low	Cantilever
FF RM HIGH	CSEB	Yes	900	1800	2.00	High	Fixed-fixed
CL RM HIGH	CSEB	Yes	900	1800	2.00	High	Cantilever
FF LOW	Fired brick	No	1620	1598	0.99	Low	Fixed-fixed
CL LOW	Fired brick	No	1620	1598	0.99	Low	Cantilever
FF HIGH	Fired brick	No	1620	1598	0.99	High	Fixed-fixed
CL HIGH	Fired brick	No	1620	1598	0.99	High	Cantilever
FF LOW	Fired brick	No	870	1732	1.99	Low	Fixed-fixed
CL LOW	Fired brick	No	870	1732	1.99	Low	Cantilever
FF HIGH	Fired brick	No	870	1732	1.99	High	Fixed-fixed
CL HIGH	Fired brick	No	870	1732	1.99	High	Cantilever

4.2 Solver and quasi-static strategy (ABAQUS/Explicit)

All analyses were performed using ABAQUS/Explicit. The explicit procedure was chosen because the models contain strong nonlinearities, mainly due to changing contact conditions with opening, re-contact and sliding, combined with stiffness degradation and softening of the constituent materials. In preliminary trials, these features often led to convergence difficulties in implicit static analyses in ABAQUS/Standard, whereas explicit integration avoids global equilibrium iterations and is therefore more robust for contact-dominated softening problems (SIMULIA, 2024g,l).

Since ABAQUS/Explicit is inherently dynamic, quasi-static conditions were obtained by applying the prescribed displacement history sufficiently slowly, and by using a smooth-step amplitude (See Figure 4.1) to reduce spurious accelerations at the beginning and end of the loading. Quasi-static behaviour was then verified from the energy balance, where the kinetic energy (ALLKE) remained below approximately 5-10% of the internal energy (ALLIE) during the main loading phase (SIMULIA, 2024k,n). The response was also inspected to confirm that no significant oscillations affected the pushover curves (SIMULIA, 2024n). In this context, the analysis time served only as a numerical parameter that controlled the loading rate, and it was not intended to represent an earthquake time history.

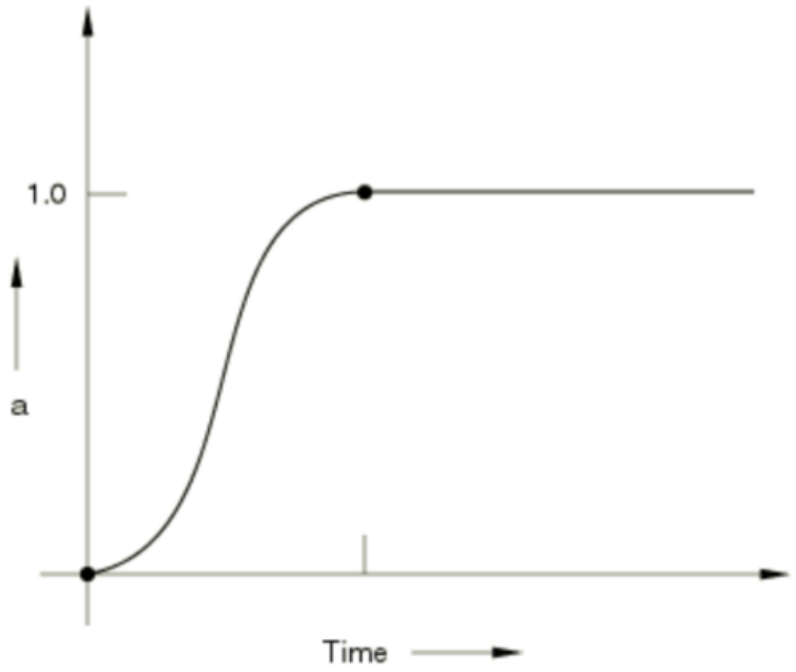

Figure 4.1: Smooth-step amplitude that was used for quasi-static loading in ABAQUS/Explicit based on SIMULIA (2024g).

4.3 Model configurations and modelling approach

A detailed micro-modelling (DMM) strategy was adopted to capture crack initiation and propagation not only in the units, but also in the mortar and grout. This approach also enables an explicit representation of interface-governed mechanisms, such as joint opening and sliding. Masonry units, mortar/grout and reinforcement (when present) were modelled as separate components. Interfaces between adjacent bodies were represented explicitly through contact descriptions. Figure 4.2 illustrates the adopted DMM layout for fired clay brick masonry.

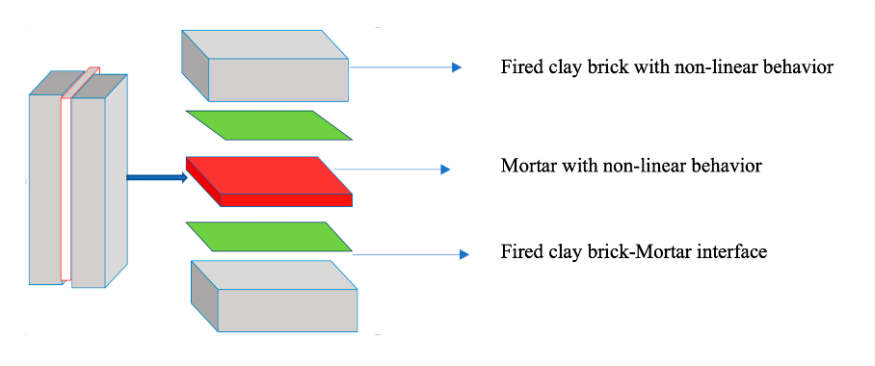

Figure 4.2: Adopted detailed micro-modelling (DMM) layout for fired clay brick masonry based on Hernoune et al. (2020).

4.3.1 Reinforced cases

Reinforcement was included only in the dedicated reinforced configuration. The aim was not to optimise detailing, but to quantify the effect of vertical bars on the pier response under monotonic in-plane loading. Only vertical reinforcement was modelled, placed in grouted cores at (i) the two pier end regions and (ii) at wall junctions/opening jambs where applicable, consistent with the prescriptive intent of NBC 202/NBC 203 (NBC 202:2015; NBC 203:2015). All other configurations were modelled as URM.

4.4 Material modelling

This section describes how the material parameters used in the numerical models were obtained. The materials are CSEB, mortar/grout, fired clay brick, and steel reinforcement. Parameters for CSEB and mortar/grout were derived from laboratory tests performed in Nepal for this project. Fired clay brick parameters were adopted from published experimental studies, since no project-specific brick tests were available. Steel parameters were taken from the applicable reinforcement specification NBC 202:2015 and supporting literature. The processed curves and full input datasets are provided in section 4.4.1 and Appendix A.

4.4.1 Material Properties

Test-based parameters for CSEB and mortar/grout

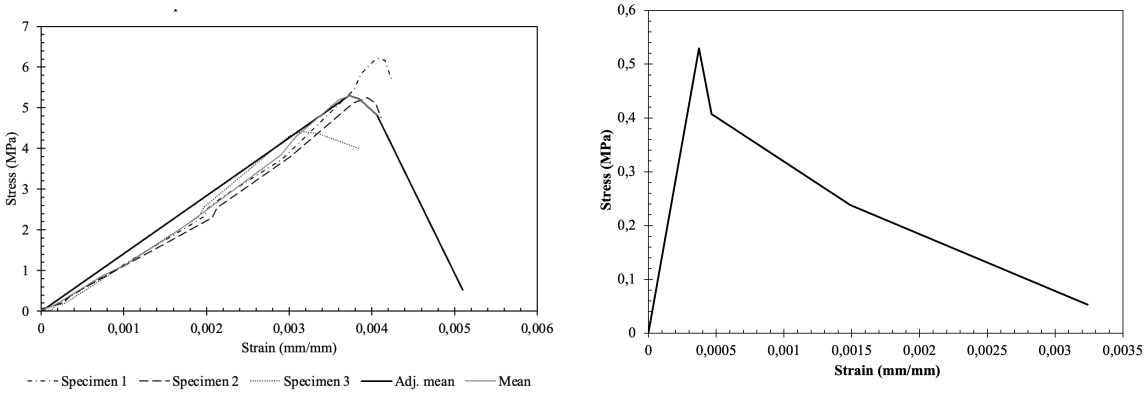

(a) Compressive stress-strain curve **(b)** Tensile stress-strain curve

Figure 4.3: Stress-strain curves for CSEB used as numerical input.

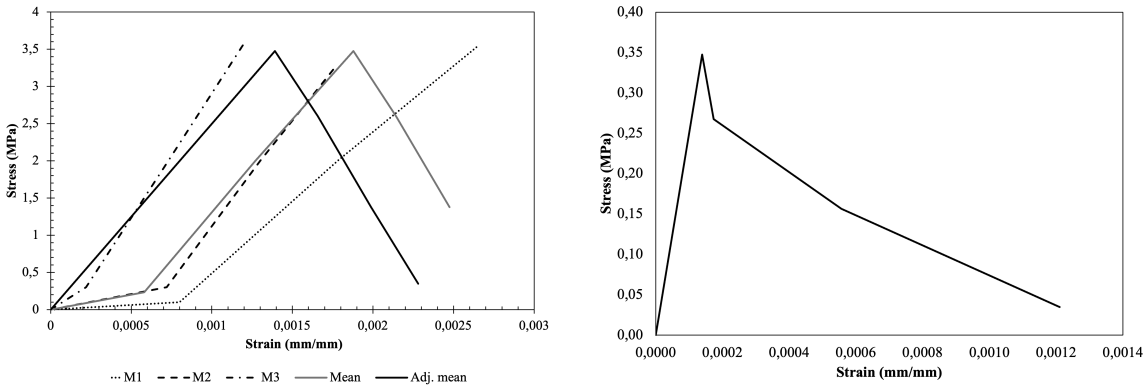

(a) Compressive stress-strain curve **(b)** Tensile stress-strain curve

Figure 4.4: Stress-strain curves for mortar 1:0:6/grout used as numerical input.

For both CSEB and mortar/grout, three uniaxial compression tests were available and reported as stress-strain curves. The curves were aligned in strain and averaged pointwise to obtain a representative mean curve for each material. Small adjustments were then applied to obtain smooth and numerically stable input in ABAQUS. Minor irregularities were removed and, where present, the initial seating part at very low stress was reduced. These adjustments did not increase the peak strength. The compressive stress-strain curve for CSEB is shown in Figure 4.3a, and the corresponding curve for mortar/grout is shown in Figure 4.4a.

A simplified post-peak branch was introduced for CSEB and mortar/grout to obtain a complete compressive response, including softening after peak. This is required later when defining stiffness degradation and damage in the ABAQUS constitutive model (see Section 4.4.2). The idealisation was kept simple and conservative.

The compressive strength f_c was taken as the peak stress of the representative curve. Young's modulus E was evaluated as a secant modulus in the quasi-linear range, computed between $\sigma = 0.10 f_c$ and $\sigma = \frac{1}{3} f_c$. The lower bound was used to reduce the influence of seating effects. For CSEB, axial and lateral strain measurements were also available, which allowed Poisson's ratio ν to be estimated from the initial approximately linear axial-lateral strain relation (See Figure 4.5).

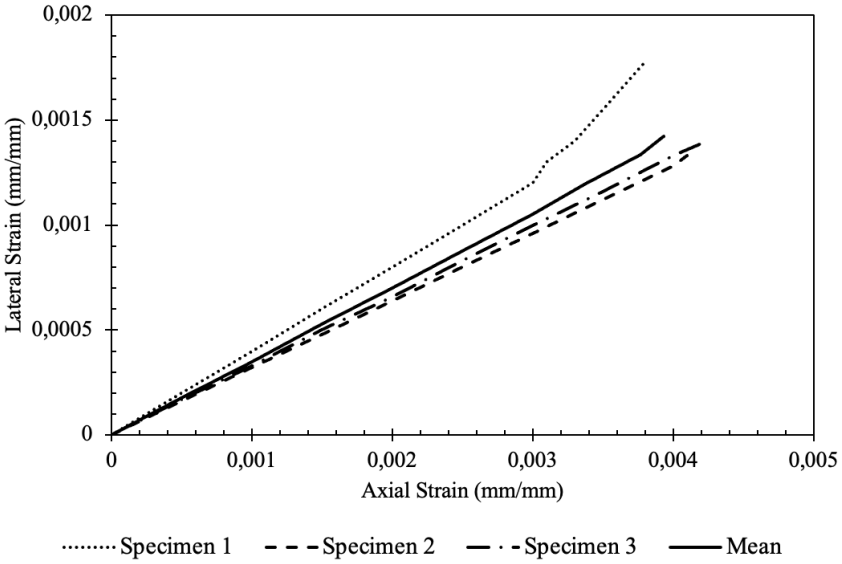

Figure 4.5: Lateral strain as a function of axial strain for three CSEB specimens tested in uniaxial compression. The solid line shows the pointwise mean curve used to estimate Poisson's ratio in the initial approximately linear strain range.

$$\nu = -\frac{\varepsilon_{\text{lat}}}{\varepsilon_{\text{ax}}}, \tag{4.1}$$

For mortar/grout, lateral strain was not measured and $\nu = 0.20$ was assumed, which is commonly used for mortar-like cementitious materials.

No direct tensile test data were available for CSEB and mortar/grout. The tensile response was therefore idealised for CDP using a simple tension-stiffening curve. The tensile strength was assumed as $f_t = 0.10 f_c$, and cracking was assumed to start at $\varepsilon_{cr} = f_t / E$. Beyond ε_{cr}, the post-cracking tensile response was idealised using a piecewise linear softening law with a Eurocode-inspired shape (Nafees et al., 2021), as illustrated in Figure 4.6. The resulting tensile stress-strain curves adopted for CSEB and mortar/grout are shown in Figure 4.3b and Figure 4.4b, respectively.

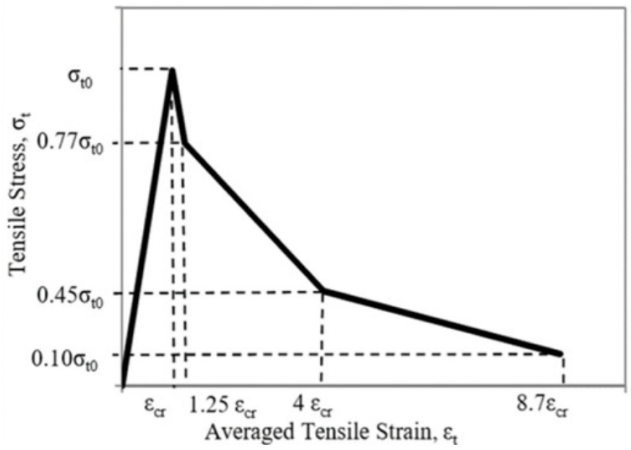

Figure 4.6: Idealised piecewise linear tensile softening law used to define post-cracking behaviour (Eurocode-inspired shape) (Nafees et al., 2021).

The material parameters for CSEB are summarised in Table 4.2, and the corresponding parameters for mortar/grout are summarised in Table 4.3.

Table 4.2: CSEB unit properties adopted in this study.

Symbol	Value	Unit
$size$	$300 \times 150 \times 100$	mm
ρ	1800	kg/m^3
ν	0.35	–
E_b	1421.2	MPa
$f_{c,b}$	5.29	MPa
$f_{t,b}$	0.529	MPa

Table 4.3: Grout/mortar properties adopted in this study.

Symbol	Value	Unit
ρ	2400	kg/m^3
ν	0.2	–
E_m	2498.5	MPa
f_c	3.48	MPa
f_t	0.348	MPa

Fired brick

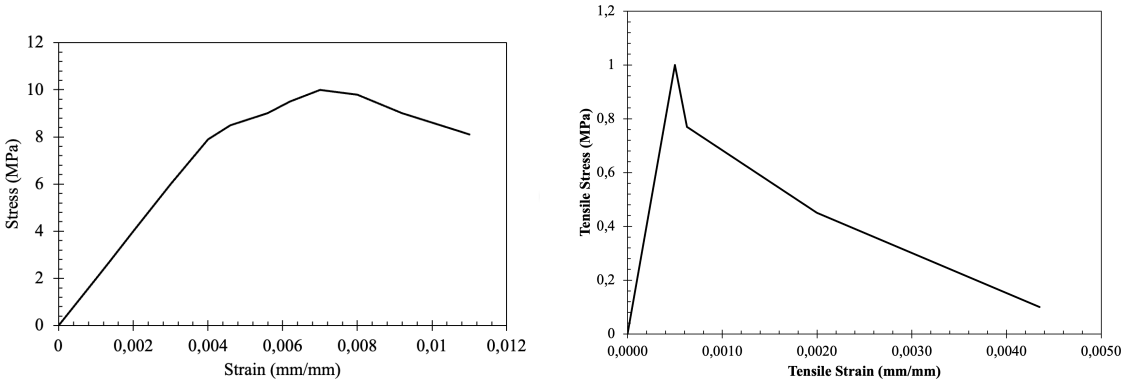

(a) Compressive stress-strain curve for fired clay brick adopted from Singh and Munjal (2017).

(b) Tensile stress-strain curve for fired clay brick.

Figure 4.7: Stress-strain relationships adopted for fired clay brick in compression and tension.

In the absence of laboratory testing within the present study, material properties for fired clay brick were established from published sources. Nepal Standard NS 1:2035 specifies that Class A fired bricks should achieve a minimum compressive strength of approximately 10 MPa (NS 1:2035). NBC 109 provides a general lower reference strength level of 3.5 MPa for bricks used in masonry (NBC 109:1994). These code values were used as contextual benchmarks.

For numerical modelling, the compressive stress-strain relationship and the elastic modulus E were adopted from the experimental results reported by Singh and Munjal (2017) (See Figure 4.7a). Since no project-specific lateral strain data were available for fired bricks, Poisson's ratio was assumed as $\nu = 0.20$, which is a commonly used value in masonry modelling when such data are missing.

Direct tensile test data were not available. Tensile behaviour was therefore defined in the same way as for CSEB and mortar/grout (See Figure 4.7b). The input data for the fired clay brick material are presented in Table 4.4.

Table 4.4: Fired brick unit properties adopted in this study.

Symbol	Value	Unit
$size$	$220 \times 115 \times 57$	mm
ρ	1750	kg/m^3
ν	0.20	–
E_b	2001	MPa
$f_{c,b}$	10.0	MPa
$f_{t,b}$	1.0	MPa

Reinforcement

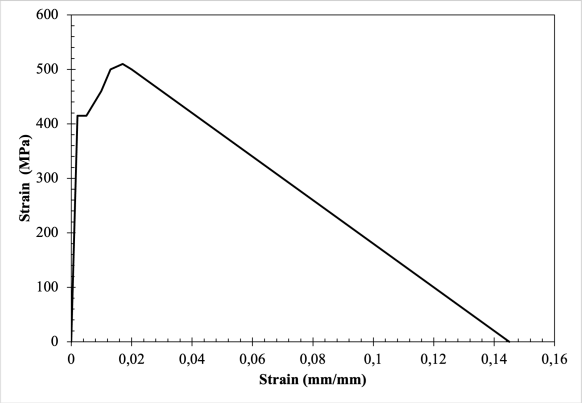

Figure 4.8: Tensile stress-strain curve for reinforcement adopted from (Sujitha et al., 2026).

Fe 415 steel was used for the vertical reinforcement, in accordance with the CSEB construction guidelines. The number 415 indicates the steel's yield strength of 415 MPa. In this study, the material properties and the stress-strain curve obtained from a tensile test of the Fe 415 steel are adopted from (Sujitha et al., 2026). The stress-strain curve shows linear elastic behaviour up to the yield strength of 415 MPa, followed by strain hardening to the ultimate tensile strength of 510 MPa, and a softening linear branch until failure. Failure is assumed to occur at an ultimate strain of 14.5%, in accordance with the minimum elongation requirement for Fe 415 steel (NBC 202:2015). The tensile stress-strain curve is illustrated in Figure 4.8, and the corresponding material properties of the Fe 415 steel are summarised in Table 4.5.

Table 4.5: Reinforcement properties adopted in this study.

Symbol	Value	Unit
diameter	12	mm
ρ	7850	kg/m^3
ν	0.30	–
E_r	200	GPa
σ_y	415	MPa
σ_D	510	MPa

4.4.2 Concrete Damaged Plasticity (CDP) parameters

To implement the test-based material data in ABAQUS, the stress-strain curves were converted into the input format required by the Concrete Damaged Plasticity (CDP) model. This section summarises how the concrete plasticity parameters were selected and how the tensile and compressive damage variables were defined for the analyses.

Concrete plasticity parameters

The CDP yield surface and flow potential were defined according to standard ABAQUS conventions (SIMULIA, 2024d). The initial biaxial-to-uniaxial compressive yield stress ratio was taken as $\sigma_{b0}/\sigma_{c0} = 1.16$. The yield surface shape parameter was set to $K_c = 2/3$ (Bui et al., 2020; SIMULIA, 2024d; Doran et al., 2023). The eccentricity was defined as $\epsilon = 0.1$. A viscosity parameter can be used in CDP to improve numerical stability in the softening regime; here it was set to $\mu_v = 0$ to avoid introducing additional artificial dissipation.

The dilation angle ψ was estimated from an internal friction angle φ using the approximation proposed by Borst and Vermeer (1984):

$$\mu_f = \tan(\varphi), \tag{4.2}$$

$$\psi = \varphi - 20^\circ. \tag{4.3}$$

For interlocking CSEB, a friction coefficient of $\mu_f = 0.733$ was adopted from dry-stack tests reported by Sturm et al. (2014), which yields $\psi \approx 16^\circ$. The same value was assumed for mortar/grout due to the similar cement-based composition. For fired clay brick, $\psi = 7^\circ$ was adopted based on the CDP calibration used by Agüera et al. (2016).

Concrete damage parameters

Damage evolution primarily influences the post-peak softening response. To maintain numerical stability and avoid complete loss of stiffness at full damage, the damage variables were limited to a maximum value of

$$d_{\max} = 0.9. \tag{4.4}$$

Since unloading-reloading test data were not available, the tensile and compressive damage variables were defined using the simplified relations proposed by Nastri et al. (2023):

$$d_t = 1 - \frac{\sigma}{\sigma_{t0}}, \qquad d_c = 1 - \frac{\sigma}{\sigma_{cu}}. \tag{4.5}$$

The complete CDP input datasets, including the compression stress-inelastic strain and tension stress-cracking strain relationships together with the corresponding damage variables, are provided in Appendix A.

4.4.3 Reinforcement constitutive model and ductile damage

Damage initiation was defined using the ABAQUS ductile damage criterion (SIMULIA, 2024c). Damage initiation was assumed to start at the onset of softening in the adopted tensile curve, i.e. at the peak stress $\sigma = 510$ MPa. The corresponding plastic strain at this point was taken as $\varepsilon_D^{pl} = 0.01445$. For uniaxial tension, the stress triaxiality was taken as $\eta = 1/3$. The tensile test is quasi-static, therefore strain-rate effects were neglected and $\dot{\varepsilon}^{pl} = 0$. The ductile damage initiation inputs used in ABAQUS are summarised in Table A.3.

After damage initiation, damage evolution was defined using a displacement-based formulation with linear softening (SIMULIA, 2024a). The characteristic length was taken as the reinforcement element length in the adopted mesh: $L_c = 0.0323$ m for the slender wall and $L_c = 0.0322$ m for the squat wall. Failure was defined by an ultimate equivalent plastic displacement $\bar{u}_f^{pl}$, computed as

$$\bar{u}_f^{pl} = L_c \left(\bar{\varepsilon}_f^{pl} - \bar{\varepsilon}_D^{pl} \right). \tag{4.6}$$

From the adopted tensile curve, failure occurs at a total strain of 0.145. At zero stress, the elastic strain contribution is zero, so $\bar{\varepsilon}_f^{pl} = 0.145$. See Table A.3 for the calculated input values of $\bar{u}_f^{pl}$ for the squat and slender walls, respectively.

Plasticity and ductile damage parameters for Fe 415 steel were implemented in ABAQUS. The adopted input tables are provided in Table A.3.

4.5 Element type and mesh

Masonry units (CSEB and fired clay brick) and mortar/grout were modelled using three-dimensional solid elements of type C3D8R in ABAQUS, while the reinforcement bars were modelled using two-node truss elements (T3D2). C3D8R is an eight-node linear brick element. The nodes represent the locations in the model where displacements can occur and are therefore essential for describing the structural response (SIMULIA, 2024e,i,o).

The global mesh was kept as coarse as possible to reduce computational time. Local mesh refinement was applied around the holes and interlocking features in the CSEB units, where stress concentrations were expected. For the fired clay brick models, the mortar joints were initially meshed more finely, however, this significantly increased the runtime. The final model therefore used a single element through the joint thickness as a practical compromise.

In the CSEB models, the grout mesh was adapted to match the surrounding CSEB geometry as closely as possible. The reinforcement was then meshed to be compatible with the grout mesh. The CSEB geometry required several partitions and local seed adjustments to obtain predominantly hexahedral and reasonably regular elements while keeping the minimum element size controlled. Representative mesh visualisations are provided in Appendix C.

4.6 Interactions

After assembling the model, interactions were defined using General Contact. This approach automatically includes all relevant surfaces and reduces the need to define a large number of individual contact pairs, which is beneficial for complex geometries with many potential interactions (SIMULIA, 2024f). The mechanical behaviour assigned to the different interfaces is summarised below.

4.6.1 CSEB-CSEB (dry-stacked contact)

The contact between CSEB blocks was modelled as dry-stacked, upon request from Build Up Nepal. Normal and tangential contact behaviour were defined, while cohesive behaviour was excluded since no physical adhesion between blocks was assumed.

In the normal direction, hard contact was used to prevent interpenetration and to allow separation when the contact pressure vanished. In the tangential direction, Coulomb friction was adopted. Based on experimental testing of stabilised interlocking CSEB in a dry-stack configuration, a friction coefficient of $\mu = 0.733$ was used (Sturm et al., 2014).

4.6.2 Fired Brick-Mortar

Surface-based cohesive behaviour was used to represent the interface response between fired clay brick units and mortar to capture both the joint capacity and progressive degradation (SIMULIA, 2024h). This approach was adopted because fired-clay brick walls were expected to exhibit joint debonding and sliding, which cannot be captured by frictional contact alone prior to loss of cohesion. The constitutive behaviour follows a traction-separation law consisting of (i) an initial linear elastic response, (ii) damage initiation, and (iii) damage evolution (SIMULIA, 2024h).

Accurate determination of interface parameters requires experimental testing, including shear, flexural, and tensile test configurations. No experimental determination of the interface parameters was performed in this study. The normal stiffness, k_{nn}, and the shear stiffnesses, k_{ss} and k_{tt}, were therefore computed using the relations proposed by Dolatshahi and Aref (Dolatshahi and Aref, 2011):

$$\frac{1}{k_{nn}} = 2\left(\frac{h_m}{E_m} + \frac{h_b}{E_b}\right), \qquad \frac{1}{k_{ss}} = 2\left(\frac{h_m}{G_m} + \frac{h_b}{G_b}\right), \qquad k_{ss} = k_{tt}. \tag{4.7}$$

Here, E_b, G_b, and h_b are the elastic modulus, shear modulus, and thickness of the brick, while E_m, G_m, and h_m are the corresponding properties and thickness of the mortar. The shear modulus G was computed as

$$G = \frac{E}{2(1+\nu)}, \tag{4.8}$$

where ν is Poisson's ratio. The normal stiffness was obtained as $k_{nn} = 1.539 \times 10^{10}$ N/m^3 and the shear stiffness values were calculated as $k_{ss} = k_{tt} = 6.4126 \times 10^9$ N/m^3.

For damage initiation, the peak nominal tractions in the normal and tangential directions, t_n^0, t_s^0, and t_t^0, were defined. These parameters represent the maximum interface stresses in normal tension and in the two shear directions. The normal peak traction t_n^0 was taken as the tensile strength of the interface. The tensile strength was derived from flexural bond strength data reported in an experimental study on brick masonry

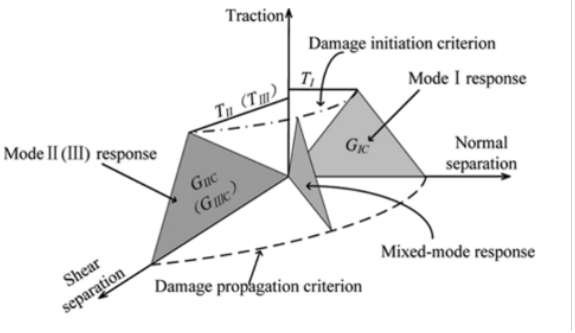

Figure 4.9: Mixed-mode traction-separation behaviour of a cohesive interface with damage initiation at T_i and energy-based propagation (G_{Ic}, G_{IIc}) using the Benzeggagh-Kenane criterion (Benzeggagh and Kenane, 1996).

with comparable brick-mortar properties (Singh and Munjal, 2017). The reported flexural bond strengths were 0.119 MPa and 0.158 MPa. The average value, 0.14 MPa, was adopted as the interface tensile strength and used as t_n^0 in the cohesive model. However, it should be noted that the flexural bond test is based on bending rather than pure tension; the measured strength may therefore include shear effects and other test-related influences, which introduces uncertainty in the adopted value.

The peak shear tractions t_s^0 and t_t^0 were assumed equal due to the assumption of isotropic interface behaviour in shear. Following Lourenço (1996), the peak shear traction was taken as $t_s^0 = t_t^0 = 1.4 f_t$, where f_t is the interface tensile strength (i.e. t_n^0 in this study). The peak shear tractions were therefore computed as $t_s^0 = t_t^0 = 0.196$ MPa.

Damage evolution was defined using a fracture-energy-based formulation with linear softening in ABAQUS. The mixed-mode critical fracture energy G_c was evaluated using the Benzeggagh-Kenane criterion, which combines mode I and mode II/III fracture energy contributions (Benzeggagh and Kenane, 1996). This criterion is suitable when the shear fracture energies in the two tangential directions are equal, which is assumed here ($G_{IIc} = G_{IIIc}$); see Figure 4.9.

The mode I tensile fracture energy of the interface, G_{Ic}, was calculated using the expression recommended in Singh and Munjal (2017):

$$G_{Ic} = 0.025\,(2f_t)^{0.7} = 0.025\left(2t_n^0\right)^{0.7}. \tag{4.9}$$

Using the adopted tensile strength in Eq. (4.9), the mode I fracture energy was obtained as $G_{Ic} = 10.255$ N/m. This value lies within the range 5-20 N/m reported in the literature for masonry interfaces (Lourenço, 1996).

Lourenço (Lourenço, 1996) reports mode II shear fracture energy values for masonry interfaces in the range 0.01-0.25 N/mm (10-250 N/m). To avoid overestimating the shear capacity of the interface and to ensure a relatively brittle shear response, a value in the lower part of this interval was adopted. Accordingly, $G_{IIc} = G_{IIIc} = 50$ N/m (0.05 N/mm) was used in the present study.

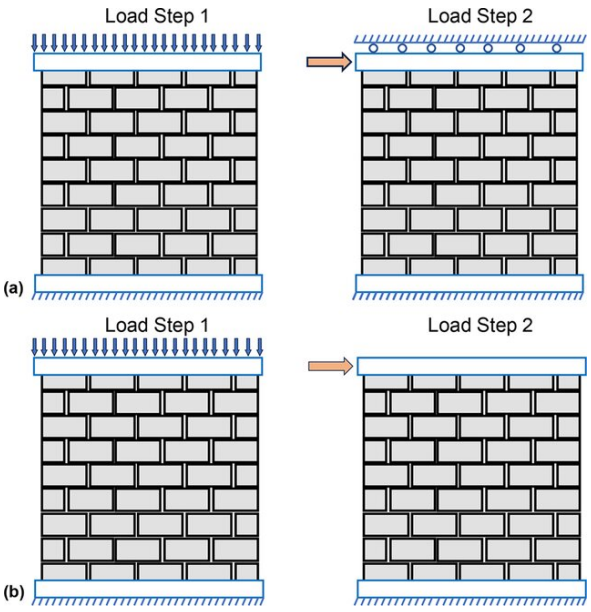

Figure 4.10: An illustration of load and boundry conditions for in-plane loaded piers (a) Fixed-fixed pier (b) Cantilever Pier adapted from Tariq et al. (2025).

4.6.3 CSEB-Grout

The interaction between the CSEB units and the grout was modelled using frictional contact only, without the inclusion of a cohesive interface (SIMULIA, 2024f,m). A friction coefficient of 0.6 was adopted. No laboratory tests were performed in the present study to determine the parameters required for a cohesive interface model. Cohesive behaviour was therefore not included to avoid overestimating the interface capacity.

4.6.4 Reinforcement-Grout

Reinforcement was connected to the surrounding grout using an "Embedded Region" constraint in ABAQUS (SIMULIA, 2024j). This approach assumes a perfect bond between the reinforcement (T3D2 element) and the grout (C3D8R element), meaning that the reinforcement follows the deformation of the grout without slip. The grout was defined as the host region, while the reinforcement elements were defined as the embedded region.

4.7 Boundary conditions

Two boundary condition idealisations, cantilever and fixed-fixed, were analysed to evaluate the influence of restraint conditions on the structural response of the wall elements. The base of the wall was fully fixed in all simulations, restraining all translations and rotations.

Boundary conditions at the top were applied through the rigid top beam used to

impose lateral displacement see 4.10. In the cantilever configuration, the top beam was allowed to translate in both the horizontal (x-direction) and vertical (y-direction) directions and to rotate in-plane about the z-axis. This allowed rocking and rotation of the wall during loading.

In the fixed-fixed configuration, the top beam was allowed to translate only in the horizontal direction (x-direction), while all other translations and rotations were restrained. This prevented rotation and vertical movement at the top, resulting in a more restrained deformation response.

The applied boundary conditions and corresponding ABAQUS input settings are summarised in Table 4.6.

Table 4.6: Boundary condition idealisations and ABAQUS implementation.

Idealisation	Physical meaning	ABAQUS implementation
Base (all cases)	Fixed support	ENCHASTRE: $U1 = U2 = U3 = UR1 = UR2 = UR3 = 0$
Cantilever (top)	Weak diaphragm restraint (top rotation allowed)	U3=UR1=UR2=0
Fixed-fixed (top)	Strong diaphragm restraint (top rotation restrained)	U2=U3=UR1=UR2=UR3=0

4.7.1 Coordinate system and loading direction

A global Cartesian coordinate system was used. The in-plane horizontal loading direction was aligned with the global **[X/Y]** axis, while the wall thickness direction was aligned with the global **[Z]** axis. Drift was evaluated as the lateral displacement of the top-beam reference point in the loading direction divided by the pier height.

4.8 Loads

4.8.1 Gravity and vertical pre-compression

Gravity was applied to the entire model using an acceleration of $g = 9.81$ m/s^2 to account for self-weight of the pier. To represent gravity loads from the overlying structure, a constant vertical pre-compression was also applied on the top surface of the pier. The vertical load comprised: (i) self-weight of masonry above the lintel band up to the roof band, (ii) self-weight of the lintel band and roof band, and (iii) the permanent roof load. The roof permanent load and the band material data were adopted from earlier Build Up Nepal case studies with the same building layout as considered herein (Thudén and Toivonen, 2018); the corresponding input values are summarised in Table 4.7.

Table 4.7: Input data used to establish the vertical load.

Component	Value
Lintel band density	2400 kg/m^3
Roof band density	2400 kg/m^3
Roof permanent load	0.157 kN/m^2
Tributary width (roof $\rightarrow$ long walls)	2.55 m

The combined vertical line load along the wall was converted to an equivalent uniform pressure by dividing by the wall thickness. For the low pre-compression level, the resulting top pressures used in the FE models were $p_{\text{CSEB}} = 16.4$ kPa for CSEB piers and $p_{\text{brick}} = 17.0$ kPa for fired-clay brick piers. A high pre-compression level was also considered and was taken as ten times the low level for both materials. A complete derivation of these values is provided in Appendix B.

4.8.2 Pushover loading (displacement control)

The in-plane pushover loading was applied through the rigid top beam. A reference point (RP) was defined at mid-span of the top beam, and the beam was modelled as a rigid body such that the RP governed the rigid-body motion of the beam. The lateral loading was introduced by prescribing a horizontal displacement at the RP using the smooth-step amplitude in Figure 4.1. Displacement control was used to ensure that the governing post-peak mechanism (e.g., rocking or sliding) could develop and be traced in a stable way. With force control, the analysis often becomes unstable and may lose equilibrium or fail to converge in the post-peak regime.

The target displacement was varied between simulations to avoid unnecessary runtime once peak capacity and the governing post-peak mechanism had been captured. Accordingly, analyses were terminated after clear strength degradation or once a stable mechanism plateau had developed. Depending on the case, the imposed displacement was limited to approximately 10-30 mm.

4.8.3 Steps

Each model was analysed using two sequential Explicit steps, see 4.10. In Step 1 (gravity and pre-compression), gravity ($g = 9.81$ m/s^2) was applied to account for pier self-weight and the vertical pre-compression was ramped to its target value. In Step 2 (pushover), the vertical pre-compression was kept constant and the in-plane response was driven by prescribing a horizontal displacement at the top-beam reference point using the smooth-step amplitude in Figure 4.1. The total step time was selected to ensure quasi-static conditions, which were verified from the energy balance (Section 4.2).

4.9 Response measures and post-processing

This section defines what was extracted from the simulations and how the results were interpreted. In Chapter 5, the response is presented as pushover curves together with the observed failure mechanisms and a drift-based reference check.

4.9.1 Global response and peak capacity

The pushover curves were constructed from the horizontal reaction force and displacement at the loading reference point (RF and U). Peak lateral capacity was defined as the maximum value of the lateral reaction force extracted at the reference point,

$$V_{\max} = \max(V). \tag{4.10}$$

Where post-peak degradation occurred, the response beyond peak was interpreted qualitatively, since softening can be sensitive to modelling assumptions.

4.9.2 Drift-based reference limit (NBC 105:2020)

To relate the pushover response to a simple code-based performance measure, a drift limit from NBC 105:2020 was used as a reference check. NBC 105:2020 specifies a storey drift limit at ULS of 2.5% (NBC 105:2020). For each pier, the corresponding displacement threshold was computed as

$$u_{\max} = 0.025\, h_{\text{pier}}. \tag{4.11}$$

This threshold was used together with $V_{\max}$ and the observed mechanism when interpreting the results in Chapter 5.

Table 4.8: Drift capacity for the studied piers.

Pier	h_{pier} (m)	$u_{\max}$ (m)
Squat CSEB (UR and R)	1.600	0.040
Slender CSEB (UR and R)	1.800	0.045
Squat fired clay brick	1.598	0.040
Slender fired clay brick	1.732	0.043

4.9.3 Ductility

In this study, the displacement ductility is used to compare the deformation capacity of the specimens after yielding. Since the measured load-displacement curves do not exhibit a distinct yield point, the ductility capacity was determined using an idealised procedure proposed by Shannag and Alhassan (2005), illustrated in Figure 4.11.

In this method, the yield displacement is determined using two straight reference lines drawn on the load-displacement curve. The first line is obtained by extending the line

connecting the origin and the point corresponding to 50% of the ultimate load, P_u. The second line is a horizontal line drawn through the point corresponding to 80% of P_u (taken as the failure level in this study). The intersection of these two lines defines the yield displacement, denoted u_y.

The maximum displacement u_f was determined as the displacement corresponding to 80% of the peak load on the descending branch of the curve. For responses that did not drop to 80% of the peak load after reaching the maximum load, the failure displacement was instead determined using drift limits. Walls governed by rocking were assigned a maximum drift of 0.6%, while walls governed by shear failure were assigned a maximum drift of 0.4%. In these cases, the second reference line was drawn at the displacement corresponding to the adopted failure point. The displacement ductility μ was then calculated as

$$\mu = \frac{u_f}{u_y}. \tag{4.12}$$

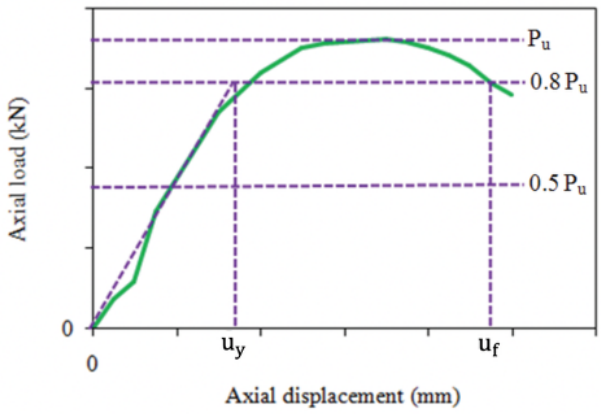

Figure 4.11: Idealised procedure for determining yield and ultimate displacements for ductility evaluation taken from (Marthong, 2018).

4.9.4 Energy absorption

In this study, the toughness of the analysed models is evaluated using the force-displacement curves obtained from pushover analyses. The absorbed energy is defined as the area under the force-displacement curve up to the displacement corresponding to the failure criterion used in this study. The area under the curve represents the total work absorbed by the structure during loading and is used as an indicator of the structural toughness. This allows a comparison of the energy absorption capacity between the different models.

Since the results are obtained as discrete data points from the numerical analysis, the area under the curve is calculated using the trapezoidal method. In this method, the area between two consecutive points on the curve is approximated as a trapezoid, and the total absorbed energy is obtained by summing the areas of all trapezoids along the curve. See Chapter 5 for the results.

4.9.5 Output requests

History outputs were requested to (i) build pushover curves and (ii) verify quasi-static conditions. The quasi-static check was based on the energy balance, primarily ensuring that ALLKE remained small compared to ALLIE. Field outputs were requested to interpret the failure mechanisms. CDP outputs (tension/compression damage and plastic strain measures) were used together with contact outputs from General Contact (normal pressure and separation/slip) to identify cracking/crushing localisation and sliding/rocking behaviour. These outputs form the basis for the plots and mechanism descriptions reported in Chapter 5 and Appendix D.

5 Results

The following section presents the experimental results from the pushover analysis, with emphasis on the behaviour of reinforced CSEB (RM) piers in comparison with unreinforced CSEB (URM) and fired brick piers. Tables 5.1-5.4 summarise the main response parameters obtained from the experimental programme for both squat and slender specimens.

In the tables, FF denotes fixed-fixed boundary conditions and CL denotes cantilever boundary conditions, while LOW and HIGH refer to low and high pre-compression, respectively. The symbol V_p denotes the peak lateral load and Δ_p the corresponding lateral displacement. V_{80} denotes the lateral load corresponding to 80% of the peak load on the descending branch, and Δ_f the associated displacement. The parameter θ_f represents the drift at failure, whereas θ_{lim} denotes the adopted drift limit in cases where the response did not reach the 80% post-peak criterion. Furthermore, Δ_y denotes the yield displacement, μ the displacement ductility, and E_{abs} the absorbed energy, calculated as the area under the load-displacement curve.

Table 5.1: CSEB squat walls (URM/RM), low and high pre-compression ($H = 1.6$ m).

Type	Failure mode	V_p [kN]	Δ_p [mm]	V_{80} [kN]	θ_{lim} [%]	Δ_f [mm]	θ_f [%]	Δ_y [mm]	μ [-]	E_{abs} [J]
FF URM LOW	–	26.33	4.070	21.06	–	4.604	0.29	2.427	1.90	78.78
FF RM LOW	–	27.81	3.620	22.25	–	4.804	0.300	2.160	2.22	92.50
CL URM LOW	Rocking	5.83	4.998	–	0.60	9.600	0.60	0.638	15.05	50.11
CL RM LOW	–	9.13	5.239	7.31	–	7.510	0.469	1.250	6.01	54.80
FF URM HIGH	–	36.94	2.287	29.55	–	3.689	0.23	1.053	3.50	99.24
FF RM HIGH	–	39.47	2.980	31.57	–	3.290	0.206	1.430	2.30	96.90
CL URM HIGH	–	21.33	3.606	17.07	–	9.410	0.23	0.988	9.53	165.91
CL RM HIGH	–	24.85	4.344	19.88	–	7.559	0.472	1.228	6.16	147.80

Table 5.2: CSEB slender walls (URM/RM), low and high pre-compression ($H = 1.8$ m).

Type	Failure mode	V_p [kN]	Δ_p [mm]	V_{80} [kN]	θ_{lim} [%]	Δ_f [mm]	θ_f [%]	Δ_y [mm]	μ [-]	E_{abs} [J]
FF URM LOW	–	14.52	5.10	11.61	–	7.762	0.431	3.255	2.38	78.95
FF RM LOW	–	15.90	4.34	12.72	–	6.150	0.342	3.310	1.86	62.00
CL URM LOW	–	1.12	0.91	0.893	–	0.9254	0.051	0.5337	1.73	0.612
CL RM LOW	–	5.27	10.199	4.217	–	14.732	0.818	4.436	3.32	55.90
FF URM HIGH	–	19.29	4.247	15.43	–	4.9935	0.277	2.406	2.08	62.22
FF RM HIGH	–	18.86	3.99	15.09	–	5.400	0.300	2.380	2.27	68.30
CL URM HIGH	–	5.26	10.80	5.259	0.60	10.80	0.60	1.633	6.61	48.37
CL RM HIGH	–	9.76	15.00	7.805	–	15.46	0.859	4.180	3.70	131.0

Table 5.3: Fired brick squat walls, low and high pre-compression ($H = 1.598$ m).

Type	Failure mode	V_p [kN]	Δ_p [mm]	V_{80} [kN]	θ_{lim} [%]	Δ_f [mm]	θ_f [%]	Δ_y [mm]	μ [-]	E_{abs} [J]
FF LOW	–	14.93	2.2515	11.94	–	2.52046	0.16	1.3694	1.84	23.90
CL LOW	–	3.733	0.6550	2.986	–	0.71648	0.04	0.4780	1.50	1.54
FF HIGH	–	15.62	2.0670	12.49	–	7.6307	0.48	1.1157	6.84	99.96
CL HIGH	–	12.53	6.1058	10.03	–	7.4320	0.47	1.2570	5.91	77.35

Table 5.4: Fired brick slender walls, low and high pre-compression ($H = 1.732$ m).

Type	Failure mode	V_p [kN]	Δ_p [mm]	V_{80} [kN]	θ_{lim} [%]	Δ_f [mm]	θ_f [%]	Δ_y [mm]	μ [-]	E_{abs} [J]
FF LOW	–	7.7588	6.8286	6.2070	–	8.783	0.51	2.35	3.74	52.30
CL LOW	–	1.1997	0.910775	0.9598	–	1.15	0.07	0.659	1.75	0.87
FF HIGH	Shear	7.6630	4.1166	7.2706	0.4	6.928	0.40	1.78	3.89	43.52
CL HIGH	Rocking	3.6118	7.8300	3.4800	0.6	10.392	0.60	1.84	5.65	32.19

5.1 Squat piers

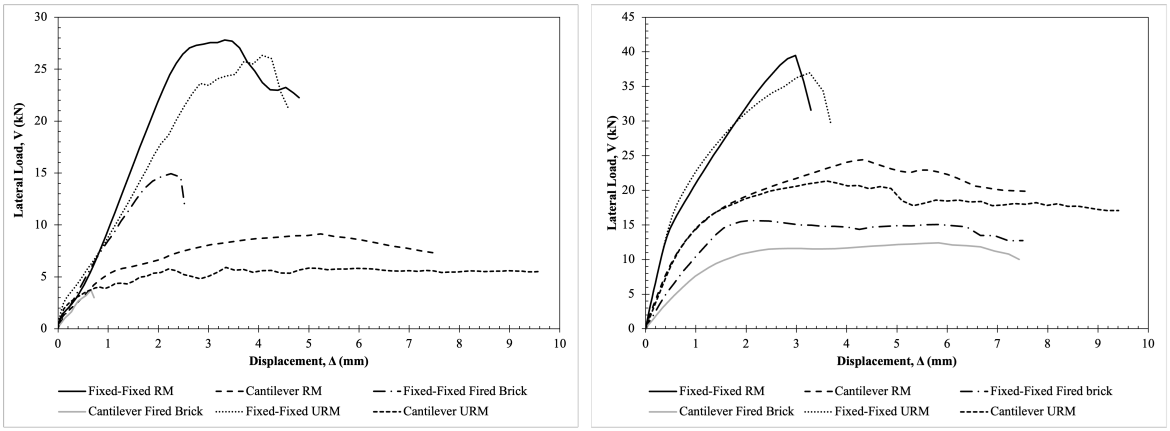

(a) Pushover curves for all squat piers under **low** pre-compression.

(b) Pushover curves for all squat piers under **high** pre-compression.

Figure 5.1: Comparison of pushover curves for squat piers under low and high pre-compression.

5.1.1 Lateral load capacity (V_p)

As shown in Figures 5.1a and 5.1b, the squat CSEB RM walls exhibited the highest lateral load capacities in all studied configurations. In the fixed-fixed configuration, the peak load increased from 27.81 kN at low pre-compression (Figure 5.1a) to 39.47 kN at high pre-compression (Figure 5.1b). The corresponding URM values were 26.33 kN

and 36.94 kN. The fired brick walls were weaker than the CSEB walls; in the fixed-fixed configuration, the peak load was 14.93 kN at low pre-compression and 15.62 kN at high pre-compression.

The pushover curves in Figures 5.1a and 5.1b also show that lateral load capacity increased with reinforcement, but that the increase associated with higher vertical pre-compression was even more pronounced. All wall types developed clearly higher peak capacities when the pre-compression level was increased, indicating that axial load had a major stabilising effect on the squat piers regardless of material system.

As can be seen most clearly in the cantilever cases in Figures 5.1a and 5.1b, the influence of reinforcement became more evident when the restraint was less favourable. At low pre-compression (Figure 5.1a), the RM wall reached 9.13 kN, compared with 5.83 kN for the URM wall and 3.73 kN for the fired brick wall. At high pre-compression (Figure 5.1b), the corresponding values were 24.85 kN for RM, 21.33 kN for URM, and 12.53 kN for fired brick. Reinforcement therefore had its clearest effect in the cantilever cases, while the fired brick walls remained significantly weaker than both CSEB alternatives. Since low pre-compression is likely to be more representative of practical one-storey masonry construction, the low-pre-compression cantilever cases shown in Figure 5.1a are particularly relevant when comparing the wall systems.

The failure modes help explain the capacity differences indicated by the pushover curves. For the RM CSEB walls, the fixed-fixed cases were mainly shear-dominated, with clear diagonal cracking through both the masonry and the grout, as shown in Figure 5.2. In cantilever, the low-pre-compression case showed stepped diagonal cracking mainly in the grout together with a localised deformation pattern, as shown in Figure 5.3. This suggests that the reinforced wall was able to maintain its integrity even as cracking developed. The high-pre-compression case developed a more severe mixed response with diagonal tensile cracking, extensive grout damage, and local toe crushing, but this may be viewed as a more strongly confined response rather than the most representative practical condition.

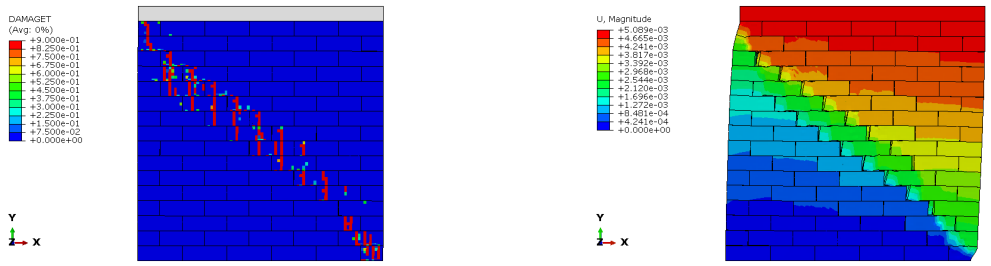

(a) Tensile damage in the squat RM CSEB pier under low pre compression.

(b) Deformed shape of the squat RM CSEB pier under low pre compression.

Figure 5.2: Failure development of the squat RM CSEB pier in the fixed fixed configuration under low pre compression.

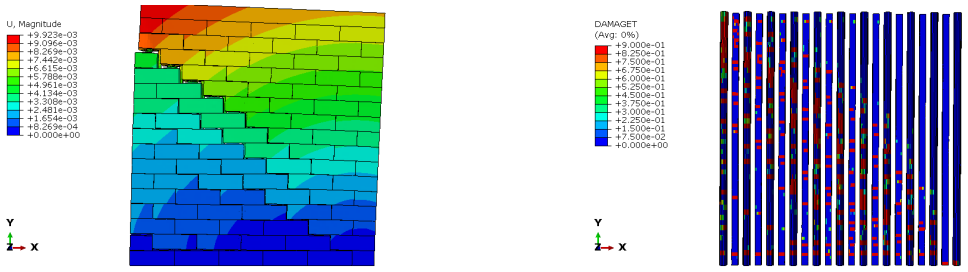

(a) Deformed shape of the squat RM CSEB pier in the cantilever configuration under low pre compression.

(b) Tensile damage in the mortar of the squat RM CSEB pier in the cantilever configuration under low pre compression.

Figure 5.3: Response of the squat RM CSEB pier in the cantilever configuration under low pre compression at V_{80}.

The URM CSEB walls showed less stable behaviour, especially in cantilever, where the response was governed more directly by grout cracking and in the low case by rocking. The fired brick walls were dominated by joint sliding and rocking rather than by a strong wall action, which is consistent with their lower lateral load capacities, as illustrated in Figure 5.5.

(a) Deformed shape of the squat URM CSEB pier in the cantilever configuration under low pre compression.

(b) Tensile damage in the squat URM CSEB pier in the cantilever configuration under low pre compression.

Figure 5.4: Response of the squat URM CSEB pier in the cantilever configuration under low pre compression at maximum load.

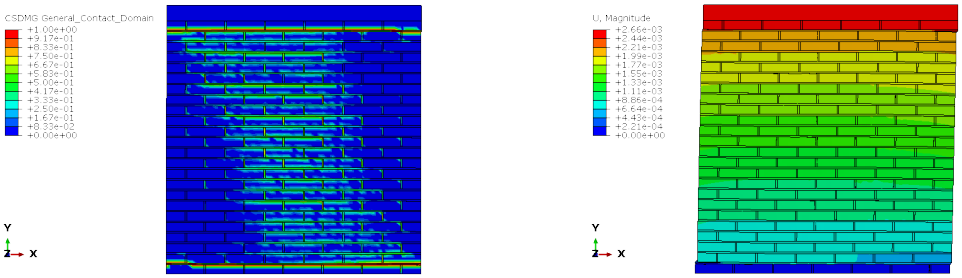

(a) Cohesive damage in the fired brick squat pier in the fixed fixed configuration under low pre compression.

(b) Deformed shape of the fired brick squat pier in the fixed fixed configuration under low pre compression.

Figure 5.5: Response of the fired brick squat pier in the fixed fixed configuration under low pre compression at V_{80}.

Additional ABAQUS output, including detailed damage distributions and failure pat-

terns, is provided in Appendix D.

5.1.2 Displacement ductility (μ)

The ductility results must be interpreted together with both the peak load and the failure mode. For the squat RM walls in fixed fixed, the ductility remained moderate, with $\mu = 2.22$ at low pre compression and $\mu = 2.30$ at high pre compression. The corresponding URM values were $\mu = 1.90$ and $\mu = 3.50$. This indicates that the fixed fixed walls were mainly shear controlled. Reinforcement improved the response, but did not lead to very large ductility values.

In cantilever, the URM walls gave much higher numerical ductility values, with $\mu = 15.05$ at low pre compression and $\mu = 9.53$ at high pre compression. The corresponding RM values were $\mu = 6.01$ and $\mu = 6.16$. However, these high URM values should not be interpreted as a better structural response. In the low cantilever case, the URM wall carried only 5.83 kN and was governed by rocking. The large ductility therefore reflects large displacements at low load rather than a stronger or more robust behaviour. The RM wall had a lower ductility index, but also a clearly higher capacity and a more stable failure process.

The fired brick walls had low ductility at low pre compression, with $\mu = 1.84$ in fixed fixed and $\mu = 1.50$ in cantilever. At high pre compression, the values increased to $\mu = 6.84$ and $\mu = 5.91$. This suggests that higher vertical load delayed degradation and produced a longer post peak response. Even so, the fired brick walls remained weaker than the CSEB walls, so the higher ductility was reached at substantially lower load levels.

An additional point is that not all curves showed a clear drop to 80% of the peak load. This is particularly important for the cantilever cases, where rocking or gradual degradation often dominated the response. In such cases, the response extended over a large displacement range without a sharp post peak drop. The ductility values are therefore influenced not only by the material response, but also by the shape of the post peak curve and by whether a clear failure point can be identified. This is especially relevant for the URM cantilever walls and for the fired brick walls with gradual strength loss.

5.1.3 Energy absorption (E_{abs})

The energy absorption results confirm that the response cannot be judged from peak load and ductility alone. For the RM walls, the absorbed energy was 92.5 J and 96.9 J in fixed fixed at low and high pre compression, respectively. In cantilever, the values were 54.8 J and 147.8 J. The large increase in the cantilever high case shows that the RM wall was able to sustain meaningful load over a relatively large displacement range, even after major cracking had developed.

The URM CSEB walls also showed high absorbed energy in some cases. The values were 78.78 J and 99.24 J in fixed fixed, 50.11 J in cantilever low, and 165.91 J in

cantilever high. The highest value was therefore obtained for the URM cantilever high wall, even though the RM wall had the higher peak load. This indicates that the URM curve extended over a broader displacement range. The larger energy value therefore reflects the shape of the curve rather than a stronger wall. This agrees with the observed failure mode, where the response was governed more by progressive cracking and extended deformation in the grout than by a stable load carrying mechanism.

For fired brick, the absorbed energy was much lower at low pre compression, with 23.9 J in fixed-fixed and only 1.54 J in cantilever. At high pre compression, the values increased strongly to 99.96 J and 77.35 J. This again shows the stabilising effect of vertical load. Still, the fired brick walls did not reach the same combination of strength and integrity as the CSEB walls.

Overall, the energy results highlight the importance of the post peak curve shape. A high absorbed energy can result either from a strong and stable response, as in the RM cantilever high case, or from a weaker but very extended deformation process, as in the URM cantilever high case. The observed failure modes are therefore essential when interpreting the energy values. Without them, the numerical results alone may give a misleading picture.

5.2 Slender piers

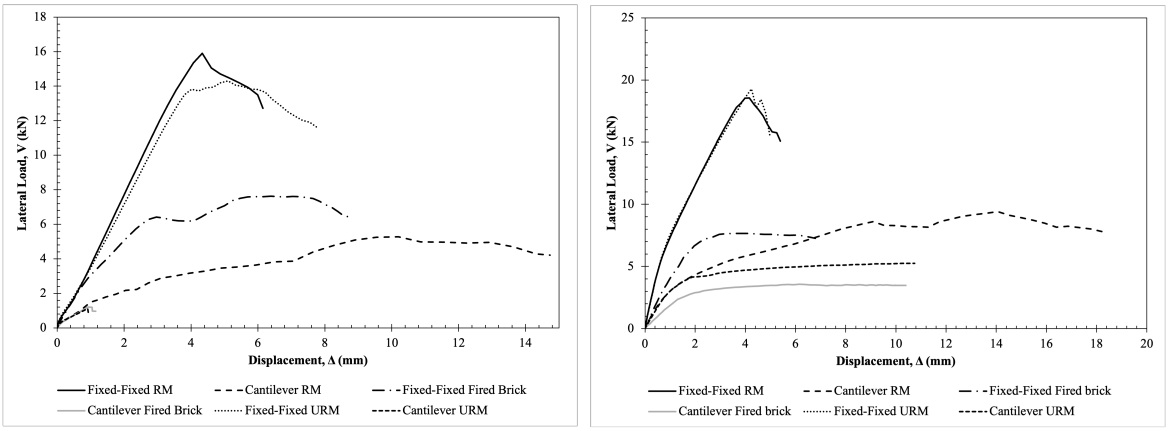

(a) Pushover curves for all slender piers under **low** pre-compression.

(b) Pushover curves for all slender piers under **high** pre-compression.

Figure 5.6: Comparison of pushover curves for slender piers under low and high pre-compression.

5.2.1 Lateral load capacity (V_p)

As shown in Figures 5.6a and 5.6b, the slender CSEB RM walls again exhibited the highest or near-highest lateral load capacities in most configurations. In the fixed-fixed configuration, the peak load was 15.90 kN at low pre-compression (Figure 5.6a) and 18.86 kN at high pre-compression (Figure 5.6b). The corresponding URM values were 14.52 kN and 19.29 kN. The fired brick walls were clearly weaker than the CSEB walls;

in the fixed-fixed configuration, the peak load was 7.76 kN at low pre-compression and 7.66 kN at high pre-compression.

The pushover curves in Figures 5.6a and 5.6b also show that the increase in lateral load capacity with reinforcement was less uniform than for the squat walls. For the CSEB walls in the fixed-fixed configuration, the increase from low to high pre-compression was relatively modest, and for RM the peak load was slightly lower than that of the corresponding URM wall at high pre-compression. This suggests that, for the slender piers, the response was influenced not only by axial load, but also more strongly by bending, crack localisation, and the interaction between grout, masonry, and reinforcement.

As can be seen most clearly in the cantilever cases in Figures 5.6a and 5.6b, the influence of reinforcement became much more pronounced when the restraint was less favourable. At low pre-compression (Figure 5.6a), the RM wall reached 5.27 kN, compared with 1.12 kN for the URM wall and 1.20 kN for the fired brick wall. At high pre-compression (Figure 5.6b), the corresponding values were 9.76 kN for RM, 5.26 kN for URM, and 3.61 kN for fired brick. Reinforcement therefore had its clearest effect in the cantilever cases, while the fired brick walls remained significantly weaker than the CSEB walls in all slender cases.

The failure modes help explain the capacity differences indicated by the pushover curves. For the RM CSEB walls, the fixed-fixed cases showed diagonal cracking together with damage in both block and grout, while the high-pre-compression case also developed a more mixed response with a flatter diagonal crack, vertical splitting tendencies, and local toe crushing, as illustrated in Figure 5.7. In cantilever, the low-pre-compression case showed extensive tensile damage in the grout and stepped diagonal cracking, while the high-pre-compression case developed diagonal cracking together with strong grout damage below the crack and local toe crushing, as shown in Figure 5.8.

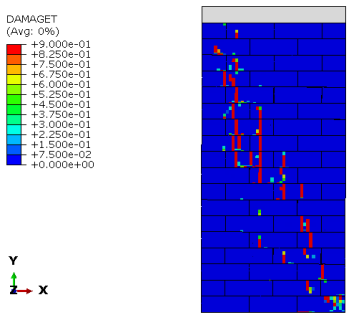

(a) Tensile damage in the slender RM CSEB pier in the fixed-fixed configuration under low pre-compression.

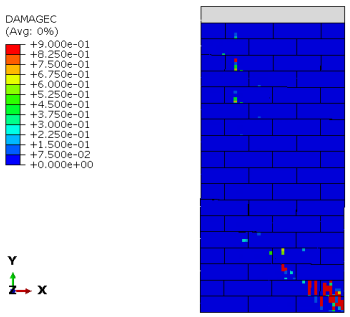

(b) Compressive damage in the slender RM CSEB pier in the fixed-fixed configuration under high pre-compression.

Figure 5.7: Representative damage patterns of the slender RM CSEB pier in the fixed-fixed configuration under low and high pre-compression.

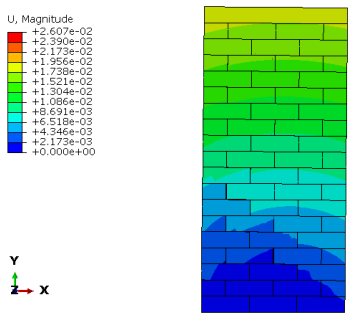

(a) Deformed shape of the slender RM CSEB pier in the cantilever configuration under high pre-compression.

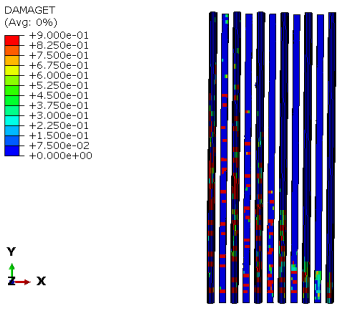

(b) Tensile damage in the grout of the slender RM CSEB pier in the cantilever configuration under high pre-compression.

Figure 5.8: Response of the slender RM CSEB pier in the cantilever configuration under high pre-compression at V_{80}.

The URM CSEB walls showed less stable behaviour, especially in cantilever, where the response was governed more directly by grout damage and local sliding- or rocking-like behaviour. In fixed-fixed, the low-pre-compression case appears to have involved both diagonal cracking and splitting, while the high-pre-compression case developed a more mixed pattern with distributed diagonal damage and local toe crushing. A representative low-pre-compression cantilever response is shown in Figure 5.9.

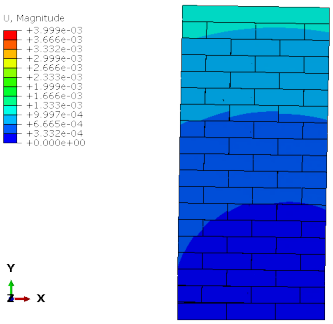

(a) Deformed shape of the slender URM CSEB pier in the cantilever configuration under low pre-compression.

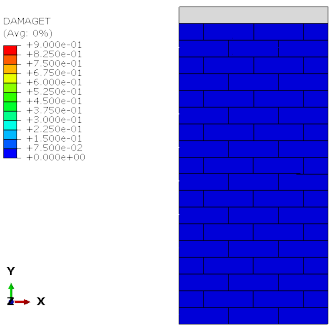

(b) Tensile damage in the slender URM CSEB pier in the cantilever configuration under low pre-compression.

Figure 5.9: Response of the slender URM CSEB pier in the cantilever configuration under low pre-compression at V_{80}.

The fired brick walls were again governed more strongly by joint-related mechanisms. In cantilever, the low- and high-pre-compression cases were mainly rocking-dominated, while the fixed-fixed cases showed more limited distributed damage and cohesion loss along the mortar joints rather than strong wall action, as illustrated in Figure 5.10.

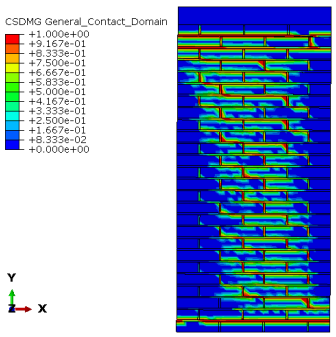

(a) Cohesive damage in the fired brick slender pier in the fixed-fixed configuration under low pre-compression.

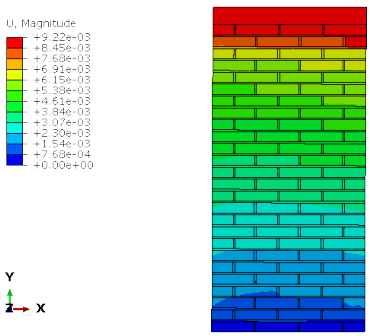

(b) Deformed shape of the fired brick slender pier in the fixed-fixed configuration under low pre-compression.

Figure 5.10: Response of the fired brick slender pier in the fixed-fixed configuration under low pre-compression at V_{80}.

Additional ABAQUS output, including detailed damage distributions and failure patterns, is provided in Appendix D.

5.2.2 Displacement ductility (μ)

The ductility values for the slender walls must also be interpreted together with the peak load and the shape of the post peak curve. For the fixed fixed CSEB walls, the RM ductility remained modest, with $\mu = 1.86$ at low pre compression and $\mu = 2.27$ at high pre compression. The corresponding URM values were $\mu = 2.38$ and $\mu = 2.08$. This suggests that in fixed fixed the response was governed by cracking and progressive localisation rather than by a long stable post peak regime. Reinforcement did not produce a large numerical increase in ductility, but it contributed to a more controlled and coherent response.

In cantilever, the picture was different. At low pre compression, the RM wall reached $\mu = 3.32$, compared with $\mu = 1.73$ for URM. At high pre compression, RM reached $\mu = 3.70$, while URM reached $\mu = 6.61$. The high URM ductility in the cantilever high case should however be interpreted with care, since the corresponding peak load was only 5.26 kN. The extended curve therefore reflects a long deformation process at low load rather than a stronger response. The RM wall had a lower ductility value, but combined this with a much higher peak load and much larger absorbed energy. This indicates a more useful deformation capacity at meaningful resistance levels.

The fired brick walls followed a similar pattern. At low pre compression, the ductility was $\mu = 3.74$ in fixed fixed and $\mu = 1.75$ in cantilever. At high pre compression, the values increased to $\mu = 3.89$ and $\mu = 5.65$. Especially in cantilever high, the high ductility is linked to rocking dominated behaviour rather than to a strong wall action. The fired brick walls therefore achieved relatively large deformation capacity in some cases, but at much lower load levels than the CSEB walls.

As for the squat walls, not all slender curves showed a distinct drop to 80% of the peak load. This is particularly relevant for the cantilever cases, where gradual degradation,

rocking, or sliding type behaviour could extend the response over a large displacement range without a sharp post peak drop. The ductility values are therefore sensitive to both the failure mechanism and the shape of the load displacement curve. This is especially important for the URM cantilever cases and for the fired brick walls, where the numerical ductility may appear high even though the resistance level remained low.

5.2.3 Energy absorption (E_{abs})

The energy absorption results further highlight the difference between a high peak load and a long but weak deformation process. For the RM walls, the absorbed energy was 62.0 J and 68.3 J in fixed fixed at low and high pre compression, respectively. In cantilever, the values were 55.9 J and 131.0 J. The high value in the cantilever high case shows that the reinforced wall was able to carry load over a long displacement range while still maintaining structural integrity.

For the URM CSEB walls, the energy values were 78.95 J and 62.22 J in fixed fixed, 0.612 J in cantilever low, and 48.37 J in cantilever high. The very low value in the low cantilever case is consistent with the very low peak load and with a weak grout controlled response. In fixed fixed low, the URM wall actually absorbed more energy than the corresponding RM wall, even though the RM wall had the higher peak load. This indicates that the URM curve extended over a somewhat broader displacement range. However, the difference was small in terms of strength, and the RM wall still showed a more robust structural response.

The fired brick walls gave lower or intermediate energy values. In fixed fixed, the values were 52.3 J at low pre compression and 43.52 J at high pre compression. In cantilever, the values were 0.87 J at low pre compression and 32.19 J at high pre compression. These results reflect the same trend seen in the load capacity and ductility results. The fired brick walls were more strongly influenced by rocking or joint release, especially in cantilever, and did not sustain the same load levels as the CSEB walls.

Overall, the energy results show that reinforcement was most beneficial in the slender cantilever walls. In fixed fixed, the difference between RM and URM was relatively small, especially at high pre compression. In cantilever, however, RM clearly improved the overall response by combining higher peak load with much greater absorbed energy. As for the squat walls, the post peak curve shape is essential for interpreting these values. A large absorbed energy can reflect either a stable and strong response or a long but weak deformation process, and the observed failure modes are therefore necessary for a correct interpretation.

6 Discussion

This chapter discusses the numerical results in relation to wall geometry, material system, reinforcement, boundary conditions, and pre-compression level. The aim is not only to compare the peak values obtained from the pushover analyses, but also to interpret how the different walls behaved, how damage developed, and what the observed failure modes imply for the overall structural response. Particular attention is given to the differences between reinforced and unreinforced CSEB walls, and to how these compare with fired brick walls.

The discussion is organised in three parts. First, the squat and slender walls are compared in order to identify the effect of wall geometry. Second, the pier level results are interpreted in a broader structural context in order to discuss what they may imply at building level. Finally, the main modelling uncertainties and limitations are discussed.

6.1 Comparison between squat and slender walls

A clear difference was observed between the squat and slender walls. In general, the squat walls reached higher lateral load capacities than the slender walls, especially for the CSEB specimens. This was most evident for the reinforced CSEB walls. In the squat fixed fixed configuration, the RM walls reached 27.81 kN and 39.47 kN at low and high pre compression, respectively, whereas the corresponding slender RM walls reached 15.90 kN and 18.86 kN. A similar trend was seen in cantilever, where the squat RM walls reached 9.13 kN and 24.85 kN, while the slender RM walls reached 5.27 kN and 9.76 kN. The squat geometry therefore gave a clear capacity advantage.

At the same time, the comparison between RM and URM was not entirely uniform. In most cases, reinforcement increased the lateral load capacity, especially in cantilever. However, there were also cases where URM matched or slightly exceeded RM. This was most visible for the slender fixed fixed walls at high pre compression, where URM reached 19.29 kN and RM 18.86 kN. A similar tendency can also be seen if energy absorption is considered, for example in the squat cantilever high case where URM exceeded RM despite the lower peak load. These results show that reinforcement did not always lead to a direct increase in every numerical performance indicator. Instead, the benefit of reinforcement depended on wall geometry, restraint condition, and the governing failure mechanism.

The failure modes help explain these differences. The squat walls were more often governed by diagonal cracking, shear dominated damage, and in some cases local toe crushing. In the reinforced squat walls, the grout zone and the reinforcement were actively engaged, and the wall generally remained coherent even after major cracking had developed. The slender walls showed a more mixed response. Their behaviour

more often combined diagonal cracking with bending effects, local sliding, splitting, or partial rotation over a crack band. In several slender cases, the damage became more distributed and the post peak response longer and less sharply defined. This helps explain why a slender URM wall could in some cases reach values close to, or even slightly above, those of the corresponding RM wall, despite the absence of reinforcement. The longer and more distributed post peak response may in some cases have compensated partly for the lower structural integrity.

The ductility and energy results reflect this complexity. In the squat walls, lower ductility values were often associated with a stronger and more stable response. In the slender walls, higher ductility could in some cases be achieved through weaker mechanisms with lower resistance. This was particularly clear in the URM cantilever cases, where large displacements could develop without a correspondingly high load level. The same applies to energy absorption. A high absorbed energy did not always indicate a better wall, but could instead reflect a long and relatively weak post peak response.

For the CSEB walls, the energy absorption was often high in the slender cases, especially in cantilever. For example, the slender RM cantilever high wall reached 131.0 J, compared with 147.8 J for the squat case, while the slender URM cantilever high wall reached 48.37 J. More importantly, several of the slender walls showed a more extended deformation process, which in some cases gave energy values that were comparable to, or higher than, those of the squat walls even when the peak load was lower. This confirms that the energy values were strongly influenced by the shape of the pushover curve and not only by the peak capacity.

For fired brick, the trend was somewhat different. The slender fired brick walls were generally weaker and more sensitive to rocking and joint release, but the energy absorption did not always increase with slenderness. A clear example is the fixed fixed high case, where the squat fired brick wall reached 99.96 J, while the corresponding slender wall reached only 43.52 J. This indicates that the squat fired brick wall was able to sustain load over a longer and more meaningful post peak range, whereas the slender wall lost capacity more quickly despite its more deformable geometry. The comparison therefore shows that increased slenderness did not automatically produce a better energy response, especially not for the fired brick walls.

6.1.1 From pier level to building level

Although the present results were obtained at pier level, they still give some indication of how the wall systems may perform in a real one storey house. At building level, the critical issue is not only which wall reaches the highest peak load, but which wall can provide sufficient strength while still maintaining a stable and coherent response as damage develops.

In that respect, the reinforced CSEB walls appear to be the most favourable option overall. This is supported mainly by their generally higher lateral load capacities and by the observed failure modes, where the walls remained more coherent after cracking than the corresponding unreinforced and fired brick walls. The energy absorption

results are more mixed and do not always favour the reinforced walls. In several cases, the unreinforced CSEB walls reached similar or even higher energy values, but this often appears to reflect a longer and weaker post peak response rather than a more robust structural behaviour.

The results also highlight an important trade off. In seismic design, more slender walls are often considered favourable because they are more likely to develop flexural or rocking dominated behaviour rather than brittle shear failure. Under cyclic loading, such mechanisms can be beneficial because they allow larger deformation and may provide clearer warning before collapse. However, this should not be interpreted as damage free behaviour. In the present wall systems, rocking and deformation dominated response were generally associated with opening of joints, cohesion loss, sliding, grout damage, and local interface degradation. Such walls may therefore remain standing after strong shaking, but still suffer significant residual damage, reduced stiffness, and reduced capacity in a subsequent loading cycle.

By contrast, the squat walls often developed more severe diagonal cracking, grout damage, and in some cases local toe crushing. This type of response is more directly associated with irreversible structural damage and may be less desirable if it becomes too abrupt or brittle. At the same time, the squat walls generally reached much higher lateral load levels than the slender walls. Greater deformability therefore did not automatically imply a better overall structural response in the present study. The slender walls often achieved their larger deformation capacity at substantially lower resistance levels.

For the wall systems studied here, the squat reinforced CSEB walls appear to offer the most favourable overall balance between strength and damage tolerance. Even if the squat walls were more shear dominated, they still developed a stronger and generally more robust response than the slender walls in most cases. The practical implication is therefore that reinforced CSEB walls appear more promising than fired brick walls for one storey construction in earthquake prone areas, while the choice between squat and slender geometry should be understood as a balance between higher strength and more deformation tolerant failure mechanisms.

Overall, the results indicate that squat walls were generally more favourable than slender walls, particularly in terms of lateral load capacity and overall robustness. However, the comparison also shows that the response cannot be judged from peak load alone. In some cases, URM walls approached or exceeded RM walls in individual parameters, especially when the response became more distributed and the post peak curve longer. The same applies to energy absorption, where a higher value may reflect either a robust load carrying mechanism or a long but weaker deformation process. The numerical results must therefore always be interpreted together with the failure mode and the shape of the pushover curve.

6.2 Sources of uncertainty and modelling limitations

The numerical models developed in this study provide useful insight into the behaviour of the different masonry systems, but the results should still be interpreted with caution. As in all nonlinear micromodelling studies, the global response depends strongly on the modelling assumptions, and several of these introduce uncertainty in the predicted capacity, damage development, and failure mode.

One important source of uncertainty is the interface modelling used for the fired clay brick masonry. In the present study, the brick mortar interface was represented by frictional contact combined with cohesive behaviour. This required the definition of stiffness and strength parameters in the normal direction and in two shear directions. Although the selected values were based on available literature and reasonable assumptions, the actual interface properties are difficult to define with confidence. If the cohesive shear strength was chosen too low, the model may have allowed sliding or debonding too early. This would reduce the predicted load carrying capacity of the fired brick walls and may partly explain why the fired brick models showed relatively low resistance. Since masonry behaviour is strongly influenced by the bond between units and mortar, the interface parameters have a direct effect on the global response.

A related simplification concerns the interaction between the CSEB units and the grout. In the numerical models, this interface was modelled using friction only, without any cohesive bond. In reality, some mechanical bond would be expected once the grout has hardened. By neglecting this bond effect, the interaction between the block and the grout may have been weaker in the simulations than in an actual wall. This could make the reinforced CSEB models somewhat conservative, especially in cases where the response depends strongly on the integrity of the grout zone and the transfer of forces between the grout, the blocks, and the reinforcement.

Another uncertainty is connected to the assumed material properties. The constitutive models required tensile behaviour and compressive damage parameters for the CSEB units, the grout, and the mortar. However, no direct tensile testing was available for these materials. The tensile properties therefore had to be estimated using theoretical assumptions and values from previous studies. This is significant because masonry materials are generally weak in tension, and the numerical response is highly sensitive to the onset and development of cracking. The assumed tensile parameters likely influenced both the predicted failure mode and the post peak behaviour.

The reinforcement modelling also includes simplifications. In the present study, the reinforcement mainly contributed through axial action, while no separate shear resistance was assigned to the bars. In reality, reinforcement can also influence the shear response of a wall, either directly or indirectly through its interaction with the surrounding grout and masonry. The omission of this contribution may therefore have affected the predicted behaviour of the reinforced CSEB walls, particularly in cases where combined flexural and shear mechanisms developed.

Mesh size is another factor that may influence the results. In nonlinear analyses, the mesh affects stiffness, stress concentration, crack localisation, and the apparent distribution of damage. Although care was taken to choose a reasonable mesh size, some

sensitivity to mesh density should still be expected. A dedicated mesh sensitivity study would therefore strengthen confidence in the numerical results and help determine whether the observed crack patterns and failure modes are stable with respect to discretisation.

In addition, all materials were treated as homogeneous and isotropic. This is a necessary simplification, but it does not fully reflect the variability that exists in real masonry materials. CSEB units, fired clay bricks, mortar, and grout may all vary in strength and stiffness due to differences in production, curing, workmanship, and material composition. Since such variability was not included in the models, the simulations represent an idealised material response rather than the full range of behaviour that may occur in practice.

The boundary conditions represent another important limitation. The study considered two idealised cases, namely cantilever and fixed fixed. These two configurations were chosen in order to capture two limiting structural responses and to investigate the influence of restraint on wall behaviour. In real buildings, however, the restraint conditions are usually somewhere between these extremes. Connections to slabs, adjacent walls, and surrounding structural elements often provide partial restraint rather than perfectly fixed or completely free conditions. The numerical results should therefore be interpreted as representing a range between two limiting cases, rather than exact predictions of real boundary conditions.

7 Conclusion

This study used detailed numerical micromodelling to investigate the lateral response of squat and slender masonry piers made of reinforced CSEB, unreinforced CSEB, and fired brick under different boundary conditions and pre compression levels. The results show that CSEB walls gave a more favourable overall structural response than fired brick walls. This applied not only to the reinforced CSEB walls, but also to the unreinforced CSEB walls, which in most cases still performed better than fired brick walls. Among all wall systems considered, the reinforced CSEB walls gave the best overall performance.

Wall geometry also had a clear influence on the response. In general, the squat walls performed better than the slender walls, with higher peak loads and a more stable overall behaviour. The slender walls were more sensitive to bending, localised cracking, and deformation concentration, especially under cantilever boundary conditions. At the same time, the results showed that greater deformability did not automatically imply better structural performance, since the more slender walls often reached these deformation levels at lower load levels.

Reinforcement improved the performance of the CSEB walls, particularly in the cantilever cases, where it increased the lateral resistance and helped the walls remain more coherent after major cracking had developed. Fired brick walls showed the least favourable behaviour overall and were more strongly governed by joint sliding, rocking, and cohesion loss in the mortar joints.

The main conclusion is therefore that reinforced CSEB walls appear to be the most suitable option among the wall systems studied. For applications such as those relevant to Build up Nepal, this is an important result, since it indicates that reinforced CSEB construction can provide a more favourable combination of structural capacity, damage tolerance, and post peak robustness than traditional fired brick masonry. Within the scope of the present study, reinforced CSEB walls are therefore recommended as a promising alternative for one storey construction in earthquake prone areas.

7.1 Future work and potential applications

The modelling framework developed in this study provides a useful basis for further research. The detailed micromodelling approach makes it possible to observe how damage initiates and develops in different materials and interfaces, which gives valuable insight into the mechanisms governing the global wall response.

One important continuation of the present work would be improved calibration of the material and interface models. Experimental tensile testing of the grout, mortar, and CSEB units would allow a more reliable definition of the tensile parameters used in

the nonlinear analyses. In the same way, experimental calibration of the fired brick mortar interface and of the grout block interaction would improve the reliability of the interface modelling and reduce some of the present uncertainty.

The results of this study may also be useful for macro scale modelling of CSEB buildings. In macro models, masonry walls are often represented by equivalent piers and spandrels rather than by detailed material level models. The response observed in this study, including lateral load capacity, displacement limits, and failure modes for squat and slender piers, could therefore be used to define representative properties for such macro elements. This would make it possible to use the present findings in simplified structural models of CSEB houses, where the global seismic response of the building is evaluated on the basis of the performance of individual wall segments. Such models could also make it possible to study how squat and slender wall segments interact within the same building, and which parts of the wall system are most likely to govern the onset of severe damage.

In this study, only one reinforcement configuration was investigated. According to the Nepal National Building Code, vertical reinforcement in CSEB walls should be placed at a spacing of approximately 1.2-1.5 m, while this study only considered the upper limit of 1.5 m. A smaller spacing, such as 1.2 m, would increase the amount of vertical reinforcement in the wall and could potentially improve both strength and deformation capacity by providing additional resistance against cracking. In addition, the code requires horizontal reinforcement in sill and lintel bands, which were not included in the analysed models. These elements contain horizontal reinforcement that ties the walls together and helps distribute loads within the structure. In a macro-scale modelling approach, these bands could instead be represented as separate structural elements with horizontal reinforcement included, making it possible to evaluate how they influence the overall structural behaviour and seismic performance of the building. An additional aspect that could be considered is the inclusion of horizontal reinforcement directly in the bed joints between the CSEB blocks. In reinforced masonry, horizontal reinforcement contributes to shear resistance by bridging cracks and transferring tensile forces across potential failure planes. This can improve crack control and reduce the risk of brittle shear failure, particularly in walls where shear mechanisms are dominant. Such reinforcement may also enhance deformation capacity and energy absorption by promoting a more stable post-peak response. Including this type of reinforcement in future models could therefore influence both the failure mode and the overall structural performance of the wall system. In this study, the reinforcement diameter was also kept constant at 12 mm, although the standard allows diameters between 10 and 12 mm. It would therefore be interesting to investigate how the results might change if a smaller diameter, such as 10 mm, were used.

The results also make it possible to identify which material or interface tends to govern the response in different wall types and loading conditions. This is useful for future design development, since it highlights where strengthening measures may be most effective. If failure repeatedly initiates in a certain material or interface, future studies can focus on improving that part of the system through modified detailing, alternative material properties, or improved interface performance.

Further studies should also investigate a wider range of structural configurations. In

the present work, only squat and slender walls under two idealised boundary conditions were considered. There is therefore clear scope to study intermediate cases with partial restraint, since these may better represent real masonry buildings. Validation against experimental tests would also be an important next step, both to improve confidence in the material models and to assess how well the numerical failure modes correspond to observed behaviour in practice.

Another relevant continuation would be to study alternative reinforcement strategies. This could include different bar diameters, reinforcement ratios, layouts, anchorage conditions, or reinforcement materials. Such studies would help clarify whether the favourable response observed for the reinforced CSEB walls can be further improved through modified reinforcement detailing.

Overall, the present work should be seen as a first step toward a more robust numerical framework for masonry modelling. With improved calibration, validation, and sensitivity analysis, the modelling approach developed here could be extended into a more reliable tool for both research and practical structural assessment.

Bibliography

Abrams, D. P. and N. Shah (1992). *Cyclic Load Testing of Unreinforced Masonry Walls*. Tech. rep. 92-26-10. Urbana, IL: University of Illinois at Urbana-Champaign, Advanced Construction Technology Center.

Agüera, N. D., M. E. Tornello and C. D. Frau (2016). "Structural Response of Unreinforced Masonry Walls". In: *Journal of Civil Engineering and Architecture* 10, pp. 219–231. DOI: 10.17265/1934-7359/2016.02.011.

Akhaveissy, A. H. and G. Milani (2012). "Pushover analysis of large scale unreinforced masonry structures by means of a fully 2D non-linear model". In: *Construction and Building Materials* 41, pp. 276–295. DOI: 10.1016/j.conbuildmat.2012.11.090.

Armouti, S. N. (2015). *Earthquake Engineering: Theory and Implementation with the 2015 International Building Code*. New York, NY: McGraw-Hill Education.

Augenti, N. and F. Parisi (2006). "Testing of Partially Grouted Masonry Walls Subjected to Reversed Cyclic Loading". In: *Proceedings of the 8th U.S. National Conference on Earthquake Engineering*. San Francisco, CA.

Azevedo, A. and M. Hagen (2025). *Solar and Seasonal Influences on Volcanoes and Earthquakes: The Rule of X Flares*. Open Journal of Earthquake Research. CC BY 4.0.

Barenblatt, G. I. (1962). "The mathematical theory of equilibrium cracks in brittle fracture". In: *Advances in Applied Mechanics* 7, pp. 55–129. DOI: 10.1016/S0065-2156(08)70121-2.

Benzeggagh, M. L. and M. Kenane (1996). "Measurement of mixed-mode delamination fracture toughness of unidirectional glass/epoxy composites with mixed-mode bending apparatus". In: *Composites Science and Technology* 56.4, pp. 439–449. DOI: 10.1016/0266-3538(96)00005-X.

Borst, R. de and P. A. Vermeer (1984). "Non-Associated Plasticity for Soils, Concrete and Rock". In: *HERON* 29.3, pp. 1–64.

Bothara, J. M. and S. Brzev (2011). *A Tutorial: Improving the Seismic Performance of Stone Masonry Buildings*. Oakland, CA: Earthquake Engineering Research Institute (EERI).

Brick – First Amendment (NS 1:2035): Specification for Burnt Clay Bricks (1978). Nepal.

Bryce, E. (12th Oct. 2023). *How many tectonic plates does Earth have?* URL: https://www.livescience.com/planet-earth/geology/how-many-tectonic-plates-does-earth-have (visited on 15/03/2026).

Bui, T.-T., A. Limam, W.-S.-A. Nana, E. Ferrier, M. Bost and Q.-B. Bui (2020). "Evaluation of One-Way Shear Behaviour of Reinforced Concrete Slabs: Experimental and Numerical Analysis". In: *European Journal of Environmental and Civil Engineering* 24.2, pp. 190–216. DOI: 10.1080/19648189.2017.1371646.

Build Up Nepal (BUN) (n.d.). *About us*. Build Up Nepal. URL: https://www.buildupnepal.com/about-us/ (visited on 31/01/2026).

Build Up Nepal (BUN) (2026). *Interlocking Eco-Bricks*. URL: https://www.buildupnepal.com/interlocking-bricks/ (visited on 31/01/2026).

Celano, T., L. Argiento, F. Ceroni and C. Casapulla (2021). "Literature Review of the In-Plane Behavior of Masonry Walls: Theoretical vs. Experimental Results". In: *Materials* 14, p. 3063.

Center for Research & Development (CERAD) (2025). *Impact Report 2024–2025*. Babarmahal, Kathmandu: Center for Research & Development.

Dassault Systèmes (SIMULIA) (2024a). *Damage Evolution and Element Removal for Ductile Metals*. Defines characteristic length and displacement-/energy-based damage evolution for ductile metals. URL: https://docs.software.vt.edu/abaqusv2024/English/SIMACAEMATRefMap/simamat-c-damageevolductile.htm (visited on 28/02/2026).

Dassault Systèmes (SIMULIA) (2024b). *Defining plasticity in Abaqus*. Abaqus 2024 documentation mirror (Virginia Tech). URL: https://docs.software.vt.edu/abaqusv2024/English/SIMACAEGSARefMap/simagsa-c-matdefining.htm (visited on 28/02/2026).

Dassault Systèmes (SIMULIA) (2024c). *Ductile damage*. Lists required input columns (fracture strain, stress triaxiality, strain rate) and defines stress triaxiality. URL: https://docs.software.vt.edu/abaqusv2024/English/SIMACAECAERefMap/simacae-t-prpmechanicaldamageductile.htm (visited on 28/02/2026).

Dassault Systèmes SIMULIA (2024d). **CONCRETE DAMAGED PLASTICITY*. Keyword reference page listing the five CDP plasticity parameters. URL: https://abaqus.uclouvain.be/English/SIMACAEKEYRefMap/simakey-r-concretedamagedplasticity.htm (visited on 28/02/2026).

Dassault Systèmes SIMULIA (2024e). *Abaqus 2024 Documentation: Abaqus/Standard element index (C3D8R definition)*. Lists C3D8R as an 8-node linear brick element with reduced integration. URL: https://docs.software.vt.edu/abaqusv2024/English/SIMACAEELMRefMap/simaelm-c-stdelementindex.htm (visited on 28/02/2026).

Dassault Systèmes SIMULIA (2024f). *Abaqus 2024 Documentation: About general contact in Abaqus/Explicit*. URL: https://docs.software.vt.edu/abaqusv2024/English/SIMACAEITNRefMap/simaitn-c-contactgeneral.htm (visited on 28/02/2026).

Dassault Systèmes SIMULIA (2024g). *Abaqus 2024 Documentation: Comparison of implicit and explicit time integration procedures*. URL: https://docs.software.vt.edu/abaqusv2024/English/SIMACAEGSARefMap/simagsa-c-absgencomp.htm (visited on 28/02/2026).

Dassault Systèmes SIMULIA (2024h). *Abaqus 2024 Documentation: Contact cohesive behavior*. URL: https://docs.software.vt.edu/abaqusv2024/English/SIMACAEITNRefMap/simaitn-c-cohesivebehavior.htm (visited on 28/02/2026).

Dassault Systèmes SIMULIA (2024i). *Abaqus 2024 Documentation: Defining individual elements by specifying their nodes*. Describes element definition via nodes and element type. URL: https://docs.software.vt.edu/abaqusv2024/English/?show=SIMACAEMODRefMap/simamod-c-element.htm (visited on 28/02/2026).

Dassault Systèmes SIMULIA (2024j). *Abaqus 2024 Documentation: Embedded element technique (Embedded Region constraint)*. Describes host/embedded regions and the kinematic constraint (no slip) imposed by the embedded element technique. URL: https://docs.software.vt.edu/abaqusv2024/English/?show=SIMACAECSTRefMap/simacst-c-embeddedelement.htm (visited on 28/02/2026).

Dassault Systèmes SIMULIA (2024k). *Abaqus 2024 Documentation: Energy balance (Abaqus/Explicit)*. URL: https://docs.software.vt.edu/abaqusv2024/English/SIMACAEGSARefMap/simagsa-m-OvwEnergy-sb.htm (visited on 28/02/2026).

Dassault Systèmes SIMULIA (2024l). *Abaqus 2024 Documentation: Explicit dynamic analysis procedure*. URL: https://docs.software.vt.edu/abaqusv2024/English/SIMACAEANLRefMap/simaanl-c-expdynamic.htm (visited on 28/02/2026).

Dassault Systèmes SIMULIA (2024m). *Abaqus 2024 Documentation: Mechanical contact properties (hard contact)*. URL: https://docs.software.vt.edu/abaqusv2024/English/SIMACAEITNRefMap/simaitn-c-contactmechanical.htm (visited on 28/02/2026).

Dassault Systèmes SIMULIA (2024n). *Abaqus 2024 Documentation: Quasi-static analysis discussion in Abaqus/Explicit (energy check)*. URL: https://docs.software.vt.edu/abaqusv2024/English/?show=SIMACAEGSARefMap/simagsa-c-qsidiscussion.htm (visited on 28/02/2026).

Dassault Systèmes SIMULIA (2024o). *Abaqus 2024 Documentation: Truss element library (T3D2 definition)*. Lists T3D2 as a 2-node linear displacement truss element. URL: https://docs.software.vt.edu/abaqusv2024/English/SIMACAEELMRefMap/simaelm-r-trusslibrary.htm (visited on 28/02/2026).

Department of Urban Development and Building Construction (DUDBC) (2015a). *Nepal National Building Code NBC 202:2015: Guidelines on Load Bearing Masonry*. Nepal National Building Code (NBC). Babar Mahal, Kathmandu, Nepal: Government of Nepal, Ministry of Urban Development. URL: https://www.iibh.org/kijun/pdf/Nepal_21_NBC_202_Thumb_Load_Bearing_Masonry.pdf (visited on 06/02/2026).

Department of Urban Development and Building Construction (DUDBC) (2015b). *Nepal National Building Code NBC 203:2015: Guidelines for Earthquake Resistant Building Construction: Low Strength Masonry*. Nepal National Building Code (NBC). Babar Mahal, Kathmandu, Nepal: Government of Nepal, Ministry of Urban Development. URL: https://giwmscdntwo.gov.np/media/pdf_upload/NBC%20203-2015%20GUIDELINES%20FOR%20EARTHQUAKE%20RESISTANT%20BUILDING%20CONSTRUCTION%20LOW%20STRENGTH%20MASONRY_xudklma.pdf (visited on 06/02/2026).

Dolatshahi, K. M. and A. A. Aref (2011). "Plane and Out-of-Plane Deformation of Masonry Walls". In: *Proceedings of the Engineering Mechanics Institute Conference (EMI 2011)*. URL: https://sharif.edu/~dolatshahi/Papers/Conference/2011-EMI-3DcyclicURM.pdf (visited on 26/02/2026).

Doran, B., M. Karslioglu, Z. Unsal Aslan and C. Vatansever (2023). "Experimental and Numerical Investigation of Unreinforced Masonry Walls with and without Opening". In: *International Journal of Architectural Heritage* 17.11, pp. 1833–1854. DOI: 10.1080/15583058.2022.2080611.

Dugdale, D. S. (1960). "Yielding of steel sheets containing slits". In: *Journal of the Mechanics and Physics of Solids* 8.2, pp. 100–104. DOI: 10.1016/0022-5096(60)90013-2.

Eil, A., J. Li, P. Baral and E. Saikawa (2020). *Dirty Stacks, High Stakes: An Overview of the Brick Sector in South Asia*. Tech. rep. Report. The World Bank.

ElGawady, M. A., P. Lestuzzi and M. Badoux (2007). "Static Cyclic Response of Masonry Walls Retrofitted with Fiber-Reinforced Polymers". In: *Journal of Composites for Construction* 11.1, pp. 50–61. DOI: 10.1061/(ASCE)1090-0268(2007)11:1(50).

Encyclopaedia Britannica Editors (2025). *Seismic Wave*. URL: https://www.britannica.com/science/seismic-wave (visited on 31/01/2026).

Fajfar, P. (2000). "A Nonlinear Analysis Method for Performance-Based Seismic Design". In: *Earthquake Spectra* 16.3, pp. 573–592. DOI: 10.1193/1.1586128.

Fordham, M. (2021). *Carbon Evaluation of Compressed Stabilised Earth Blocks (CSEB) in Nepal*. Tech. rep. London: Max Fordham LLP.

Giri, O. P., L. R. Thapa and S. Shrestha (2024). "Assessment of Shear Strength of Brick Masonry in Mud Mortar of Kathmandu Valley: An In-situ Study". In: *International Journal of Engineering Trends and Technology* 72.12.

Government of Nepal, Ministry of Urban Development and Department of Urban Development and Building Construction (DUDBC) (2016). *Seismic Retrofitting Guidelines of Buildings in Nepal: Masonry Structures*. Guideline. Volume: Masonry Structures. Kathmandu, Nepal: Ministry of Urban Development, Government of Nepal.

Government of Nepal, National Planning Commission, The World Bank, Asian Development Bank, European Union and United Nations (2015). *Nepal Earthquake 2015: Post Disaster Needs Assessment – Executive Summary*. PDNA Executive Summary. Government of Nepal (NPC) and development partners. URL: https://www.worldbank.org/content/dam/Worldbank/document/SAR/nepal-pdna-executive-summary.pdf (visited on 06/02/2026).

Haddad, M. and K. Sepehrnoori (2016). "XFEM-Based CZM for the Simulation of 3D Multiple-Cluster Hydraulic Fracturing in Quasi-Brittle Shale Formations". In: *Rock Mechanics and Rock Engineering* 49.12, pp. 4731–4748. DOI: 10.1007/s00603-016-1057-2.

Hernoune, H., B. Benabed, A. Kanellopoulos, A. H. Al-Zuhairi and A. Guettala (2020). "Experimental and Numerical Study of Behaviour of Reinforced Masonry Walls with NSM CFRP Strips Subjected to Combined Loads". In: *Buildings*.

Huang, D., A. Albareda and O. Pons (2023). "Experimental and Numerical Study on Unreinforced Brick Masonry Walls Retrofitted with Sprayed Mortar under Uniaxial Compression". In: *Buildings* 13.1, p. 122. DOI: 10.3390/buildings13010122.

International Labour Organization (2020). *Report on Employment Relationship Survey in the Brick Industry in Nepal*. Tech. rep. Kathmandu, Nepal: International Labour Organization.

Koirala, M., R. P. Sapkota and S. P. Kayastha (2025). "Soil Quality Impacted by Brick Kilns in the Agriculture Fields of Kathmandu Valley". In: *Journal of Environment Sciences* XI, pp. 18–27.

Kuria, K. K. and O. K. Kegyes-Brassai (2023). *Pushover Analysis in Seismic Engineering: A Detailed Chronology and Review of Techniques for Structural Assessment*. ResearchGate preprint. URL: https://www.researchgate.net/publication/376796130_Pushover_Analysis_in_Seismic_Engineering_A_Detailed_Chronology_and_Review_of_Techniques_for_Structural_Assessment (visited on 15/03/2026).

Lee, J. and G. L. Fenves (1998). "Plastic-Damage Model for Cyclic Loading of Concrete Structures". In: *Journal of Engineering Mechanics* 124.8, pp. 892–900. ISSN: 0733-9399.

Liu, Z. and A. Crewe (2020). "Effects of size and position of openings on in-plane capacity of unreinforced masonry walls". In: *Bulletin of Earthquake Engineering* 18, pp. 4783–4812. DOI: 10.1007/s10518-020-00894-0.

Lourenço, P. B. (1996). "Computational Strategies for Masonry Structures". PhD dissertation. Delft, The Netherlands: Delft University of Technology.

Lourenço, P. B. (2002). "Computations of historical masonry constructions". In: *Progress in Structural Engineering and Materials* 4.3, pp. 301–319. DOI: 10.1002/pse.120.

Lourenço, P. B., J. G. Rots and J. Blaauwendraad (1995). "Two approaches for the analysis of masonry structures: micro and macro-modeling". In: *HERON* 40.4, pp. 313–340. ISSN: 0046-7316.

Lubliner, J., J. Oliver, S. Oller and E. Oñate (1989). "A Plastic-Damage Model for Concrete". In: *International Journal of Solids and Structures* 25.3, pp. 299–326.

Magenes, G. and G. M. Calvi (1997). "In-plane seismic response of brick masonry walls". In: *Earthquake Engineering & Structural Dynamics* 26.11, pp. 1091–1112. DOI: 10.1002/(SICI)1096-9845(199711)26:11<1091::AID-EQE693>3.0.CO;2-6.

Maïni, S. (2005). *Earthquake Resistant Buildings with Hollow Interlocking Blocks*. Auroville: Auroville Earth Institute.

Marthong, C. (2018). "Use of Polyethylene Terephthalate Fibers for Strengthening of Reinforced Concrete Frame Made of Low-Grade Aggregate". In: *Earthquakes - Forecast, Prognosis and Earthquake Resistant Construction*. Ed. by V. Svalova. IntechOpen. DOI: 10.5772/intechopen.76616.

Mehta, P. K. and P. J. M. Monteiro (2014). *Concrete: Microstructure, Properties, and Materials*. 4th ed. McGraw-Hill Education.

Mellegård, H. and A. Steinert (2016). "Compressed Stabilised Earth Blocks in Nepal: A Study of the Rehabilitation of Buildings in Rural Villages after the Gorkha Earthquake". MA thesis. Gothenburg: Chalmers University of Technology.

Mishra, S. R., H. R. Parajuli, D. Gautam, K. B. Shrestha and H. Chaulagain (2019). "Mechanical Properties of Components of Nepalese Historical Masonry Buildings". In: *International Journal of Advanced Structural Engineering*.

Mukai, Y., H. Hoshino, N. Yamamoto, M. Masui, A. Miyauchi and R. P. Suwal (2022). "Investigation of Microtremors Observed at Historic Masonry Townhouse Buildings after Nepal Earthquake". In: *Frontiers in Built Environment* 8, p. 918960. DOI: 10.3389/fbuil.2022.918960.

Murty, C. V. R. (2002). *Why Is Vertical Reinforcement Required in Masonry Buildings?* Kanpur, India: Indian Institute of Technology Kanpur.

Nafees, A., M. F. Javed, M. A. Musarat, M. Ali, F. Aslam and N. I. Vatin (2021). "FE Modelling and Analysis of Beam Column Joint Using Reactive Powder Concrete". In: *Crystals* 11.11, p. 1372. DOI: 10.3390/cryst11111372.

Nastri, E., M. Tenore and P. Todisco (2023). "Calibration of Concrete Damaged Plasticity Material Parameters for Tuff Masonry Types of the Campania Area". In: *Engineering Structures* 283, p. 115927. DOI: 10.1016/j.engstruct.2023.115927.

National Statistics Office (2024). *National Population and Housing Census 2021 – Housing and Household Dynamics in Nepal*. Thapathali, Kathmandu: National Statistics Office.

Nationalencyklopedin (n.d). *Jordbävning*. Access via Lund University Library. URL: https://www-ne-se.ludwig.lub.lu.se/ordb%C3%B6cker/search?d=ne_sv_ordbok&s=jordb%C3%A4vning (visited on 31/01/2026).

Nepal National Building Code (NBC) 109: Unreinforced Masonry (1994). Kathmandu, Nepal.

Nepal National Building Code NBC 105: Seismic Design of Buildings in Nepal (2020). Nepal.

Oxfam (12th May 2015). *Second strong earthquake hits Nepal—you can help*. URL: https://www.oxfamamerica.org/explore/stories/second-strong-earthquake-hits-nepalyou-can-help/ (visited on 15/03/2026).

Parisi, F. and N. Augenti (2014). "Displacement-Based Seismic Design of Unreinforced Masonry Buildings". In: *Proceedings of the 2nd European Conference on Earthquake Engineering and Seismology*. Istanbul, Turkey.

Paudel, K. (Jan. 2025). *Seismic Challenges in Nepal*. The Rising Nepal. URL: https://risingnepaldaily.com/news/55555 (visited on 31/01/2026).

Paultre, P. (2011). *Dynamics of Structures*. Great Britain and the United States: ISTE Ltd and John Wiley & Sons, Inc.

Petry, S. and K. Beyer (2014). "Influence of boundary conditions and size effect on the drift capacity of URM walls". In: *Engineering Structures* 65, pp. 76–88. DOI: 10.1016/j.engstruct.2014.01.048.

Rastogi, B. K. (2024). *Nepal Earthquake of 2015*. Springer Nature Singapore. ISBN: 978-981-97-4684-2. DOI: 10.1007/978-981-97-4684-2.

Resilient Structures Private Limited (5th June 2022). *Comparison of Construction Cost of Buildings Using CSEB and Fired Clay Bricks*. Report published via Build Up Nepal website. Resilient Structures Private Limited. URL: https://www.buildupnepal.com/wp-content/uploads/2022/07/report-on-cseb-cost-comparison-structural-performance.pdf (visited on 18/02/2026).

Shannag, M. J. and M. A. Alhassan (2005). "Seismic Upgrade of Interior Beam-Column Subassemblages with High-Performance Fiber-Reinforced Concrete Jackets". In: *ACI Structural Journal* 102.1, pp. 131–138.

Shrestha, H. D. (2012a). *Manual for Engineer – CSEB Green Buildings in Nepal*. Centre of Resilience Development. Nepal.

Shrestha, H. D. (2012b). *Manual for EQ Safe Building Construction*. Centre of Resilience Development. Nepal.

Singh, S. and P. Munjal (2017). "Bond Strength and Compressive Stress–Strain Characteristics of Brick Masonry". In: *Journal of Building Engineering* 9, pp. 10–17.

Sturm, T., P. B. Lourenço, A. Campos-Costa and L. F. Ramos (2014). "Mechanical Characterization of Dry-Stack Interlocking Compressed Earth Masonry". In: *Proceedings of the 9th International Masonry Conference*. Paper No. 1466. Guimarães, Portugal.

Subedi, S. K. (2020). "Study of Characteristics of Bricks Produced in Kathmandu, Nepal". In: *American Journal of Civil Engineering* 8.3, pp. 64–76. DOI: 10.11648/j.ajce.20200803.13.

Sujitha, V. S., A. G. Sriram, S. Raja, M. A. Rusho and S. Yishak (2026). "Flexural performance of RC beams strengthened with CFF and SCCFL sheets under cyclic loading". In: *Scientific Reports* 16, p. 6491. DOI: 10.1038/s41598-026-35884-w. URL: https://www.nature.com/articles/s41598-026-35884-w (visited on 04/02/2026).

Sveriges geologiska undersökning (2020). *Jordklotets uppbyggnad*. URL: https://www.sgu.se/om-geologi/jordklotets-uppbyggnad/ (visited on 31/01/2026).

Swiss Seismological Service (n.d). *What Are P, S, Love and Rayleigh Waves?* URL: http://seismo.ethz.ch/en/knowledge/faq/what-are-p-s-love-and-rayleigh-waves/ (visited on 31/01/2026).

Tariq, H., V. Sarhosis, M. A. Najafgholipour, G. Milani and M. Noori (2025). "Influence of Constraint Conditions on the In-plane Response of URM Walls: A Comprehensive Study using Finite Element Analysis and Design Code Provisions". In: *Bulletin of Earthquake Engineering*. DOI: 10.1007/s10518-025-02237-3.

Thapaliya, N., N. Karki, L. Badu, R. Karki, U. Bagale, I. Timalsina, M. Ali, S. Thapa and M. R. Bhatt (2024). "Study on Properties and Uses of Clay Burnt Bricks as a Popular Construction Material: A Case Study of Bhaktapur, Nepal". In: *Challenges in Earth-Based Interior Architecture: Current Issues in Earth-Based Materials, Construction Techniques and Approaches*. Proceedings of the 11th International Conference, 12–14 September 2024. Kayseri, Turkey, pp. 146–155.

Thudén, A. and A. Toivonen (2018). "Analysis of Earthquake Resistant Compressed Stabilised Earth Block Buildings in rural Nepal: Common construction errors and their influence on structural resistance". Master's thesis in Structural Engineering and Building Technology. Gothenburg, Sweden: Chalmers University of Technology. URL: https://publications.lib.chalmers.se/records/fulltext/256042/256042.pdf (visited on 06/02/2026).

Tomaževič, M. (1999). *Earthquake-Resistant Design of Masonry Buildings*. Vol. 1. London: Imperial College Press.

U.S. Geological Survey (6th Aug. 2019). *Earthquake Hazards 201 – Technical Q&A*. Accessed 2026-02-06. URL: https://www.usgs.gov/programs/earthquake-hazards/science/earthquake-hazards-201-technical-qa (visited on 06/02/2026).

U.S. Geological Survey (n.d.). *Earthquake Hazards Program Glossary: Spectral acceleration (SA)*. Accessed 2026-02-06. URL: https://www.usgs.gov/glossary/earthquake-hazards-program (visited on 06/02/2026).

United Nations Development Programme (UNDP) (2024). *Assessment of Brick, Cement and Steel Sectors in Nepal*. Report. UNDP.

Wald, D. J., V. Quitoriano, T. H. Heaton, H. Kanamori, C. W. Scrivner and C. B. Worden (1999). *Relationships between Peak Ground Acceleration, Peak Ground Velocity, and Modified Mercalli Intensity in California*. USGS publication. U.S. Geological Survey. URL: https://pubs.usgs.gov/publication/70021541 (visited on 06/02/2026).

Wang, H., H. Xiao, X. Cui, S. Yang, M. M. Nadakatti and Q. Guo (2023). "Influence of Uneven Subgrade Frost Heave on Deformation and Damage of CRTSIII Slab Track". In: *Applied Sciences* 13.9, p. 5345. DOI: 10.3390/app13095345.

Ventura, C. E. (2007). *The Response Spectrum (Response Spectrum Seminar, Lecture 4)*. Lecture notes/handout. University of British Columbia / CSCE Vancouver Section seminar material. URL: https://www.caee.ca/files/Publications/Lecture-4-Slide-Handouts.pdf (visited on 06/02/2026).

Xiao, Y., Z. Chen, J. Zhou, Y. Leng and R. Xia (2017). "Concrete Plastic-Damage Factor for Finite Element Analysis: Concept, Simulation, and Experiment". In: *Advances in Mechanical Engineering* 9.9, p. 1687814017719642. DOI: 10.1177/1687814017719642.

Appendix A

Material Parameters for CDP

A.1 CSEB

Table A.1: Abaqus CDP input parameters for CSEB.

CSEB					
Elasticity					
Young's modulus (MPa)	1421.194				
Poisson's ratio (-)	0.35				
Plasticity (CDP parameters)					
	(ψ)	(ϵ)	σ_{b0}/σ_{c0}	K_c	(μ_v)
	16	0.1	1.16	0.667	0
Compressive behaviour		**Tensile behaviour**			
Yield stress (MPa)	Inelastic strain	Stress (MPa)	Cracking strain		
3.847923667	0.000000000	0.000000000	0.000000		
5.291586667	0.000000000	0.529158667	0.000000		
5.211494333	0.000181720	0.407452173	0.000179		
4.821705667	0.000669457	0.238121400	0.001322		
5.029158667	0.004727666	0.052915867	0.003202		

Table A.2: Abaqus CDP input parameters for mortar/grout.

A.2 Mortar/Grout

Mortar/grout					
Elasticity					
Young's modulus (MPa)	2498.716				
Poisson's ratio (-)	0.20				
Plasticity (CDP parameters)					
	(ψ)	(ϵ)	σ_{b0}/σ_{c0}	K_c	(μ_v)
	16	0.1	1.16	0.667	0
Compressive behaviour		**Tensile behaviour**			
Yield stress (MPa)	Inelastic strain	Stress (MPa)	Cracking strain		
0.00000	0.00000	0.00	0.000000		
0.23333	0.00000	0.35	0.000000		
2.00000	0.00000	0.27	0.000067		
3.47667	0.00000	0.16	0.000494		
2.60000	0.00062	0.03	0.001197		
1.37667	0.00144				

A.3 Reinforcement

Table A.3: FE 415 steel input used for reinforcement modelling in Abaqus.

FE 415 (Abaqus input)	
Elasticity	
Young's modulus (GPa)	200
Poisson's ratio (-)	0.30
Plasticity (stress-plastic strain)	
Stress (MPa)	**Plastic strain (-)**
415	0
415	0.002925
460	0.0077
500	0.0105
510	0.01445
Ductile damage initiation	
Fracture strain, ε_D^{pl}	0.01445
Stress triaxiality, η	1/3
Strain rate, $\dot{\varepsilon}^{pl}$	0

Appendix B

Derivation of vertical load applied at the pier top

This appendix documented the derivation of the axial pre-compression applied at the top of each pier. The vertical load was intended to represent superstructure effects through self-weight of masonry above the lintel band, self-weight of the lintel and roof bands, and the permanent roof load. All quantities were converted to an equivalent uniformly distributed pressure applied on the pier top surface in Abaqus.

Input data

Input values for roof load and band properties were taken from a previous Build Up Nepal master's thesis with the same building layout and geometry (Thudén and Toivonen, 2018). Table B.1 summarised the adopted inputs.

Table B.1: Input data used for axial load estimation.

Component	Value
Lintel band (concrete)	$\rho = 2400$ kg/m^3
Roof band (concrete)	$\rho = 2400$ kg/m^3
Roof permanent load	$g = 0.157$ kN/m^2
Tributary width (per load-bearing wall)	$b_t = 2.55$ m

CSEB pier

The height of masonry above the lintel band was computed as the difference between the roof-band level (2.545 m) and the lintel-band level (2.03 m), yielding

$$h = 2.545 - 2.03 = 0.515 \text{ m}. \tag{B.1}$$

With CSEB density $\rho = 1800$ kg/m^3, the unit weight became

$$\gamma = \rho g \approx 1800 \cdot 9.81/1000 \approx 17.66 \text{ kN/m}^3. \tag{B.2}$$

Using wall thickness $t = 0.15$ m, the line load from masonry above the lintel band was

$$q_{\text{CSEB}} = \gamma \, t \, h \approx 17.66 \cdot 0.15 \cdot 0.515 \approx 1.36 \text{ kN/m}. \tag{B.3}$$

The self-weight of the lintel band and roof band was computed with $\rho = 2400$ kg/m^3 and cross-section 0.10×0.15 m^2:

$$q_{\text{lintel}} = q_{\text{roofband}} \approx 0.10 \cdot 0.15 \cdot 2400 \cdot 9.81/1000 \approx 0.35 \text{ kN/m}. \tag{B.4}$$

The roof permanent load was converted to a line load using the tributary width:

$$q_{\text{roof}} = g\, b_t = 0.157 \cdot 2.55 \approx 0.40 \text{ kN/m}. \tag{B.5}$$

The total vertical line load became

$$q_{\text{tot}} = q_{\text{CSEB}} + q_{\text{lintel}} + q_{\text{roofband}} + q_{\text{roof}} \approx 1.36 + 0.35 + 0.35 + 0.40 = 2.46 \text{ kN/m}. \tag{B.6}$$

For Abaqus implementation, the line load was converted to a uniformly distributed pressure by dividing by the wall thickness:

$$p_{\text{CSEB}} = \frac{q_{\text{tot}}}{t} = \frac{2.46}{0.15} \approx 16.4 \text{ kN/m}^2. \tag{B.7}$$

Fired clay brick pier

The same height above lintel band was assumed ($h = 0.515$ m). With brick density $\rho = 1750$ kg/m^3, the unit weight became

$$\gamma \approx 1750 \cdot 9.81/1000 \approx 17.17 \text{ kN/m}^3. \tag{B.8}$$

Using brick wall thickness $t = 0.115$ m, the line load from masonry above the lintel band was

$$q_{\text{brick}} = \gamma\, t\, h \approx 17.17 \cdot 0.115 \cdot 0.515 \approx 1.02 \text{ kN/m}. \tag{B.9}$$

The roof permanent line load was taken as in the CSEB case, $q_{\text{roof}} \approx 0.40$ kN/m. The lintel band and roof band were assumed to have the same density (2400 kg/m^3) and height (0.10 m), while the band depth was taken as the brick wall thickness (0.115 m), yielding a cross-sectional area $A = 0.10 \cdot 0.115$ m^2 and

$$q_{\text{lintel}} = q_{\text{roofband}} \approx 0.10 \cdot 0.115 \cdot 2400 \cdot 9.81/1000 \approx 0.27 \text{ kN/m}. \tag{B.10}$$

The total vertical line load became

$$q_{\text{tot}} \approx q_{\text{brick}} + q_{\text{lintel}} + q_{\text{roofband}} + q_{\text{roof}} \approx 1.02 + 0.27 + 0.27 + 0.40 = 1.96 \text{ kN/m}. \tag{B.11}$$

The equivalent pressure applied in Abaqus was computed as

$$p_{\text{brick}} = \frac{q_{\text{tot}}}{t} = \frac{1.96}{0.115} \approx 17.0 \text{ kN/m}^2. \tag{B.12}$$

Appendix C

Finite element model setup

This appendix presents supplementary figures related to the finite element modelling of the CSEB walls. The figures are grouped into unit-level geometry and mesh, squat wall assembly, and slender wall assembly in order to clarify how the numerical models were constructed.

C.1 CSEB unit geometry and mesh

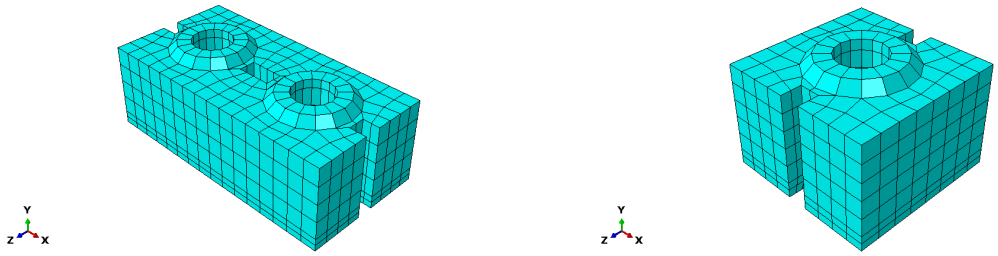

(a) Three-dimensional view of the CSEB unit geometry.

(b) Three-dimensional view of the half-unit geometry used for modelling details.

Figure C.1: Geometric definition of the CSEB unit used in the micromodelling approach.

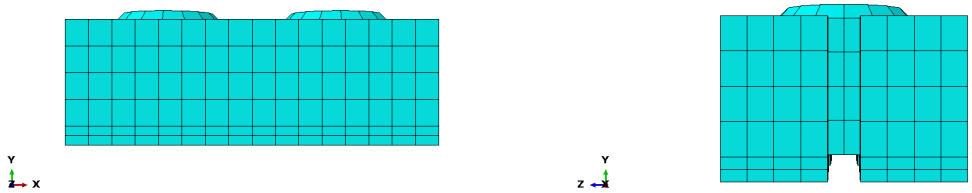

(a) View in the XY-plane.

(b) View in the YZ-plane.

Figure C.2: Orthogonal views of the CSEB unit and its finite element discretisation.

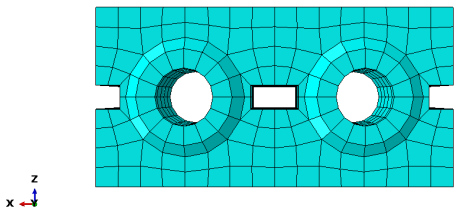

(a) View in the XZ-plane.

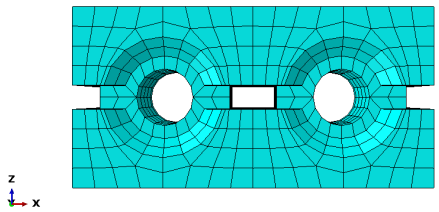

(b) XZ-view showing the underside geometry in greater detail.

Figure C.3: Additional orthogonal views of the CSEB unit geometry and mesh.

C.2 Squat wall assembly

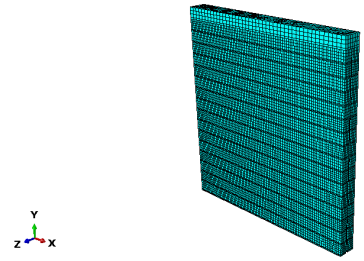

(a) 3D view of the squat wall assembly.

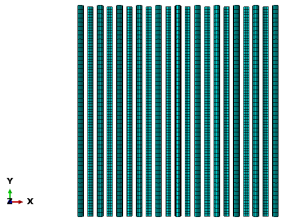

(b) Detail of grout/reinforcement layout in the squat wall assembly.

Figure C.4: Overall model setup for the squat CSEB wall.

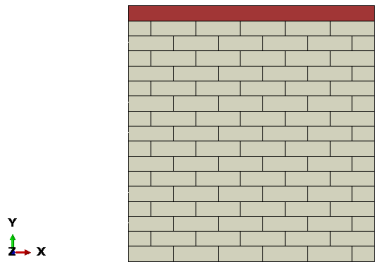

(a) Material assignment in the squat wall assembly.

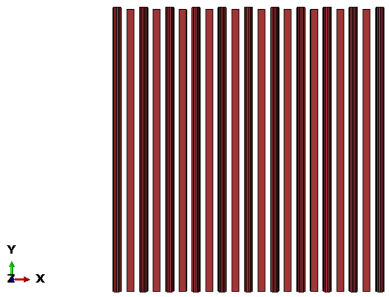

(b) Grout assignment in the squat wall assembly.

Figure C.5: Material definition for the squat CSEB wall model.

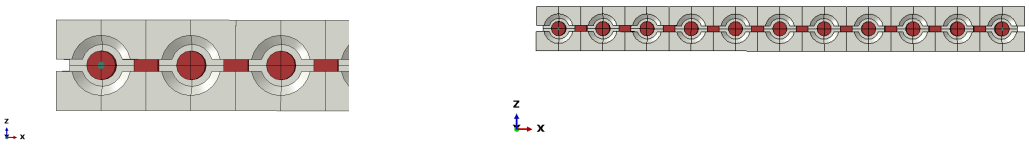

(a) Edge detail of the underside wire view for the squat wall assembly.

(b) Underside wire view of the squat wall assembly.

Figure C.6: Additional modelling views for the squat wall assembly.

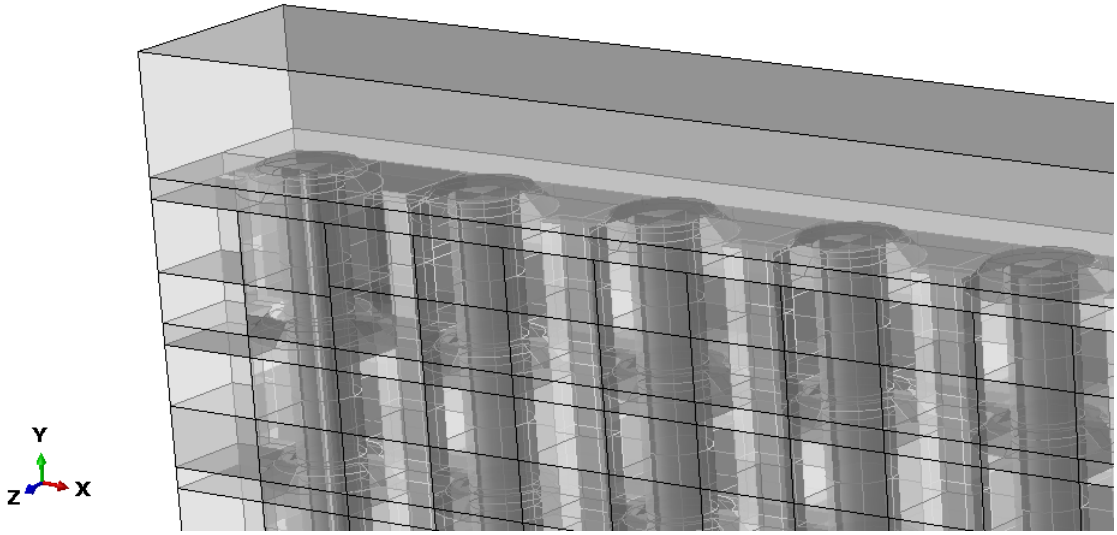

Figure C.7: Transparent assembly view of the reinforced CSEB wall model showing the internal grout cores and the overall wall geometry.

C.3 Slender wall assembly

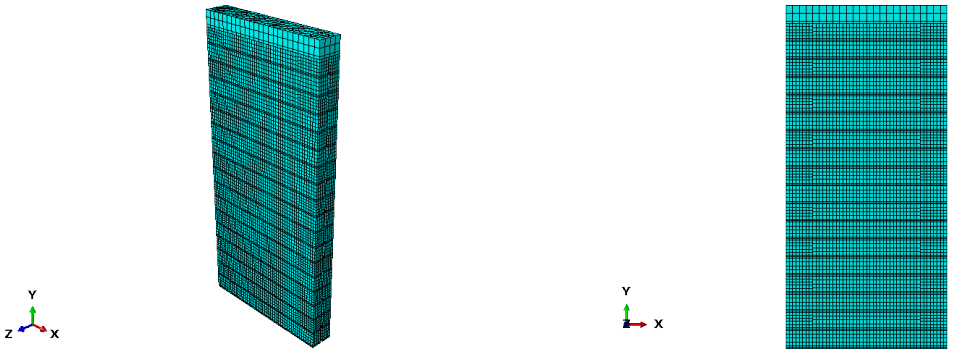

(a) 3D view of the slender wall assembly.

(b) XY view of the slender wall assembly.

Figure C.8: Overall geometry and mesh of the slender CSEB wall model.

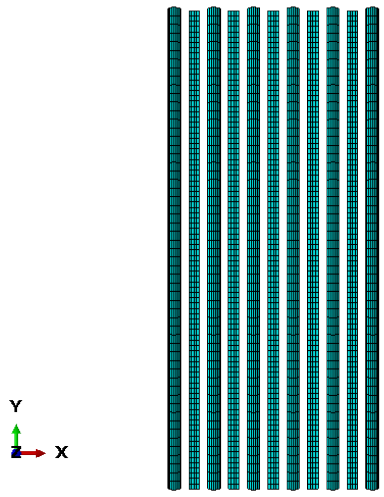

Figure C.9: Detail of grout/reinforcement layout in the slender wall assembly.

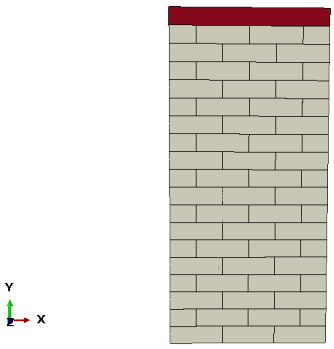

(a) Material assignment in the slender wall assembly.

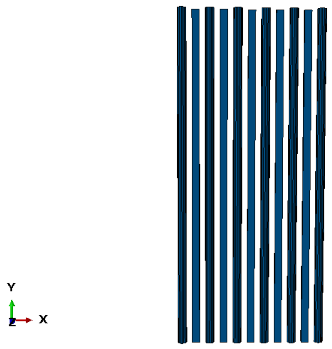

(b) Grout assignment in the slender wall assembly.

Figure C.10: Material definition for the slender CSEB wall model.

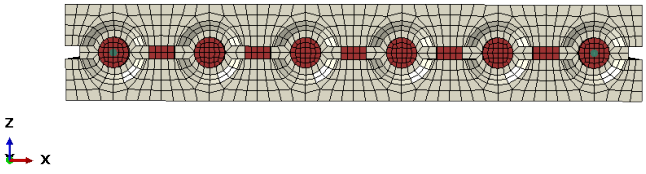

Figure C.11: Underside view of the slender wall assembly.

C.4 Fired brick wall assemblies

C.4.1 Squat wall assembly

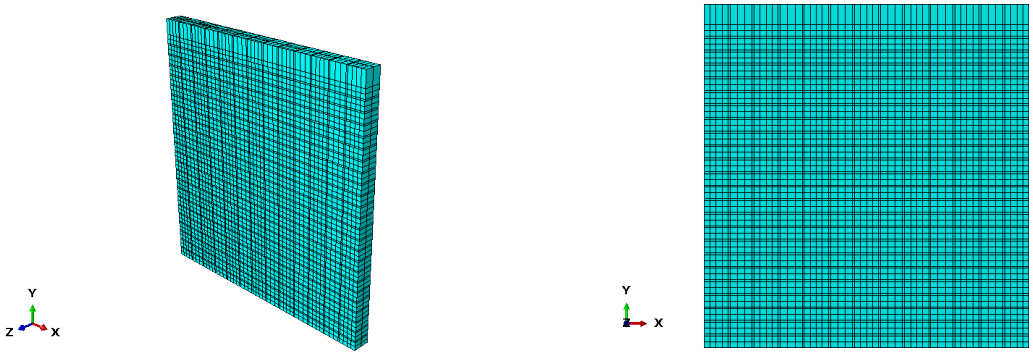

(a) Three-dimensional view of the squat fired brick wall assembly.

(b) Planar view of the squat fired brick wall assembly.

Figure C.12: Geometry and finite element discretisation of the squat fired brick wall model.

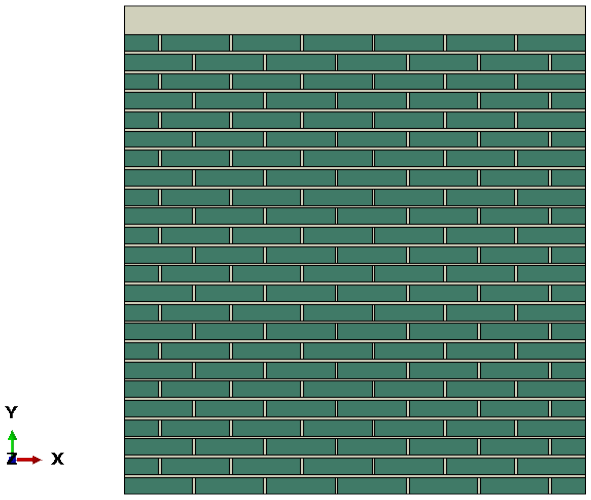

Figure C.13: Material definition of the squat fired brick wall model.

C.4.2 Slender wall assembly

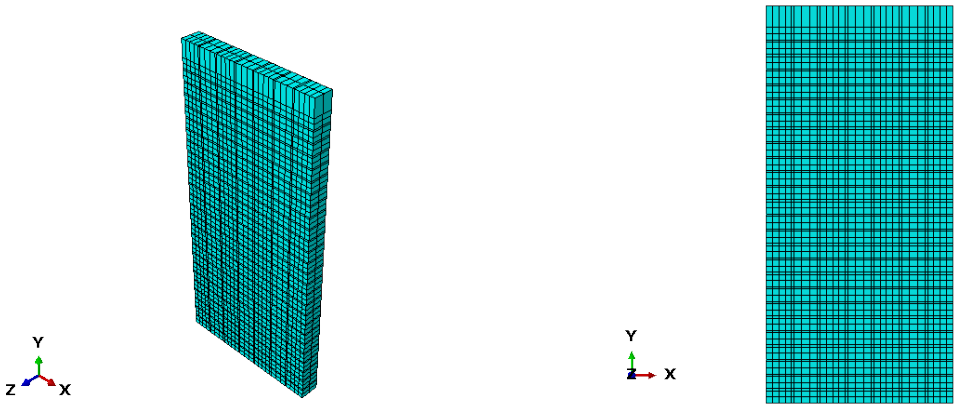

(a) Three-dimensional view of the slender fired brick wall assembly.

(b) Planar view of the slender fired brick wall assembly.

Figure C.14: Geometry and finite element discretisation of the slender fired brick wall model.

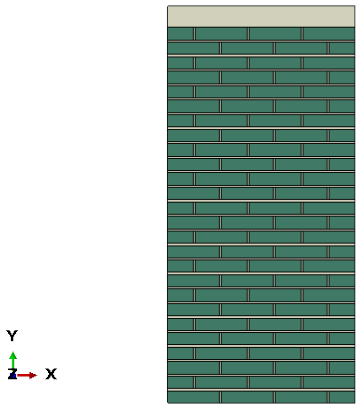

Figure C.15: Material definition of the slender fired brick wall model.

Appendix D

ABAQUS Visualization

D.1 Fired Brick

D.1.1 Squat wall

Fixed-Fixed

Low Pre-Compression

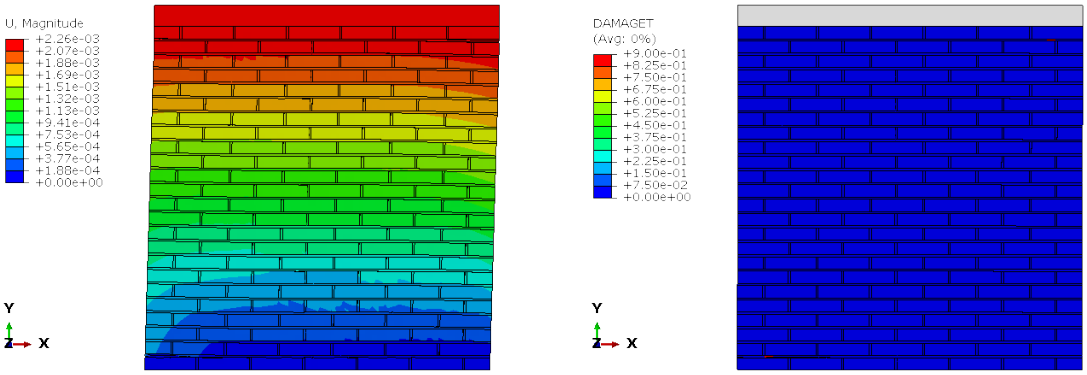

(a) U (Displacement, scaled by factor 20) **(b)** d_t (DAMAGET)

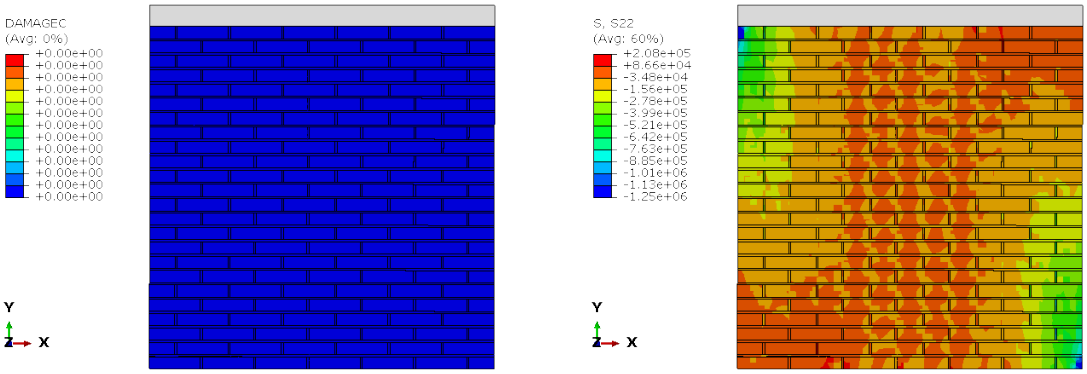

(c) d_c (DAMAGEC) **(d)** S_{22}

Figure D.1: Fired brick squat wall, fixed-fixed, low pre-compression: peak state ($V_{\max}$)

.

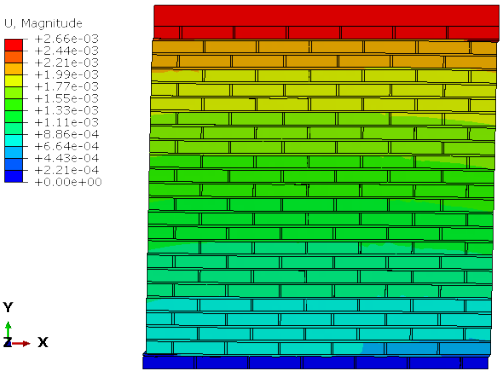

(a) U (Displacement, scaled by factor 20)

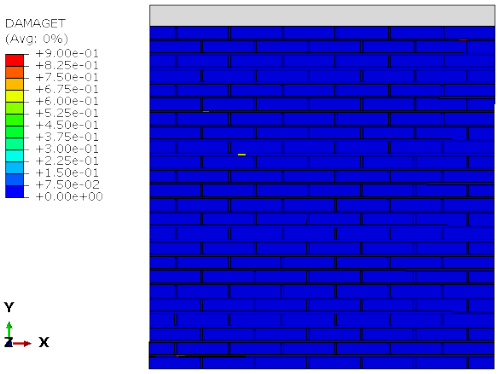

(b) d_t (DAMAGET)

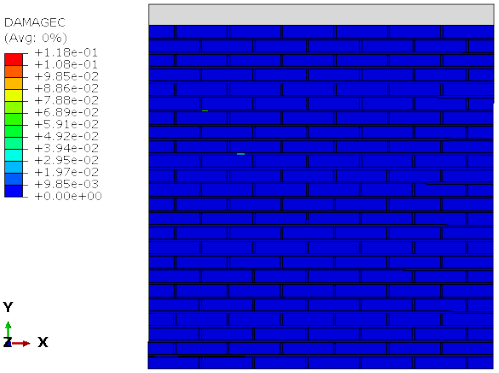

(c) d_c (DAMAGEC)

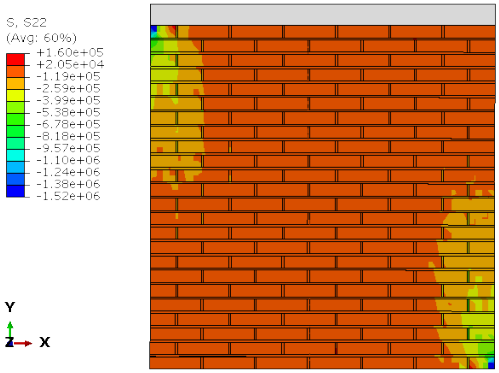

(d) S_{22}

Figure D.2: Fired brick squat wall, fixed-fixed, low pre-compression: V_{80}.

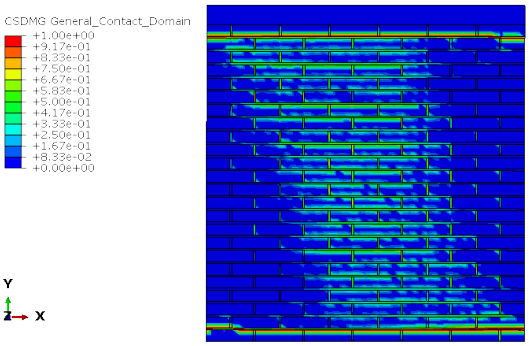

(a) Cohesive damage (CD), V_{80}.

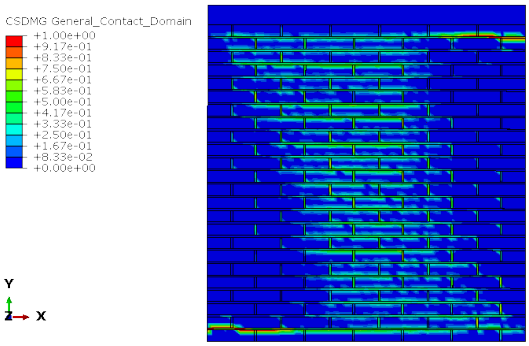

(b) Cohesive damage (CD), ($V_{\max}$)

Figure D.3: Fired brick squat wall, fixed-fixed, low pre-compression: cohesive damage (CD) at V80 and at peak state ($V_{\max}$).

High Pre-Compression

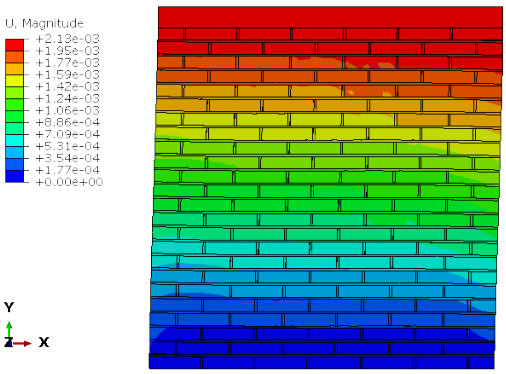

(a) U (Displacement, scaled by factor 20)

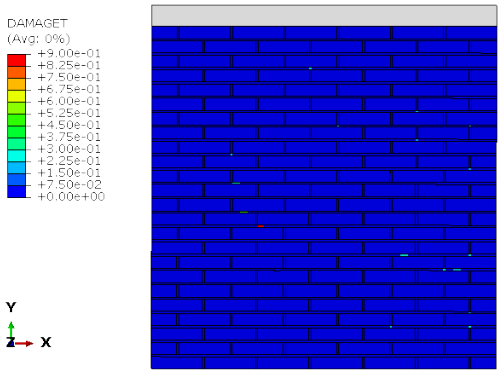

(b) d_t (DAMAGET)

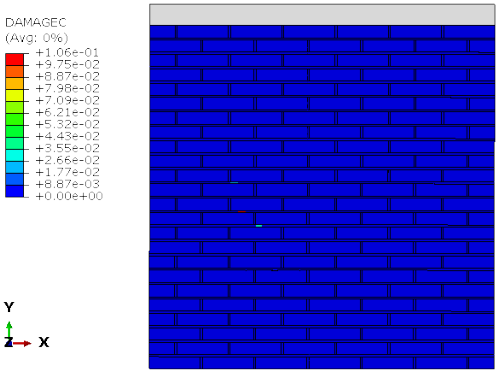

(c) d_c (DAMAGEC)

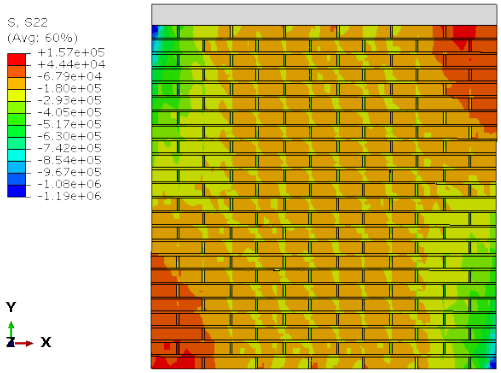

(d) S_{22}

Figure D.4: Fired brick squat wall, fixed-fixed, high pre-compression: peak state ($V_{\max}$).

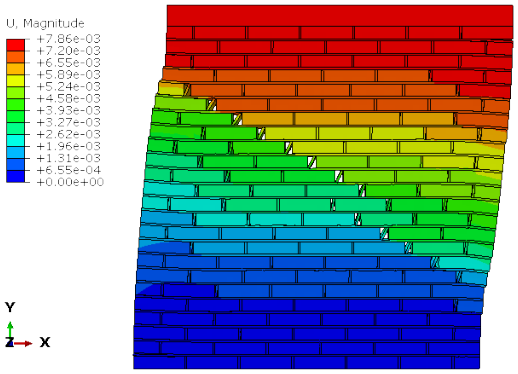

(a) U (Displacement, scaled by factor 20)

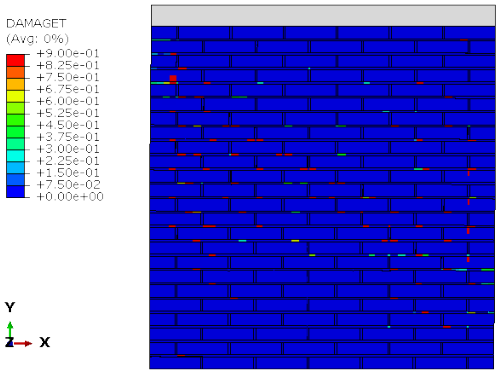

(b) d_t (DAMAGET)

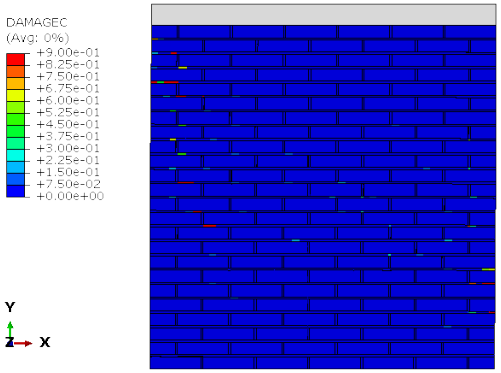

(c) d_c (DAMAGEC)

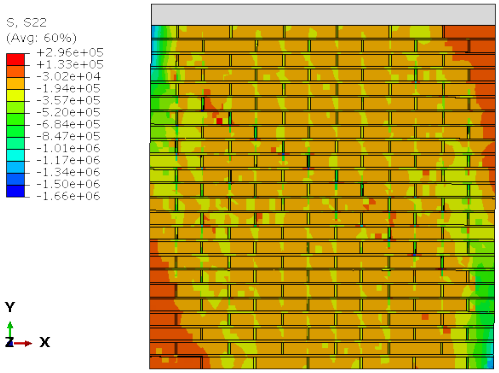

(d) S_{22}

Figure D.5: Fired brick squat wall, fixed-fixed, high pre-compression: V_{80}.

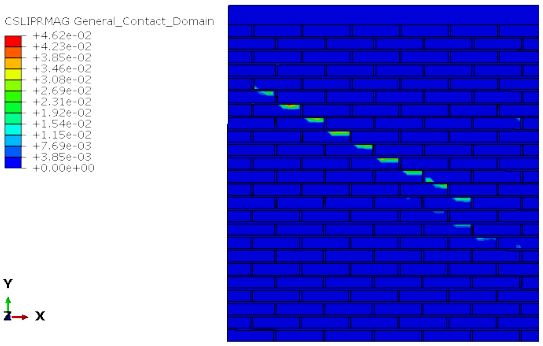

(a) Cohesive damage (CD), V_{80}.

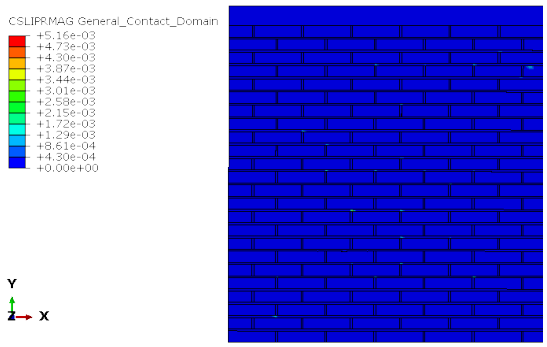

(b) Cohesive damage (CD), peak state ($V_{\max}$).

Figure D.6: Fired brick squat wall, fixed-fixed, high pre-compression: cohesive damage (CD) at V80 and at peak state ($V_{\max}$).

Cantilever

Low Pre-Compression

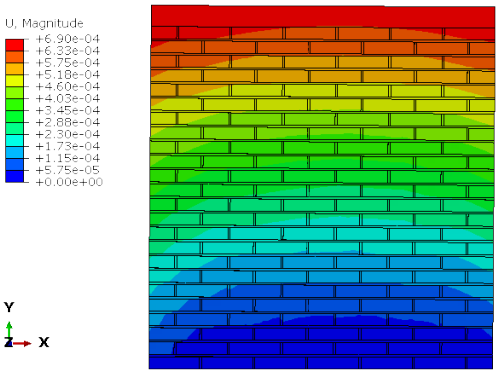

(a) U (Displacement, scaled by factor 20)

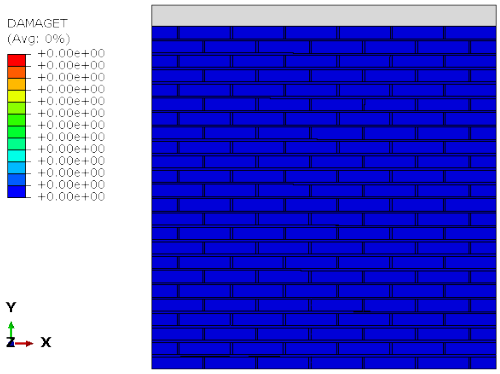

(b) d_t (DAMAGET)

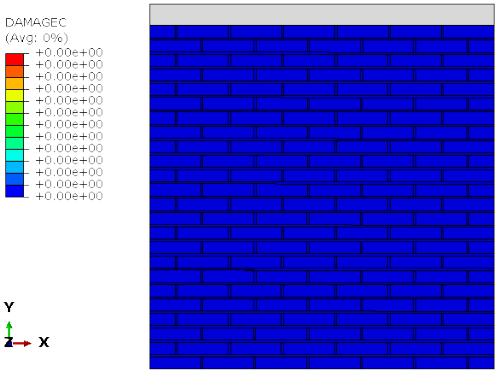

(c) d_c (DAMAGEC)

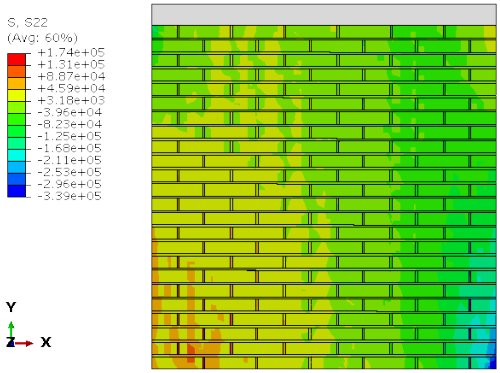

(d) S_{22}

Figure D.7: Fired brick squat wall, cantilever, low pre-compression: peak state ($V_{\max}$).

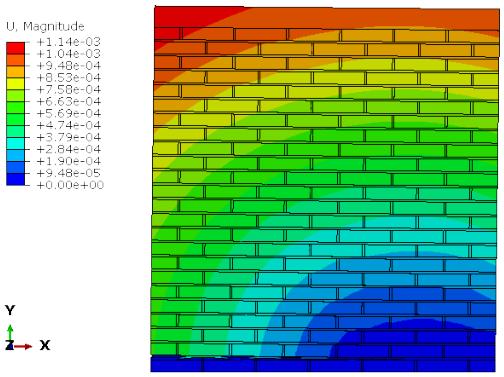

(a) U (Displacement, scaled by factor 20)

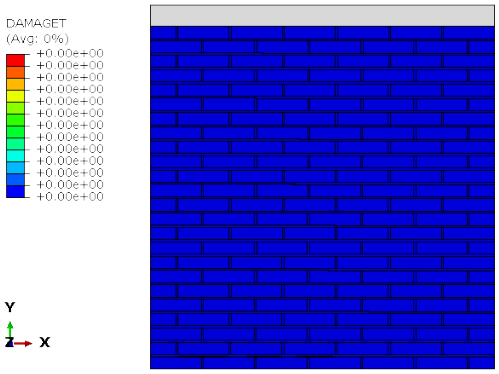

(b) d_t (DAMAGET)

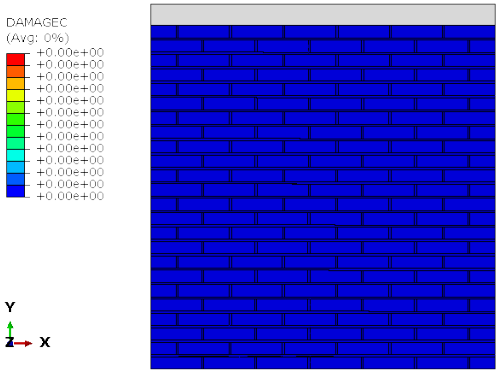

(c) d_c (DAMAGEC)

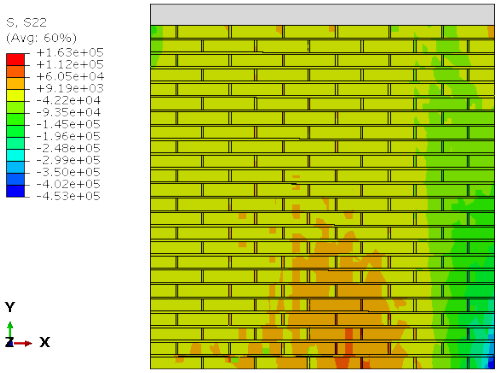

(d) S_{22}

Figure D.8: Fired brick squat wall, cantilever, low pre-compression: V_{80}.

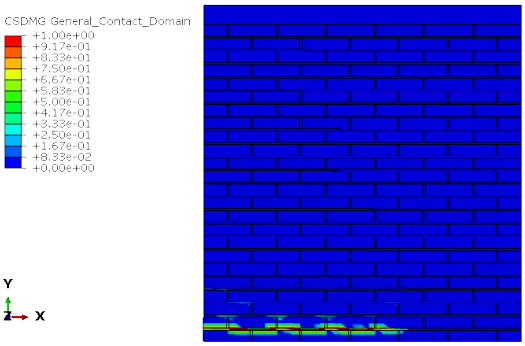

(a) Cohesive damage (CD), V_{80}.

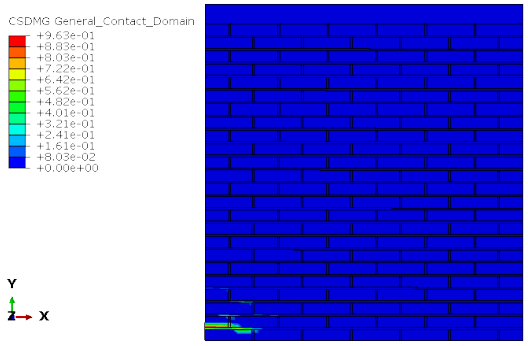

(b) Cohesive damage (CD), peak state ($V_{\max}$).

Figure D.9: Fired brick squat wall, cantilever, low pre-compression: cohesive damage (CD) at V_{80} and at $V_{\max}$.

High Pre-Compression

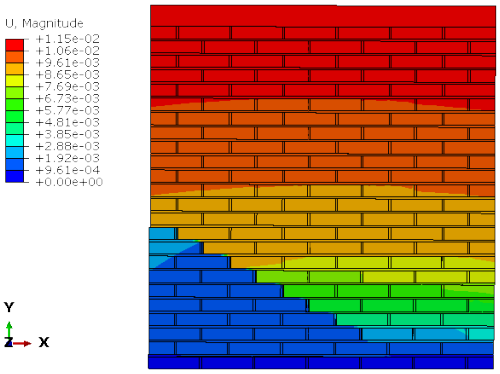

(a) U (Displacement)

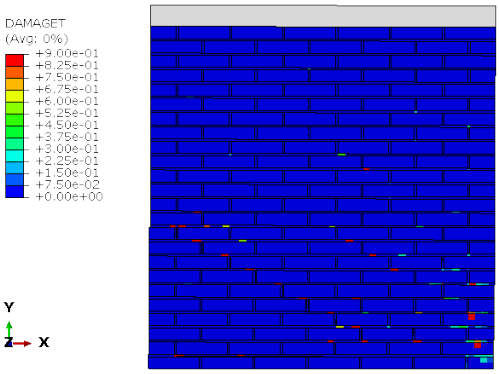

(b) d_t (DAMAGET)

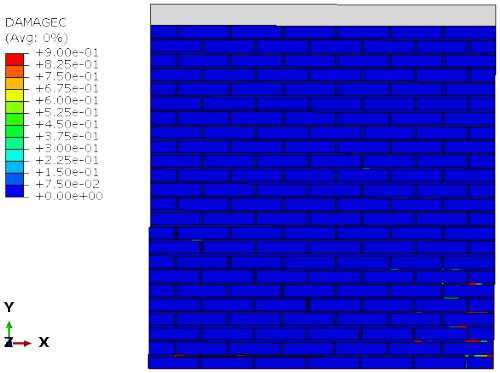

(c) d_c (DAMAGEC)

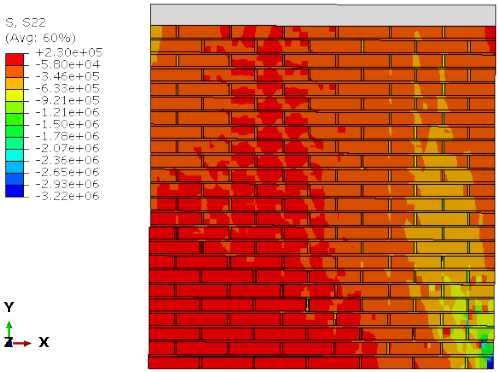

(d) S_{22}

Figure D.10: Fired brick squat wall, cantilever, high pre-compression: peak state ($V_{\max}$).

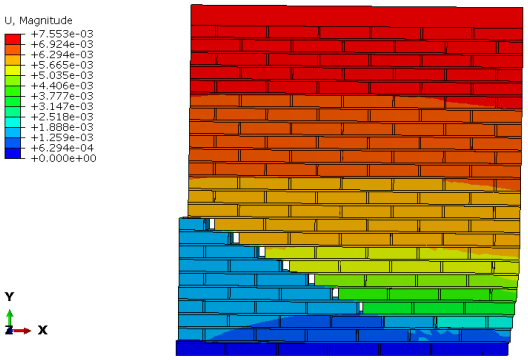

(a) U (Displacement, scaled by factor 10)

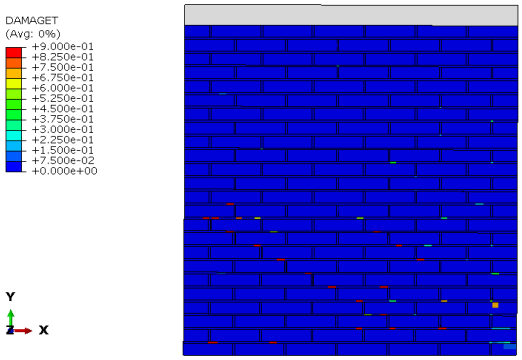

(b) d_t (DAMAGET)

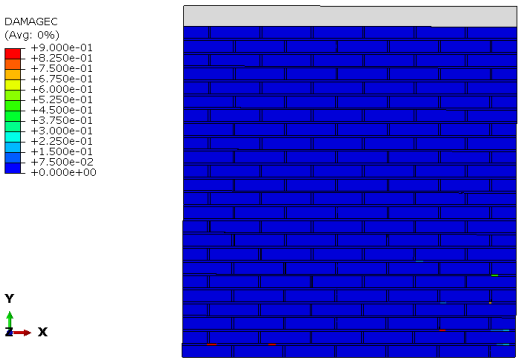

(c) d_c (DAMAGEC)

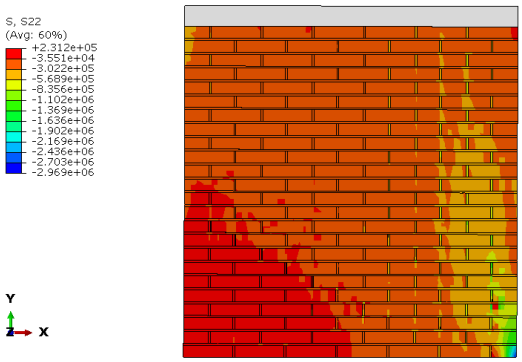

(d) S_{22}

Figure D.11: Fired brick squat wall, cantilever, high pre-compression: peak state ($V_{\max}$).

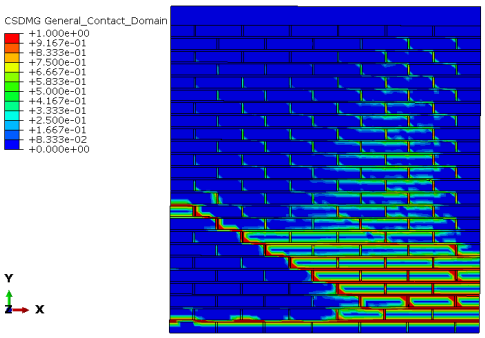

(a) Cohesive damage (CD), V_{80}.

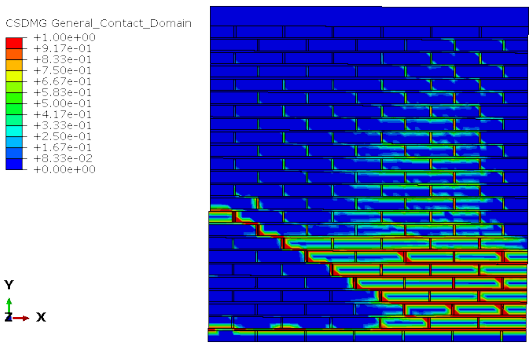

(b) Cohesive damage (CD), peak state ($V_{\max}$).

Figure D.12: Fired brick squat wall, cantilever, high pre-compression: cohesive damage (CD) at V_{80} and at $V_{\max}$.

D.1.2 Slender wall

Fixed-Fixed

Low pre-compression

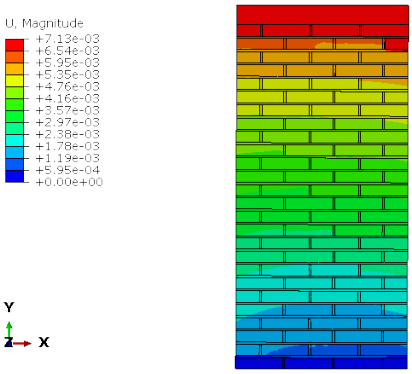

(a) U (Displacement)

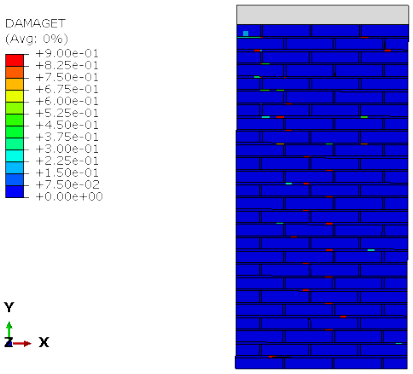

(b) d_t (DAMAGET)

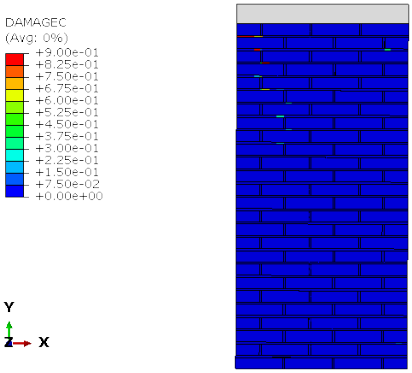

(c) d_c (DAMAGEC)

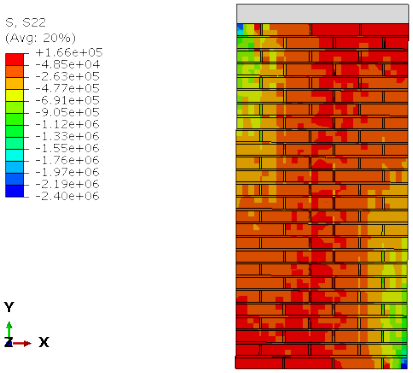

(d) S_{22}

Figure D.13: Fired brick slender wall, fixed-fixed, low pre-compression: peak state ($V_{\max}$).

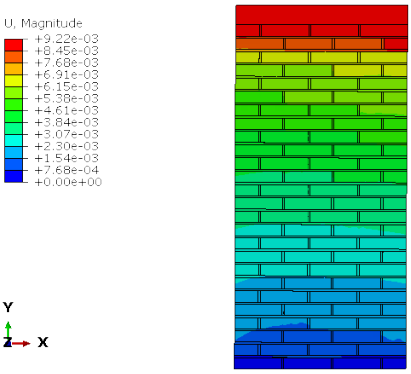

(a) (U) Displacement

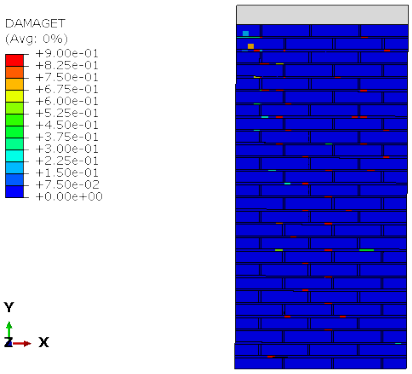

(b) d_t (DAMAGET)

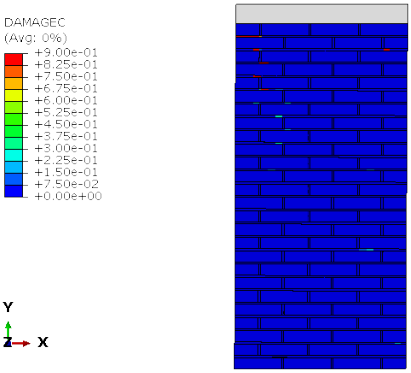

(c) d_c (DAMAGEC)

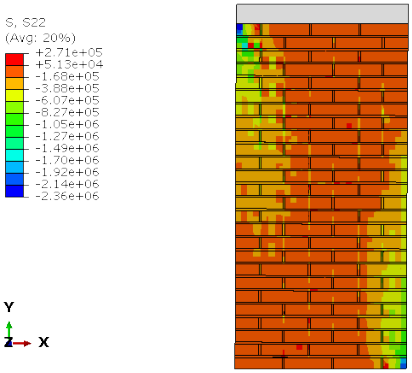

(d) S_{22}

Figure D.14: Fired brick slender wall, fixed-fixed, low pre-compression: (V_{80}).

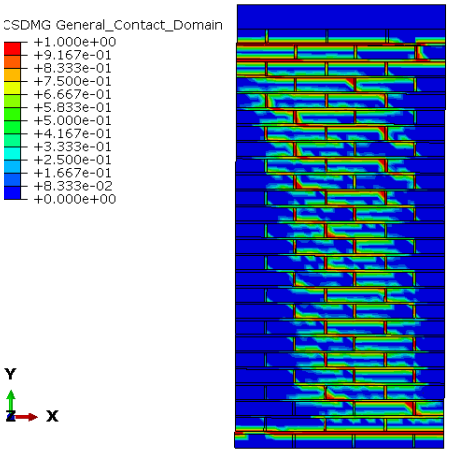

(a) Cohesive damage (CD), V_{80}.

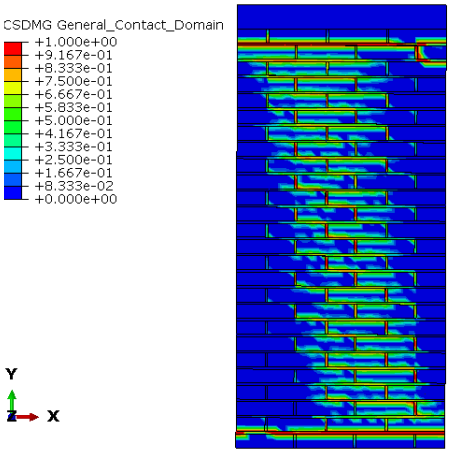

(b) Cohesive damage (CD), peak state ($V_{\max}$).

Figure D.15: Fired brick slender wall, fixed-fixed, low pre-compression: cohesive damage (CD) at V_{80} and at $V_{\max}$.

High pre-compression

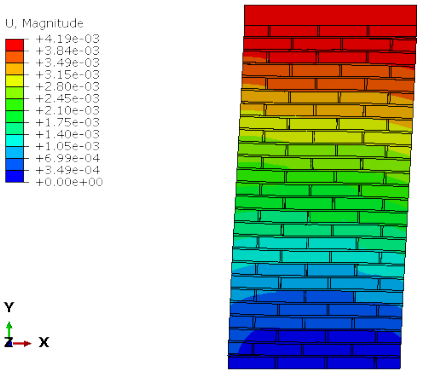

(a) U (Displacement, scaled by factor 20)

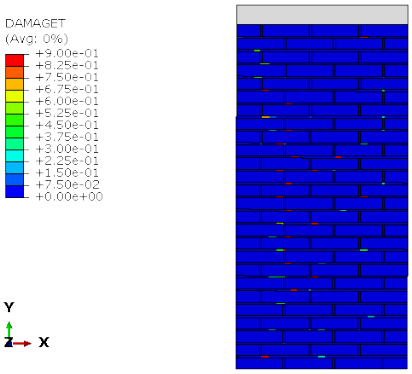

(b) d_t (DAMAGET)

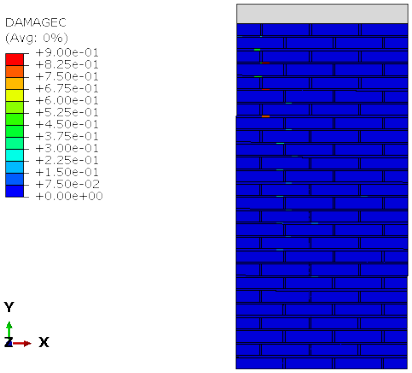

(c) d_c (DAMAGEC)

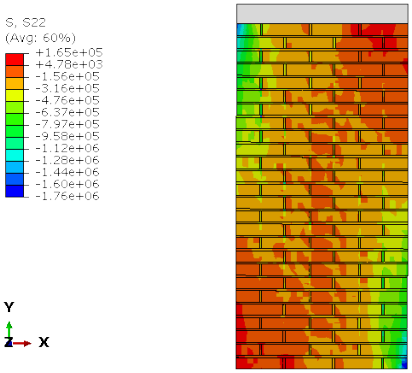

(d) S_{22}

Figure D.16: Fired brick slender wall, fixed-fixed, high pre-compression: peak state ($V_{\max}$).

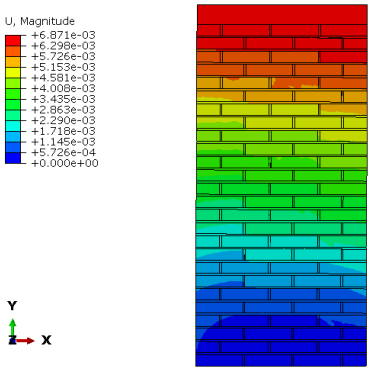

(a) U (Displacement, scaled by factor 20)

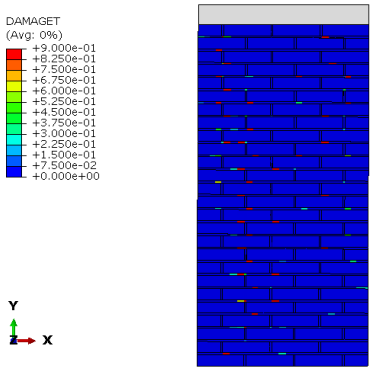

(b) d_t (DAMAGET)

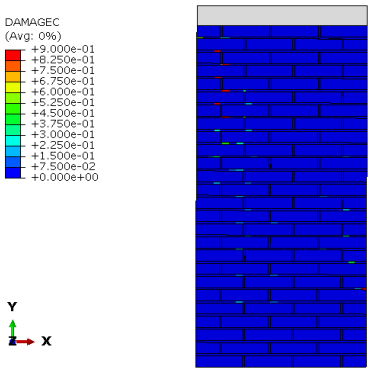

(c) d_c (DAMAGEC)

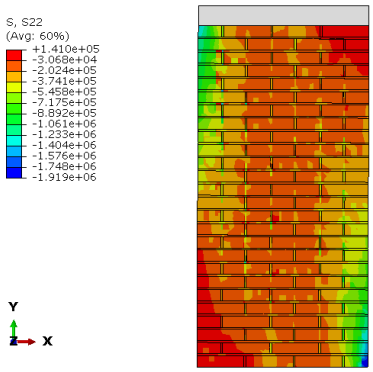

(d) S_{22}

Figure D.17: Fired brick slender wall, fixed-fixed, high pre-compression: drift $\approx 0.4\%$.

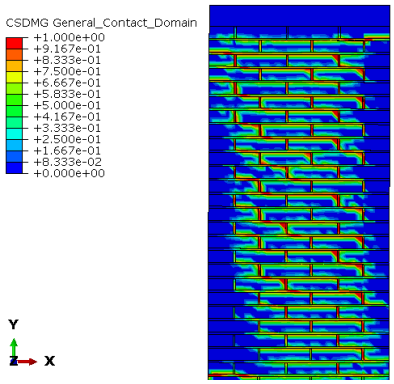

(a) Cohesive damage (CD), V_{80}.

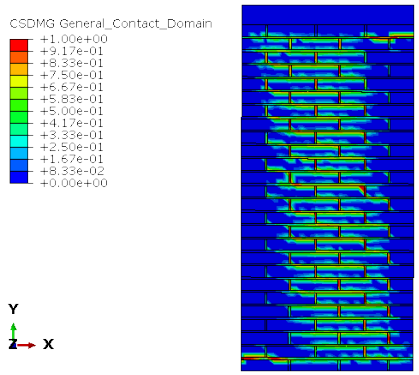

(b) Cohesive damage (CD), peak state ($V_{\max}$).

Figure D.18: Fired brick slender wall, fixed-fixed, high pre-compression: cohesive damage (CD) at drift $\approx 0.4\%$ and at $V_{\max}$.

Cantilever

Low pre-compression

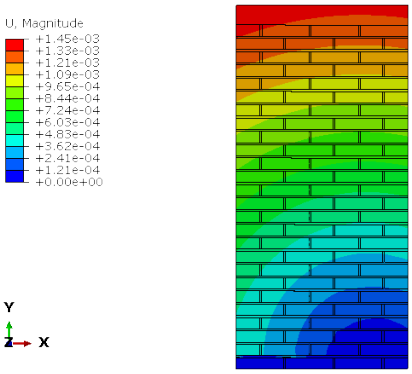

(a) U (Displacement)

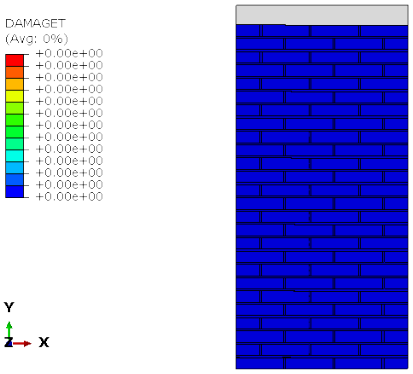

(b) d_t (DAMAGET)

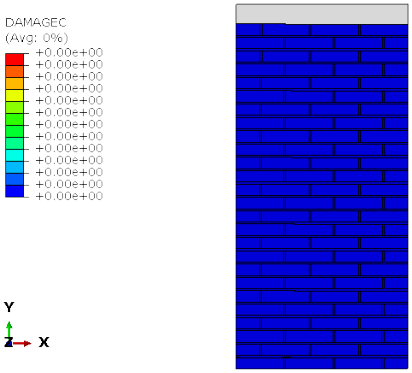

(c) d_c (DAMAGEC)

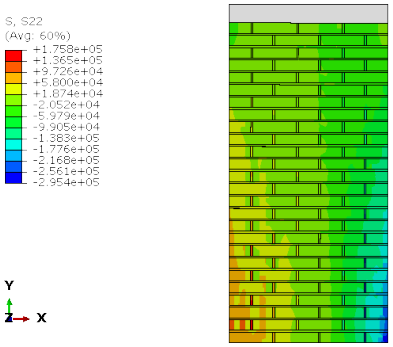

(d) S_{22}

Figure D.19: Fired brick slender wall, cantilever, low pre-compression: peak state ($V_{\max}$).

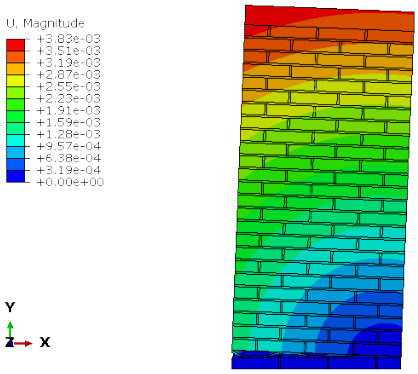

(a) U (Displacement, scaled by factor 20)

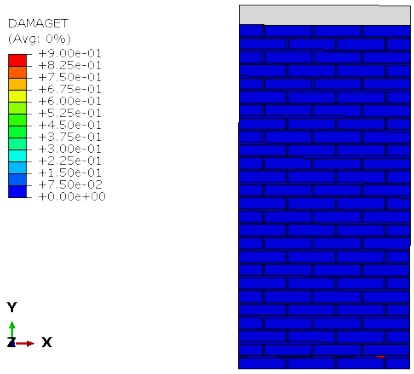

(b) d_t (DAMAGET)

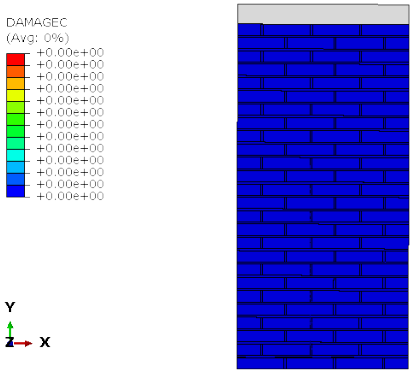

(c) d_c (DAMAGEC)

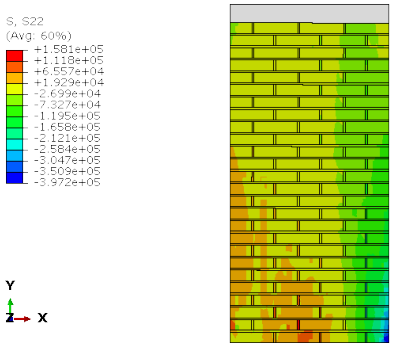

(d) S_{22}

Figure D.20: Fired brick slender wall, cantilever, low pre-compression: V_{80}.

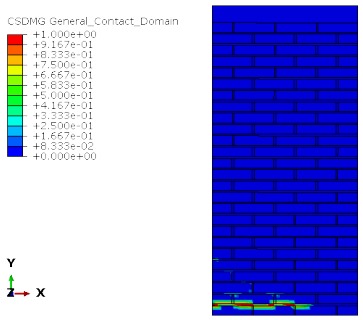

(a) Cohesive damage (CD), V_{80}.

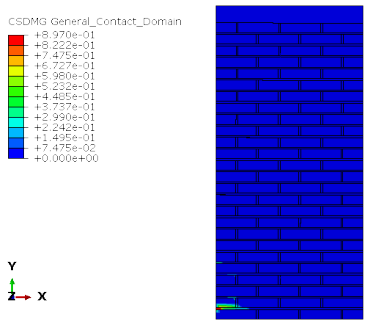

(b) Cohesive damage (CD), peak state ($V_{\max}$).

Figure D.21: Fired brick slender wall, cantilever, low pre-compression: cohesive damage (CD) at V_{80} and at $V_{\max}$.

High pre-compression

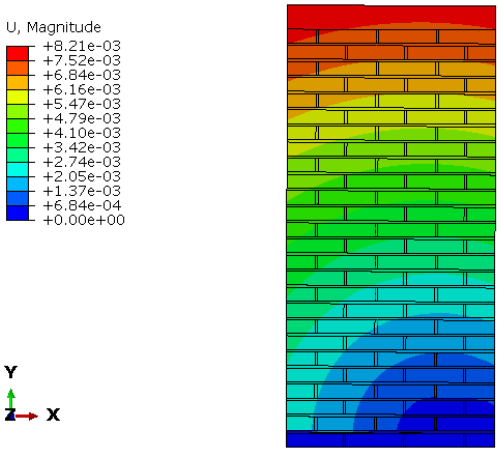

(a) U (Displacement)

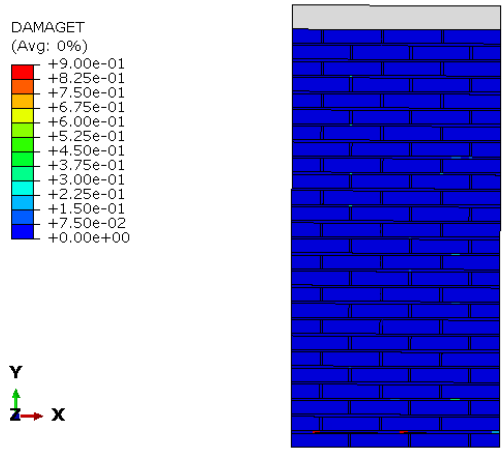

(b) d_t (DAMAGET)

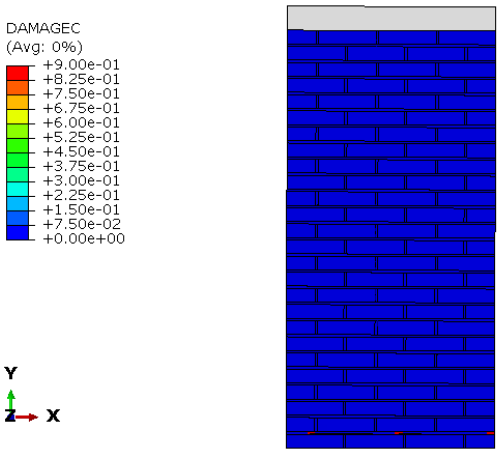

(c) d_c (DAMAGEC)

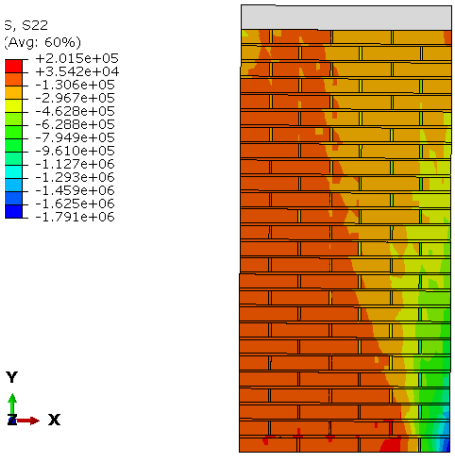

(d) S_{22}

Figure D.22: Fired brick slender wall, cantilever, high pre-compression: peak state ($V_{\max}$).

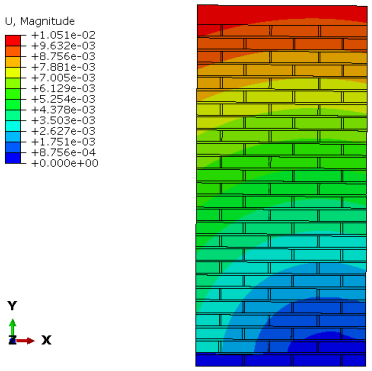

(a) U (Displacement)

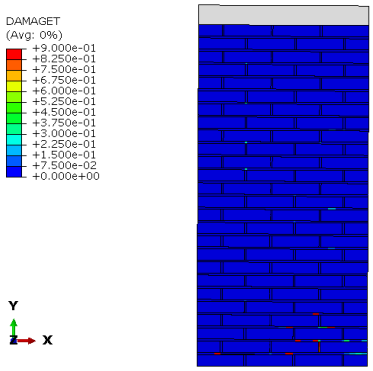

(b) d_t (DAMAGET)

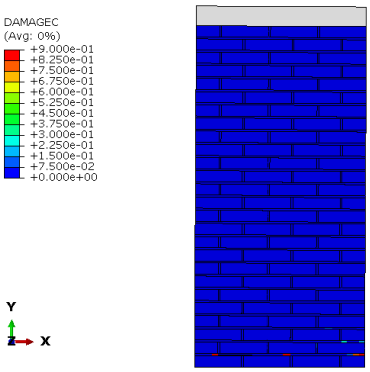

(c) d_c (DAMAGEC)

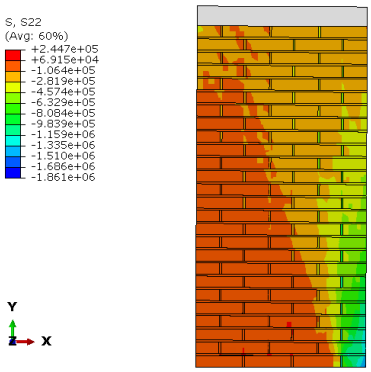

(d) S_{22}

Figure D.23: Fired brick slender wall, cantilever, high pre-compression: drift $\approx 0.6\%$.

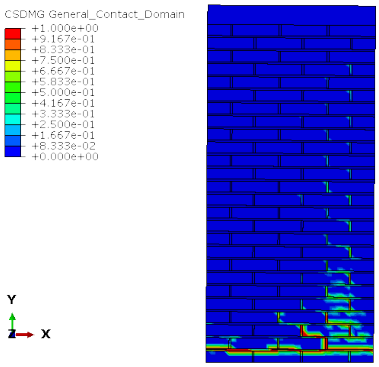

(a) Cohesive damage (CD), drift $\approx 0.6\%$.

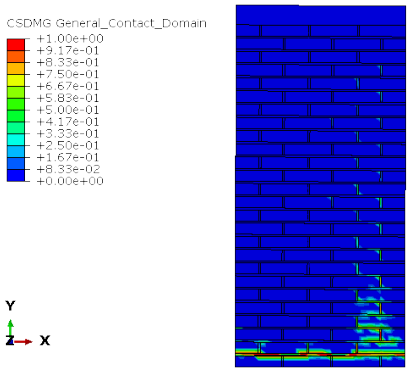

(b) Cohesive damage (CD), peak state ($V_{\max}$).

Figure D.24: Fired brick slender wall, cantilever, high pre-compression: cohesive damage (CD) at drift $\approx 0.6\%$ and at peak state, $V_{\max}$.

D.2 CSEB URM

D.2.1 Squat wall

Fixed-Fixed

Low Pre-Compression

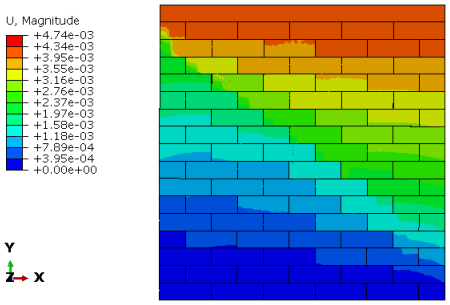

(a) U (Displacement)

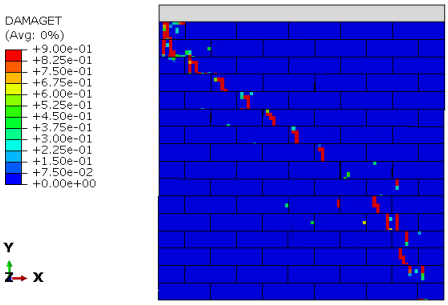

(b) d_t (DAMAGET)

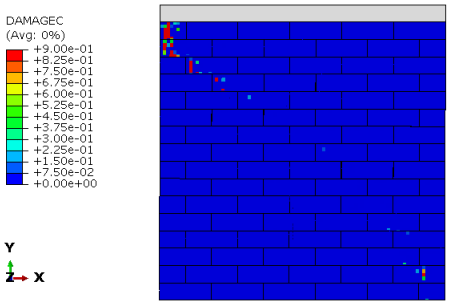

(c) d_c (DAMAGEC)

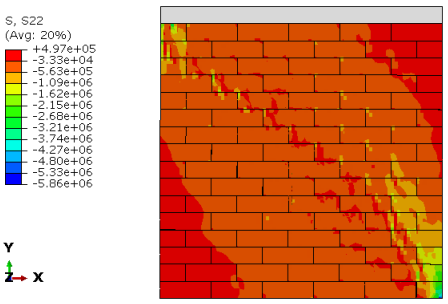

(d) S_{22}

Figure D.25: CSEB URM squat wall, fixed-fixed, low pre-compression: peak state ($V_{\max}$).

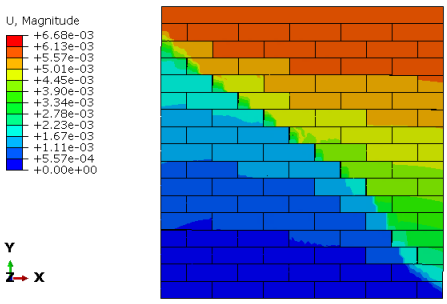

(a) U (Displacement)

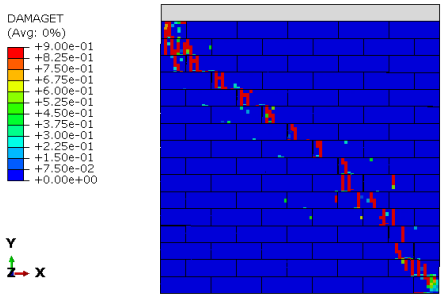

(b) d_t (DAMAGET)

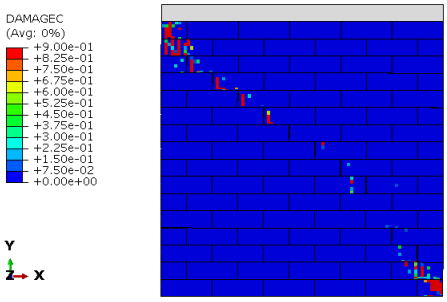

(c) d_c (DAMAGEC)

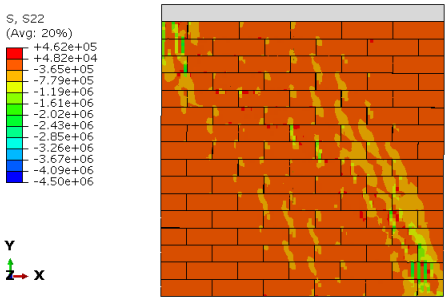

(d) S_{22}

Figure D.26: CSEB URM squat wall, fixed-fixed, low pre-compression: V_{80}.

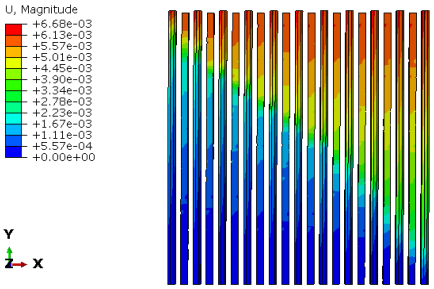

(a) U (Displacement), grout view.

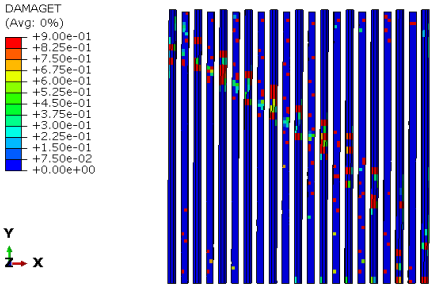

(b) d_t (DAMAGET), grout view.

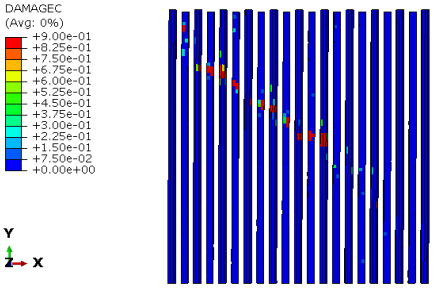

(c) d_c (DAMAGEC), grout view.

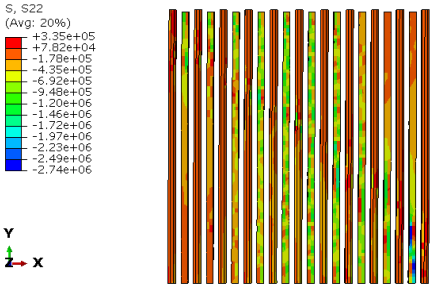

(d) S_{22}, grout view.

Figure D.27: CSEB URM squat wall, fixed-fixed, low pre-compression: grout response at V_{80}.

High Pre-Compression

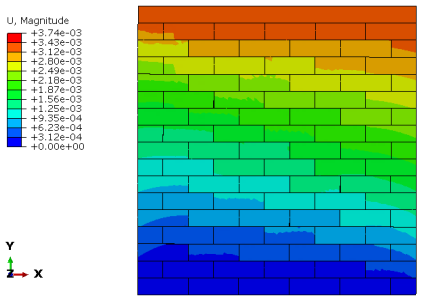

(a) U (Displacement)

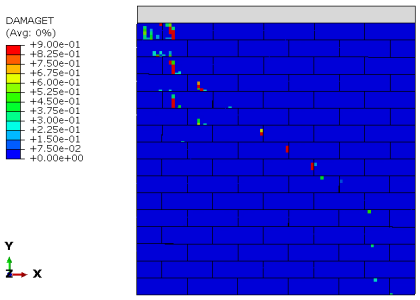

(b) d_t (DAMAGET)

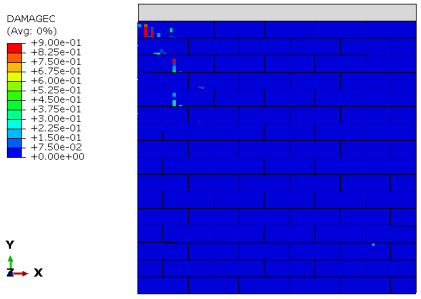

(c) d_c (DAMAGEC)

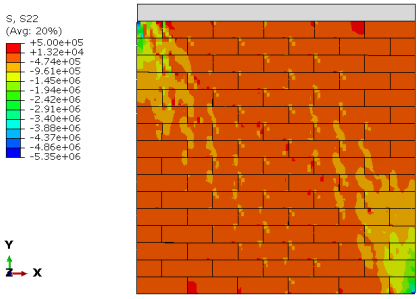

(d) S_{22}

Figure D.28: CSEB URM squat wall, fixed-fixed, high pre-compression: peak state ($V_{\max}$).

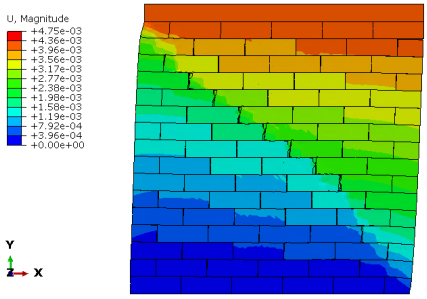

(a) U (Displacement, scaled by factor 20)

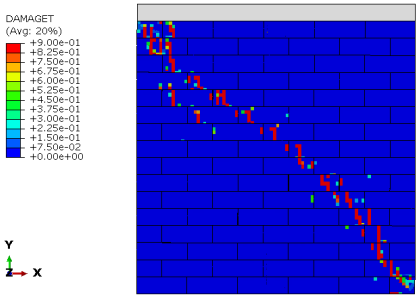

(b) d_t (DAMAGET)

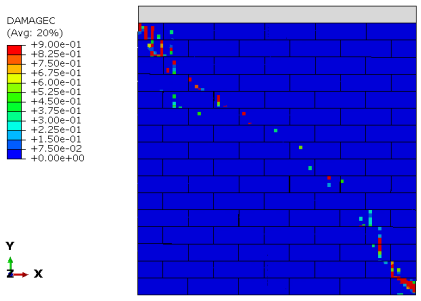

(c) d_c (DAMAGEC)

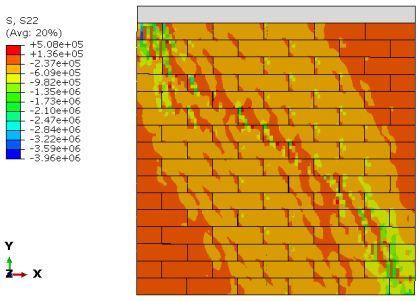

(d) S_{22}

Figure D.29: CSEB URM squat wall, fixed-fixed, high pre-compression: V_{80}.

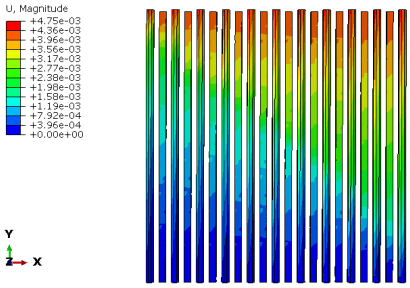

(a) U (Displacement), grout view.

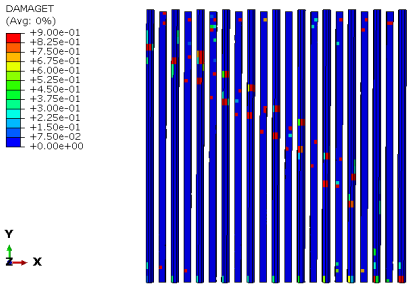

(b) d_t (DAMAGET), grout view.

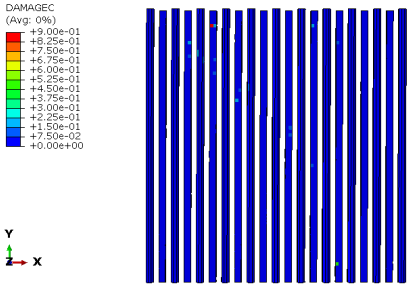

(c) d_c (DAMAGEC), grout view.

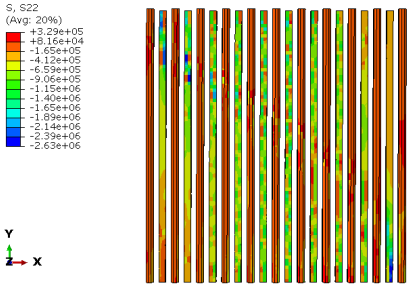

(d) S_{22}, grout view.

Figure D.30: CSEB URM squat wall, fixed-fixed, high pre-compression: grout response at V_{80}.

Cantilever

Low Pre-Compression

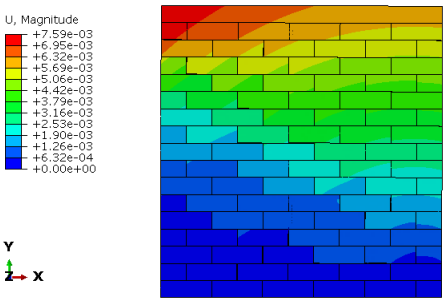

(a) U (Displacement)

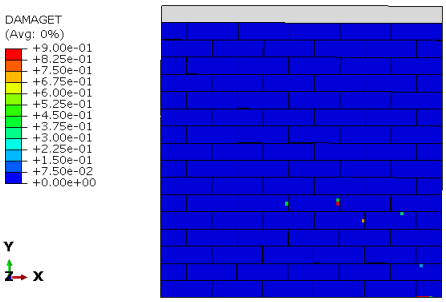

(b) d_t (DAMAGET)

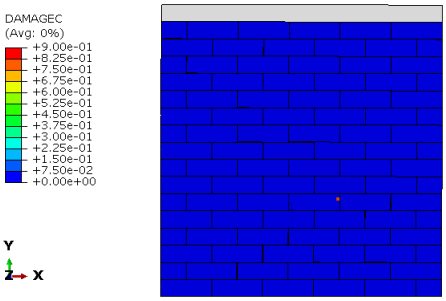

(c) d_c (DAMAGEC)

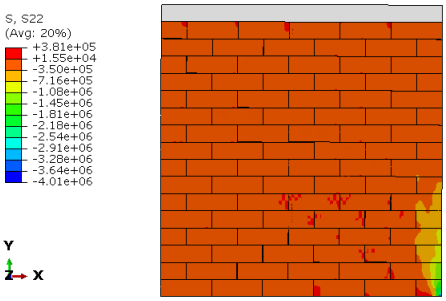

(d) S_{22}

Figure D.31: CSEB URM squat wall, cantilever, low pre-compression: peak state ($V_{\max}$).

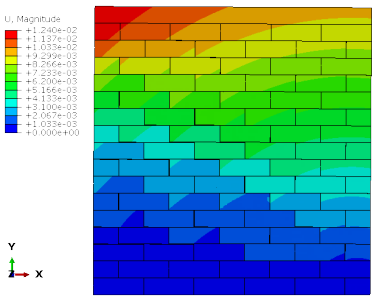

(a) U (Displacement)

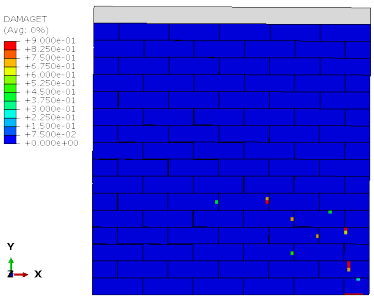

(b) d_t (DAMAGET)

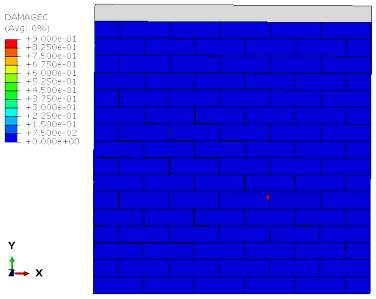

(c) d_c (DAMAGEC)

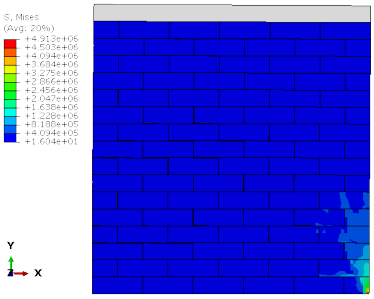

(d) S_{22}

Figure D.32: CSEB URM squat wall, cantilever, low pre-compression: drift 0.6%.

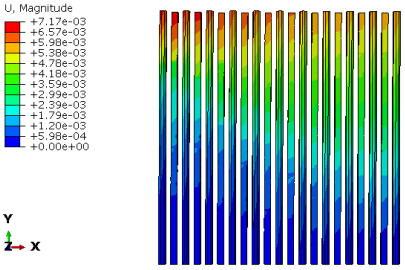

(a) U (Displacement), grout view.

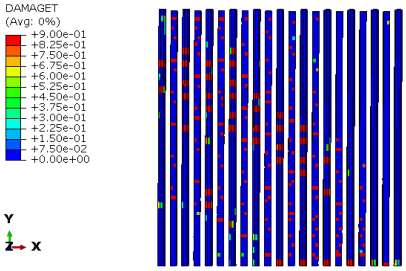

(b) d_t (DAMAGET), grout view.

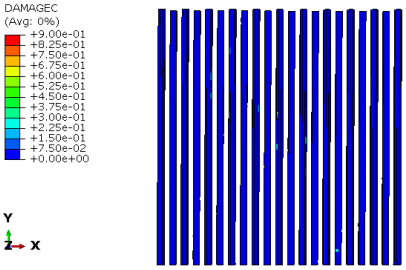

(c) d_c (DAMAGEC), grout view.

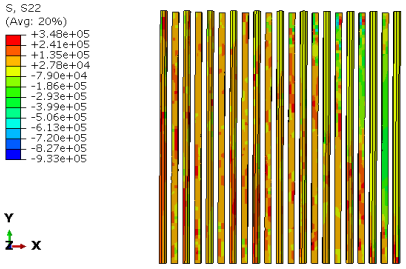

(d) S_{22}, grout view.

Figure D.33: CSEB URM squat wall, cantilever, low pre-compression: grout response at $\approx 0.6\%$.

High Pre-Compression

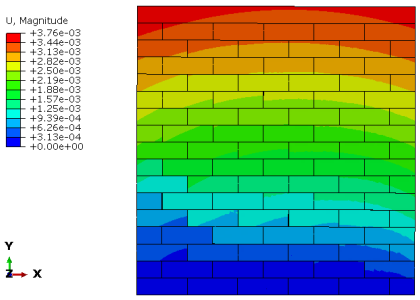

(a) U (Displacement)

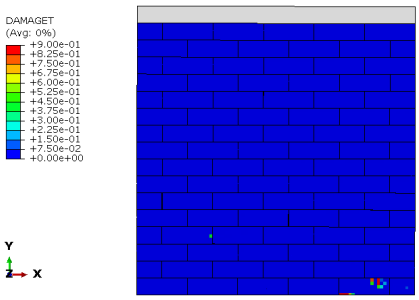

(b) d_t (DAMAGET)

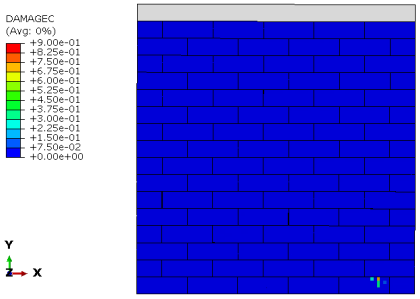

(c) d_c (DAMAGEC)

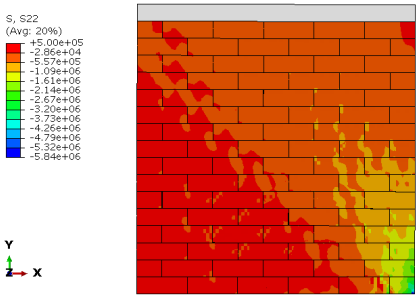

(d) S_{22}

Figure D.34: CSEB URM squat wall, cantilever, high pre-compression: peak state ($V_{\max}$).

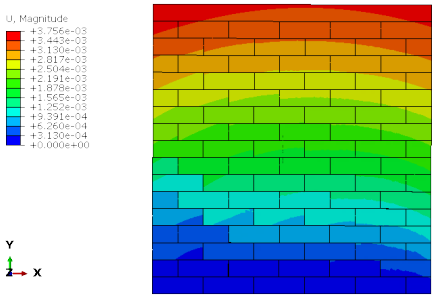

(a) U (Displacement)

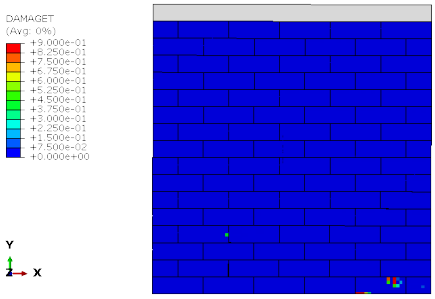

(b) d_t (DAMAGET)

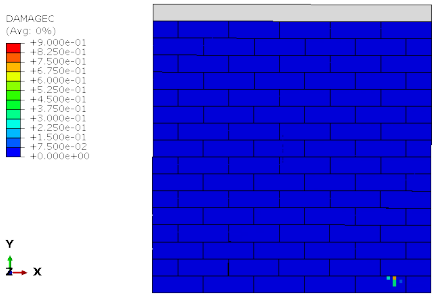

(c) d_c (DAMAGEC)

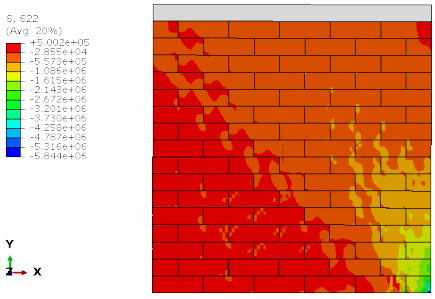

(d) S_{22}

Figure D.35: CSEB URM squat wall, cantilever, high pre-compression: V_{80}.

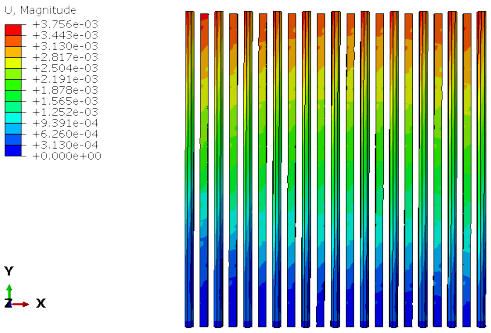

(a) U (Displacement), grout view.

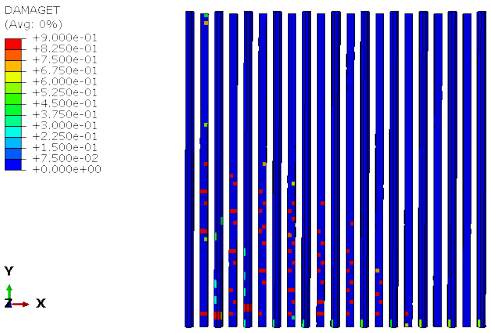

(b) d_t (DAMAGET), grout view.

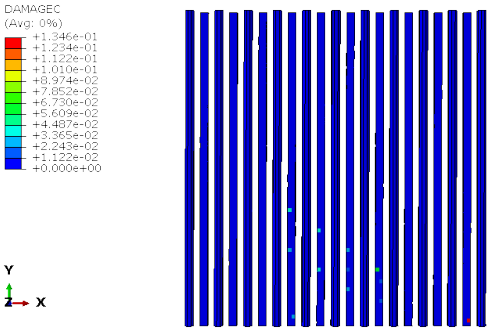

(c) d_c (DAMAGEC), grout view.

(d) S_{22}, grout view.

Figure D.36: CSEB URM squat wall, cantilever, high pre-compression: grout response at V_{80}.

D.2.2 Slender wall

Fixed-Fixed

Low Pre-Compression

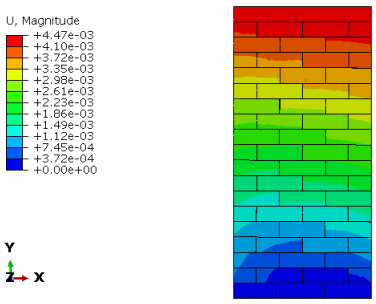

(a) U (Displacement)

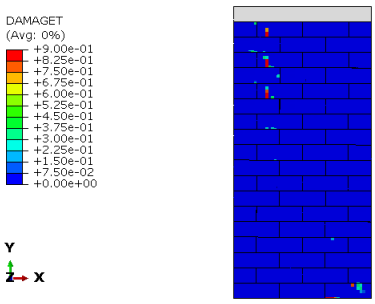

(b) d_t (DAMAGET)

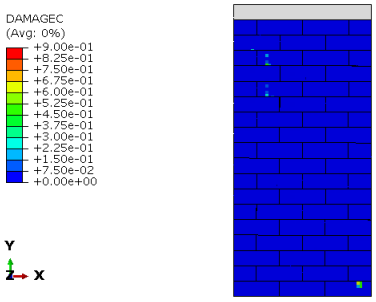

(c) d_c (DAMAGEC)

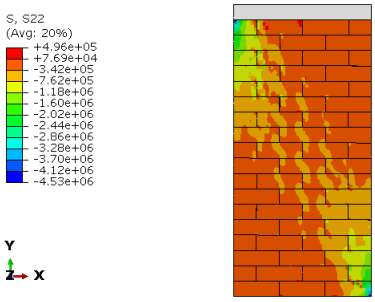

(d) S_{22}

Figure D.37: CSEB URM slender wall, fixed-fixed, low pre-compression: peak state ($V_{\max}$).

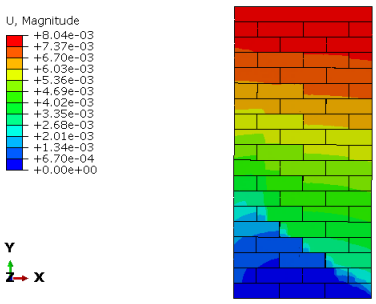

(a) U (Displacement)

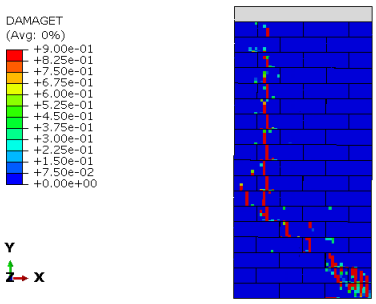

(b) d_t (DAMAGET)

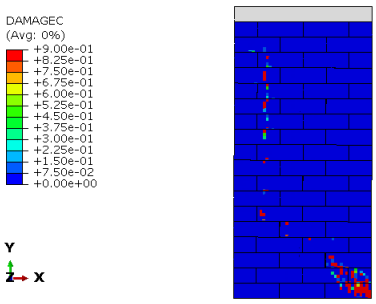

(c) d_c (DAMAGEC)

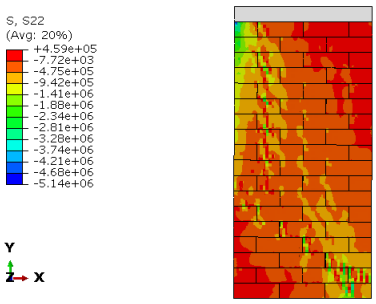

(d) S_{22}

Figure D.38: CSEB URM slender wall, fixed-fixed, low pre-compression: V_{80}.

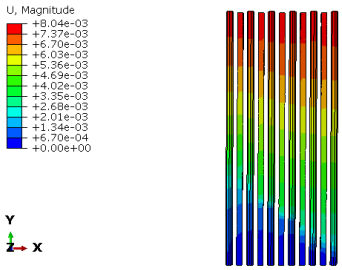

(a) U (Displacement), grout view.

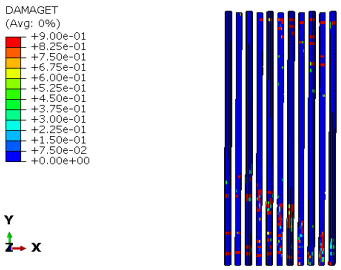

(b) d_t (DAMAGET), grout view.

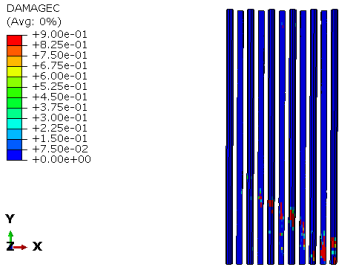

(c) d_c (DAMAGEC), grout view.

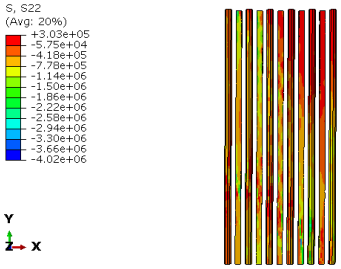

(d) S_{22}, grout view.

Figure D.39: CSEB URM slender wall, fixed-fixed, low pre-compression: grout response at V_{80}.

High Pre-Compression

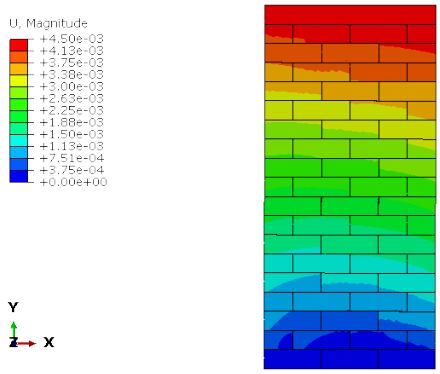

(a) U (Displacement)

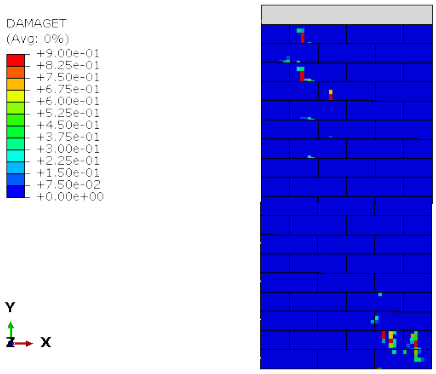

(b) d_t (DAMAGET)

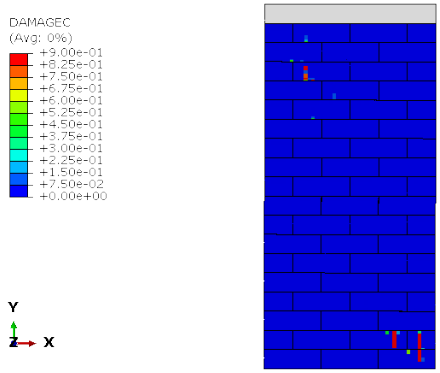

(c) d_c (DAMAGEC)

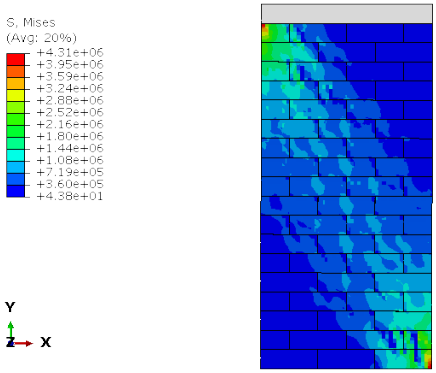

(d) S_{22}

Figure D.40: CSEB URM slender wall, fixed-fixed, high pre-compression: peak state ($V_{\max}$).

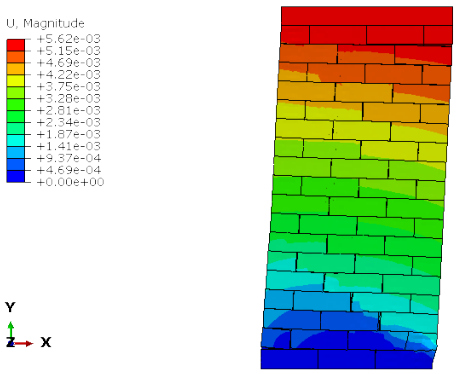

(a) U (Displacement)

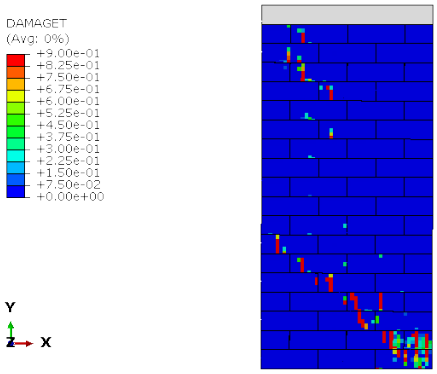

(b) d_t (DAMAGET)

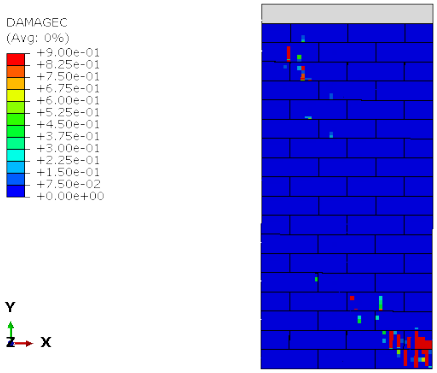

(c) d_c (DAMAGEC)

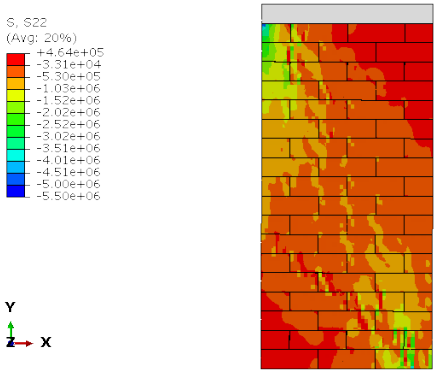

(d) S_{22}

Figure D.41: CSEB URM slender wall, fixed-fixed, high pre-compression: V_{80}.

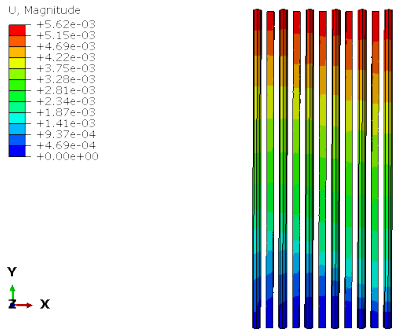

(a) U (Displacement), grout view.

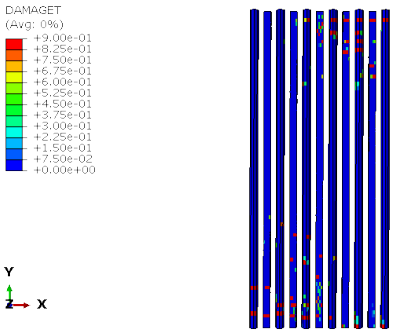

(b) d_t (DAMAGET), grout view.

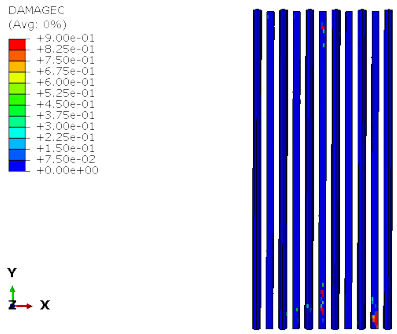

(c) d_c (DAMAGEC), grout view.

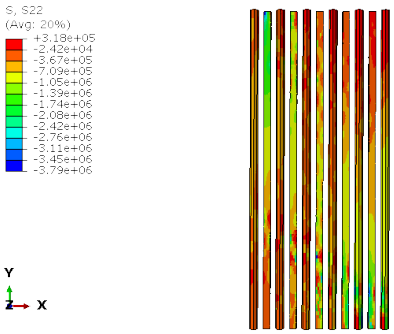

(d) S_{22}, grout view.

Figure D.42: CSEB URM slender wall, fixed-fixed, high pre-compression: grout response at V_{80}.

Cantilever

Low Pre-Compression

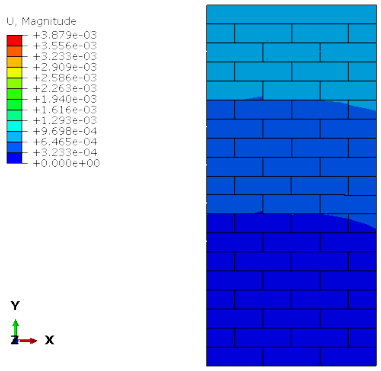

(a) U (Displacement)

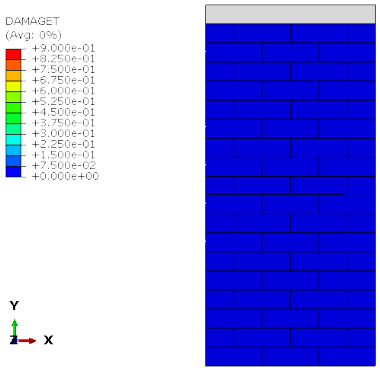

(b) d_t (DAMAGET)

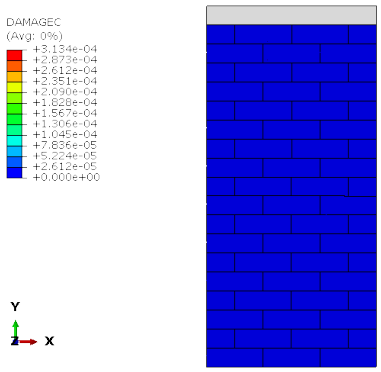

(c) d_c (DAMAGEC)

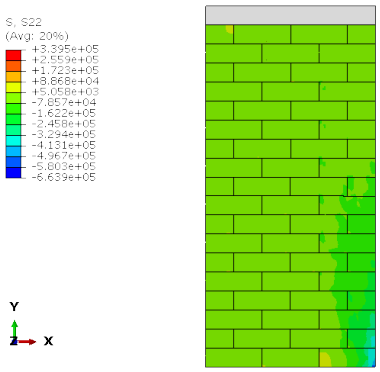

(d) S_{22}

Figure D.43: CSEB URM slender wall, cantilever, low pre-compression: peak state ($V_{\max}$).

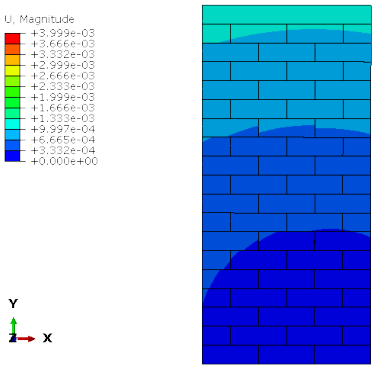

(a) U (Displacement)

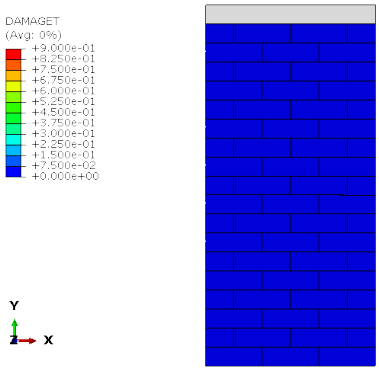

(b) d_t (DAMAGET)

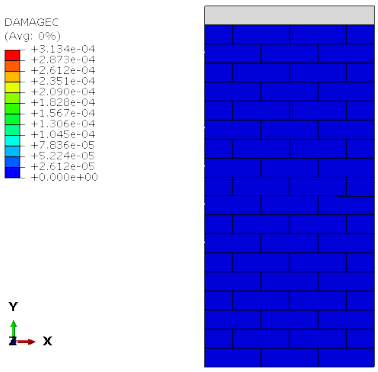

(c) d_c (DAMAGEC)

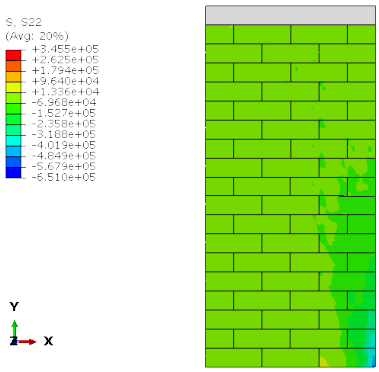

(d) S_{22}

Figure D.44: CSEB URM slender wall, cantilever, low pre-compression: V_{80}.

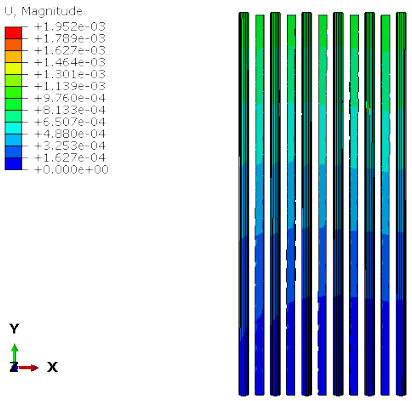

(a) U (Displacement), grout view.

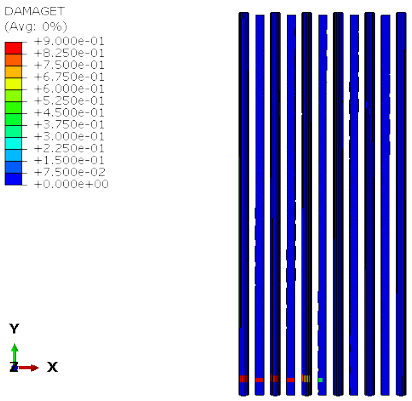

(b) d_t (DAMAGET), grout view.

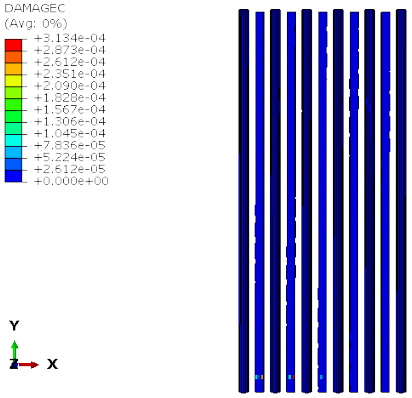

(c) d_c (DAMAGEC), grout view.

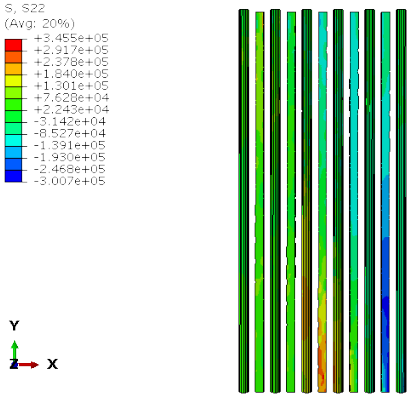

(d) S_{22}, grout view.

Figure D.45: CSEB URM slender wall, cantilever, low pre-compression: grout response at V_{80}.

High Pre-Compression

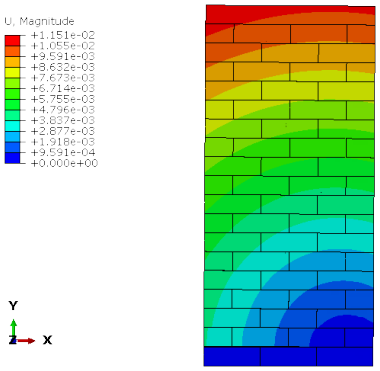

(a) U (Displacement)

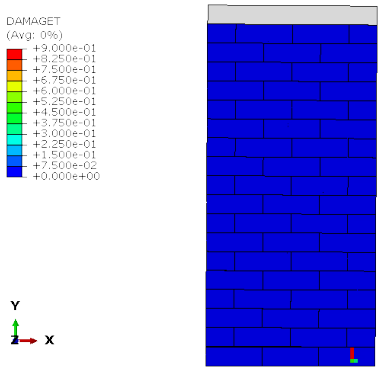

(b) d_t (DAMAGET)

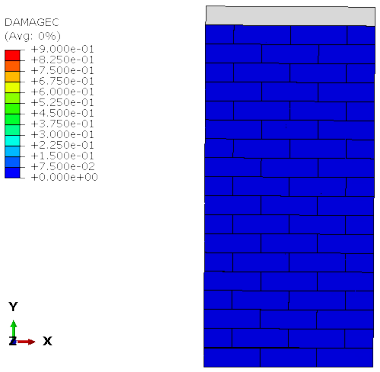

(c) d_c (DAMAGEC)

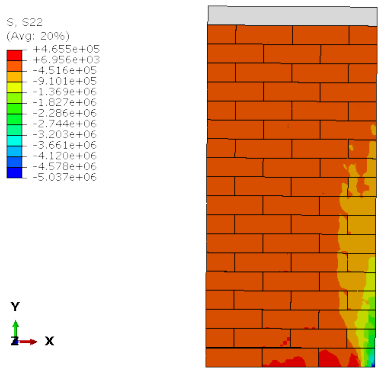

(d) S_{22}

Figure D.46: CSEB URM slender wall, cantilever, high pre-compression: response at peak load and at 0.6% drift. Since the failure pattern remained essentially unchanged after the peak load, only one set of figures is shown.

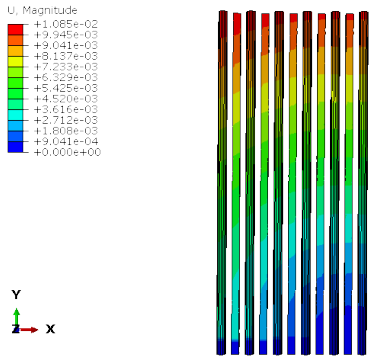

(a) U (Displacement), grout view.

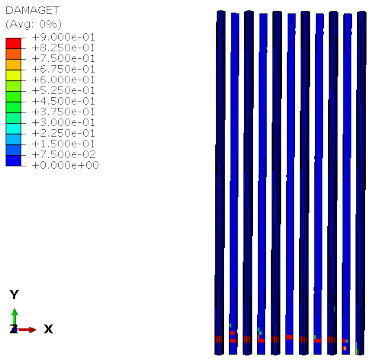

(b) d_t (DAMAGET), grout view.

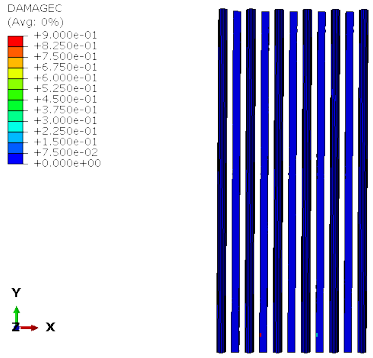

(c) d_c (DAMAGEC), grout view.

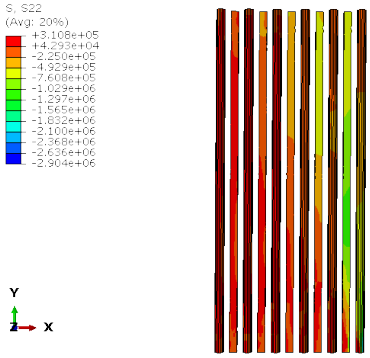

(d) S_{22}, grout view.

Figure D.47: CSEB URM slender wall, cantilever, high pre-compression: grout response at peak load and at 0.6% drift. Since the failure pattern remained essentially unchanged after the peak load, only one set of figures is shown.

D.3 Reinforced CSEB

D.3.1 Squat wall

Fixed-Fixed

Low Pre-Compression

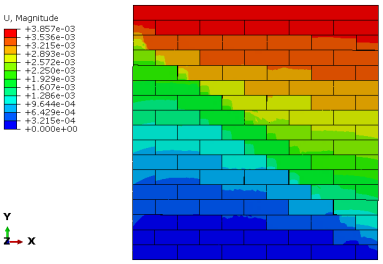

(a) U (Displacement)

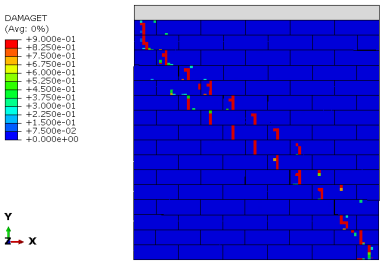

(b) d_t (DAMAGET)

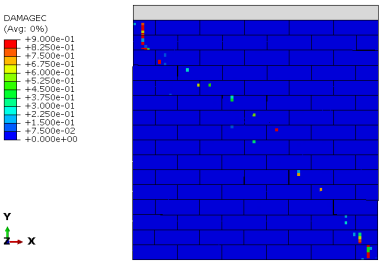

(c) d_c (DAMAGEC)

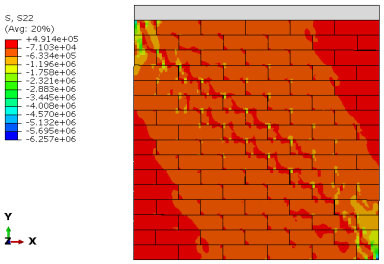

(d) S_{22}

Figure D.48: Reinforced CSEB squat wall, fixed-fixed, low pre-compression: peak state ($V_{\max}$).

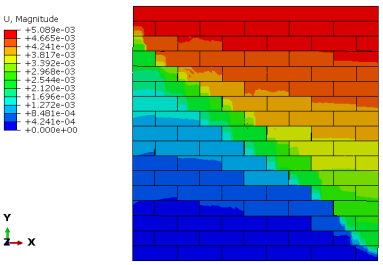

(a) U (Displacement)

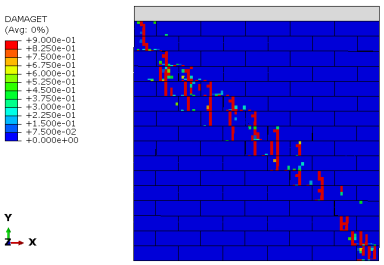

(b) d_t (DAMAGET)

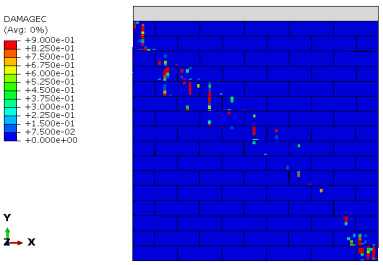

(c) d_c (DAMAGEC)

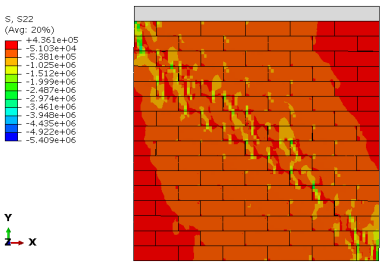

(d) S_{22}

Figure D.49: Reinforced CSEB squat wall, fixed-fixed, low pre-compression: V_{80}.

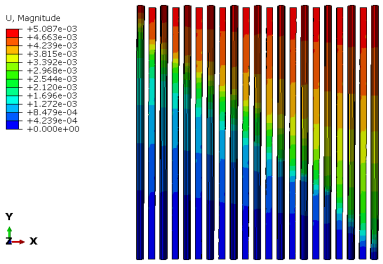

(a) U (Displacement), grout view

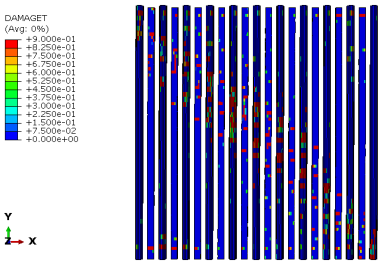

(b) d_t (DAMAGET), grout view

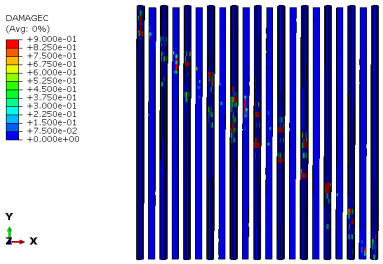

(c) d_c (DAMAGEC), grout view

(d) S_{22}, grout view

Figure D.50: Reinforced CSEB squat wall, fixed-fixed, low pre-compression: grout response at V_{80}.

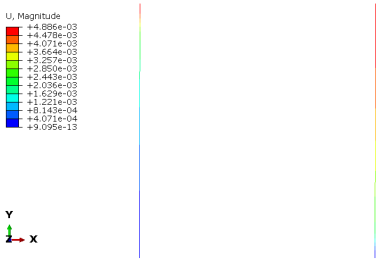

(a) U (Displacement)

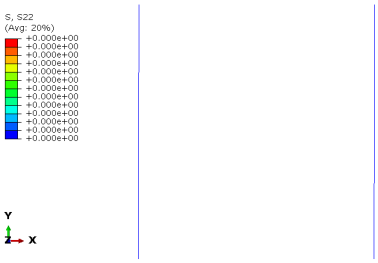

(b) S_{22}

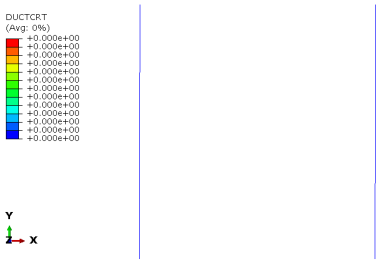

(c) Ductile damage (DUCTCRT)

(d) T_x (steel axial response)

Figure D.51: Reinforced CSEB squat wall, fixed-fixed, low pre-compression: reinforcement response at V_{80}.

High Pre-Compression

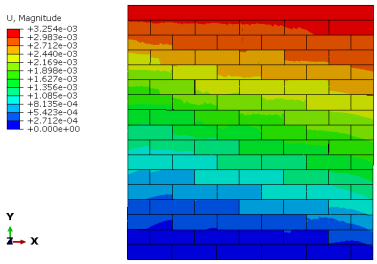

(a) U (Displacement)

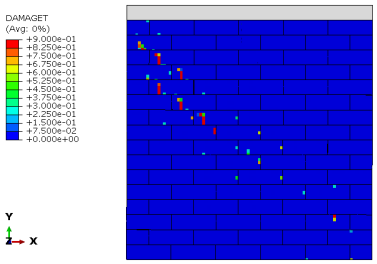

(b) d_t (DAMAGET)

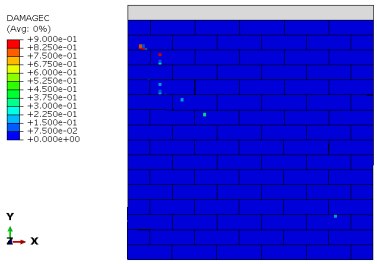

(c) d_c (DAMAGEC)

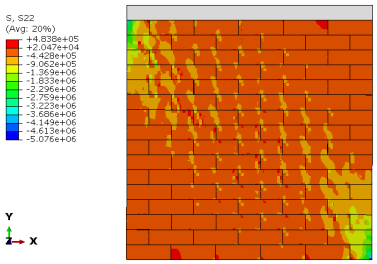

(d) S_{22}

Figure D.52: Reinforced CSEB squat wall, fixed-fixed, high pre-compression: peak state ($V_{\max}$).

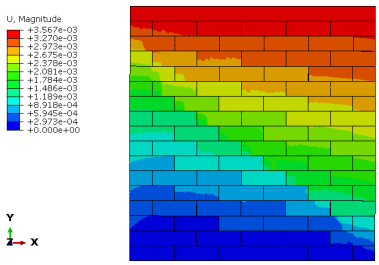

(a) U (Displacement)

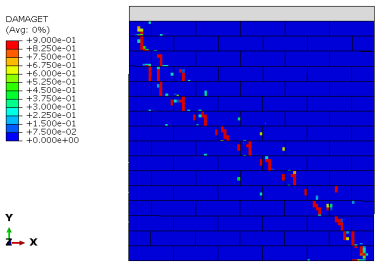

(b) d_t (DAMAGET)

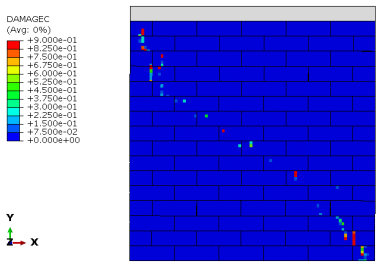

(c) d_c (DAMAGEC)

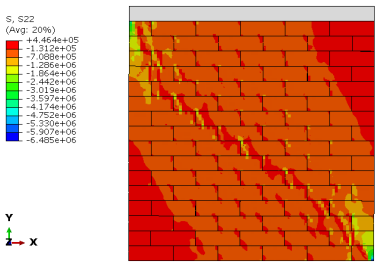

(d) S_{22}

Figure D.53: Reinforced CSEB squat wall, fixed-fixed, high pre-compression: V_{80}.

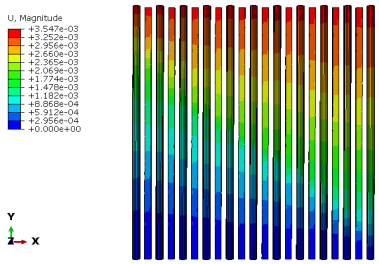

(a) U (Displacement), grout view

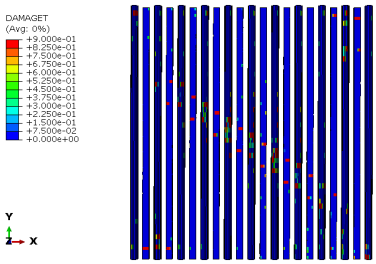

(b) d_t (DAMAGET), grout view

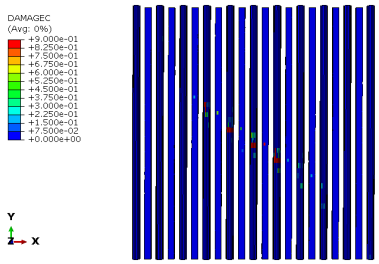

(c) d_c (DAMAGEC), grout view

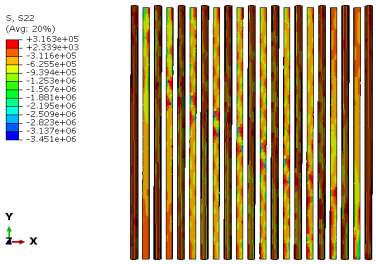

(d) S_{22}, grout view

Figure D.54: Reinforced CSEB squat wall, fixed-fixed, high pre-compression: grout response at V_{80}.

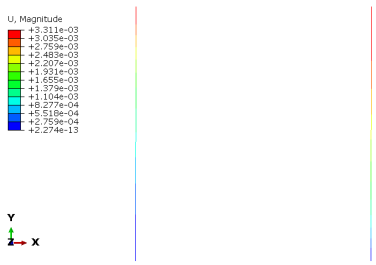

(a) U (Displacement)

(b) S_{22}

(c) Ductile damage (DUCTCRT)

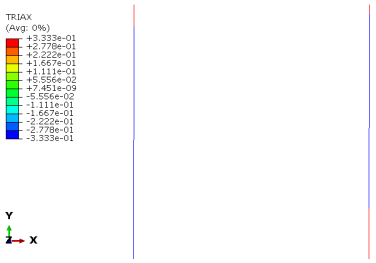

(d) T_x (steel axial response)

Figure D.55: Reinforced CSEB squat wall, fixed-fixed, high pre-compression: reinforcement response at V_{80}.

Cantilever

Low Pre-Compression

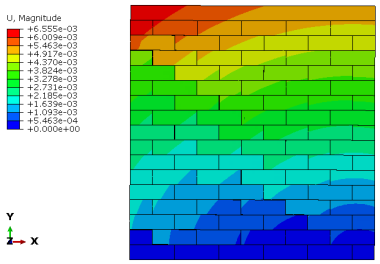

(a) U (Displacement)

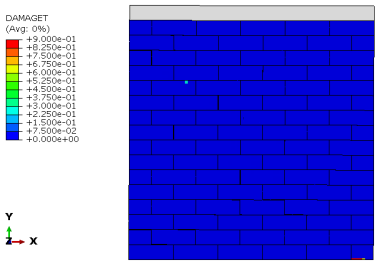

(b) d_t (DAMAGET)

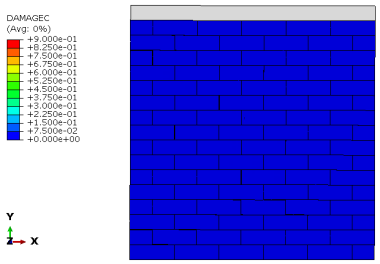

(c) d_c (DAMAGEC)

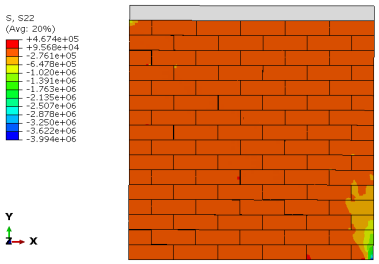

(d) S_{22}

Figure D.56: Reinforced CSEB squat wall, cantilever, low pre-compression: peak state ($V_{\max}$).

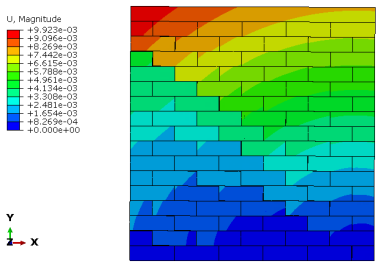

(a) U (Displacement)

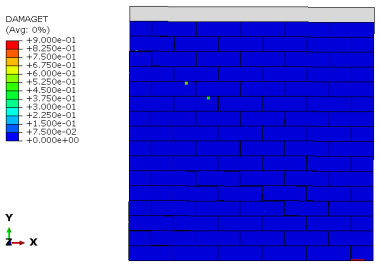

(b) d_t (DAMAGET)

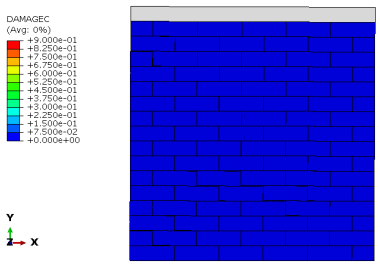

(c) d_c (DAMAGEC)

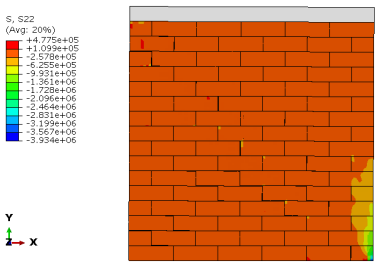

(d) S_{22}

Figure D.57: Reinforced CSEB squat wall, cantilever, low pre-compression: V_{80}.

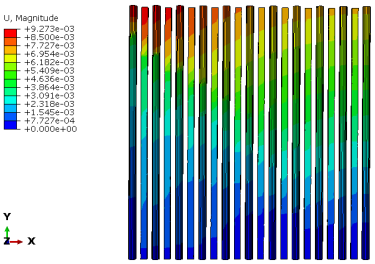

(a) U (Displacement), grout view

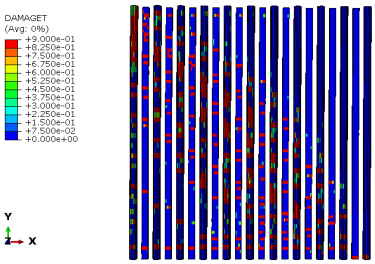

(b) d_t (DAMAGET), grout view

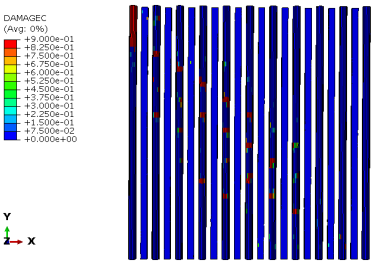

(c) d_c (DAMAGEC), grout view

(d) S_{22}, grout view

Figure D.58: Reinforced CSEB squat wall, cantilever, low pre-compression: grout response at V_{80}.

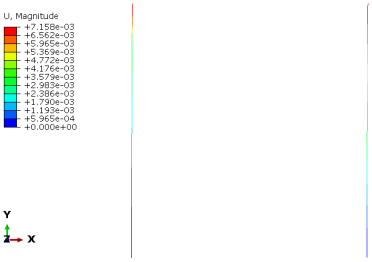

(a) U (Displacement)

(b) S_{22}

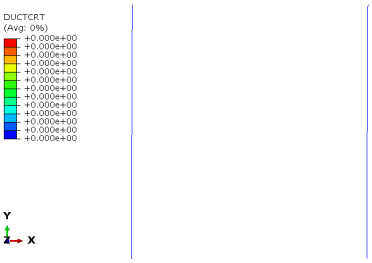

(c) Ductile damage (DUCTCRT)

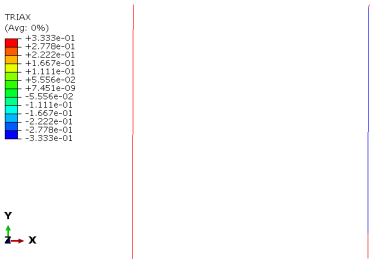

(d) T_x (steel axial response)

Figure D.59: Reinforced CSEB squat wall, cantilever, low pre-compression: reinforcement response at V_{80}.

High Pre-Compression

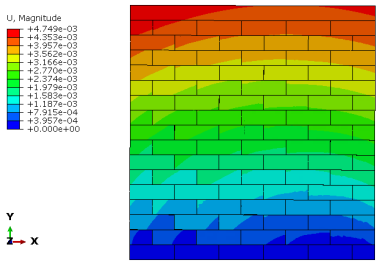

(a) U (Displacement)

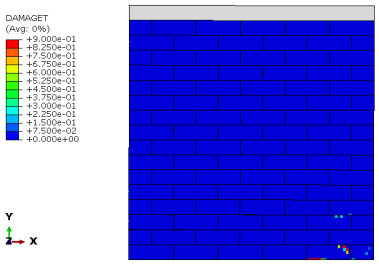

(b) d_t (DAMAGET)

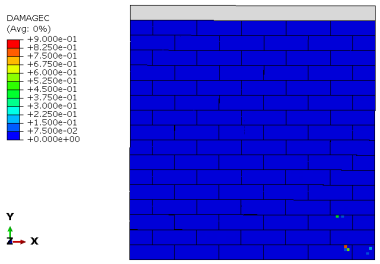

(c) d_c (DAMAGEC)

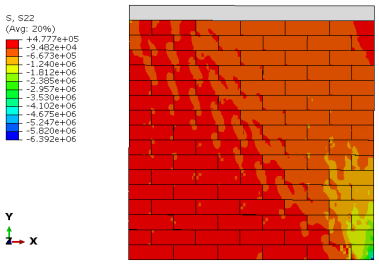

(d) S_{22}

Figure D.60: Reinforced CSEB squat wall, cantilever, high pre-compression: peak state ($V_{\max}$).

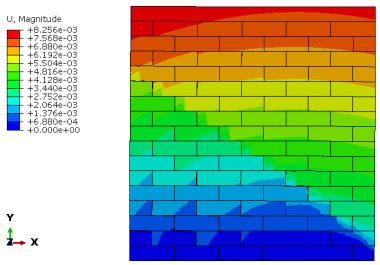

(a) U (Displacement)

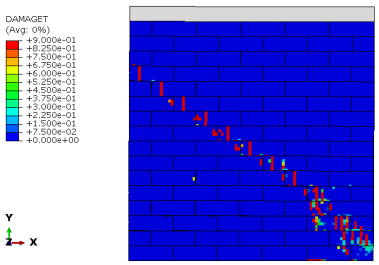

(b) d_t (DAMAGET)

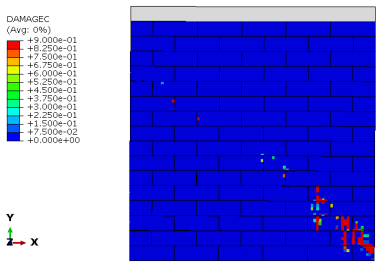

(c) d_c (DAMAGEC)

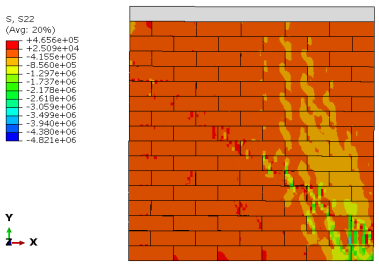

(d) S_{22}

Figure D.61: Reinforced CSEB squat wall, cantilever, high pre-compression: V_{80}.

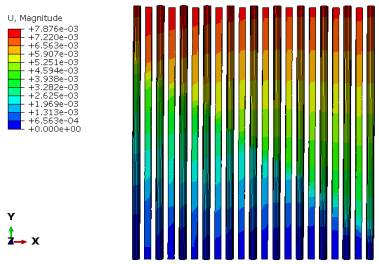

(a) U (Displacement), grout view

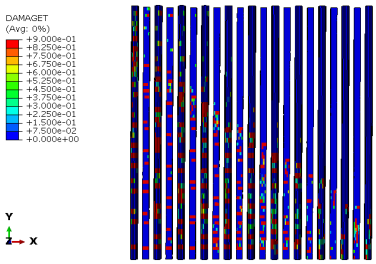

(b) d_t (DAMAGET), grout view

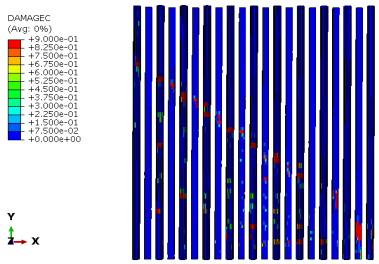

(c) d_c (DAMAGEC), grout view

(d) S_{22}, grout view

Figure D.62: Reinforced CSEB squat wall, cantilever, high pre-compression: grout response at V_{80}.

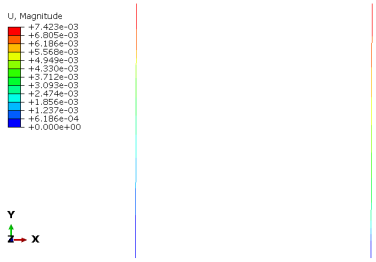

(a) U (Displacement)

(b) S_{22}

(c) Ductile damage (DUCTCRT)

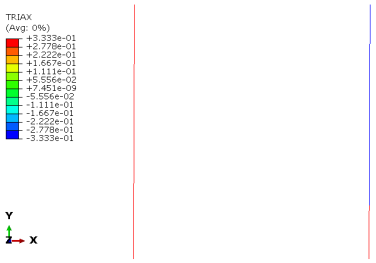

(d) T_x (steel axial response)

Figure D.63: Reinforced CSEB squat wall, cantilever, high pre-compression: reinforcement response at V_{80}.

D.3.2 Slender wall

Fixed-Fixed

Low Pre-Compression

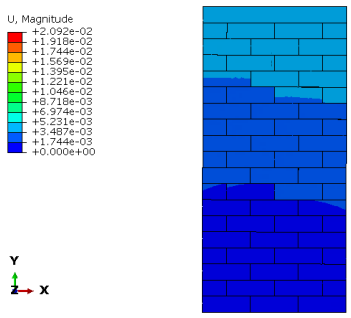

(a) U (Displacement)

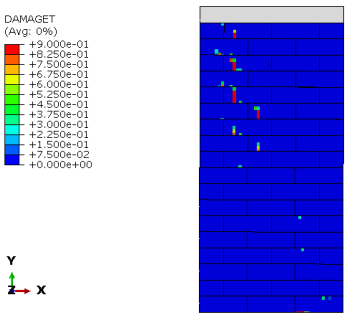

(b) d_t (DAMAGET)

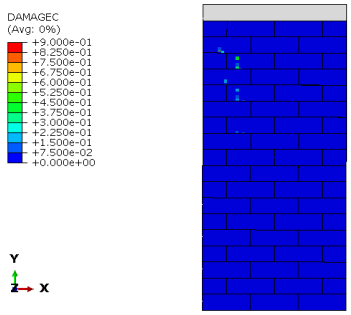

(c) d_c (DAMAGEC)

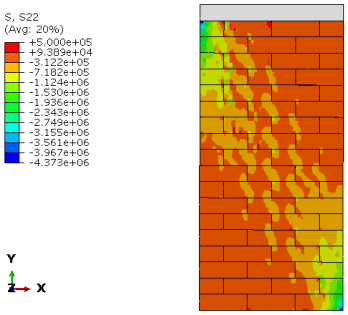

(d) S_{22}

Figure D.64: Reinforced CSEB slender wall, fixed-fixed, low pre-compression: peak state ($V_{\max}$).

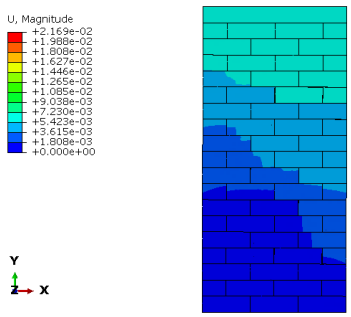

(a) U (Displacement)

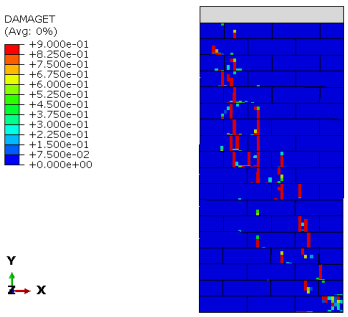

(b) d_t (DAMAGET)

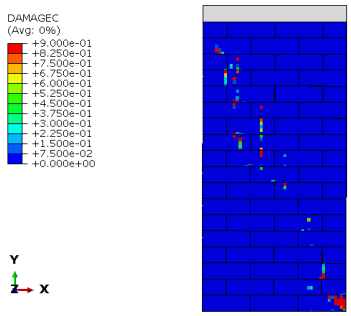

(c) d_c (DAMAGEC)

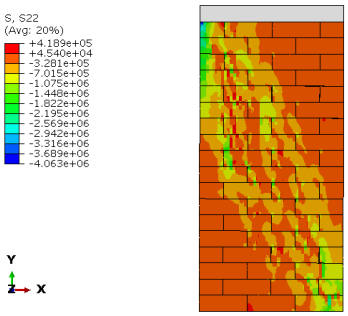

(d) S_{22}

Figure D.65: Reinforced CSEB slender wall, fixed-fixed, low pre-compression: V_{80}.

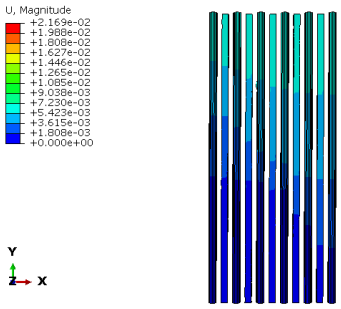

(a) U (Displacement), grout view

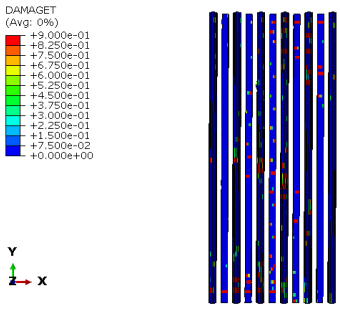

(b) d_t (DAMAGET), grout view

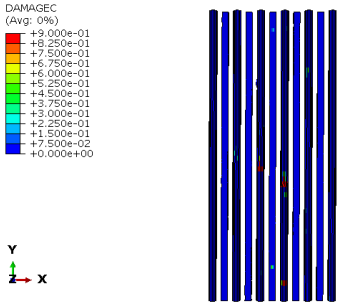

(c) d_c (DAMAGEC), grout view

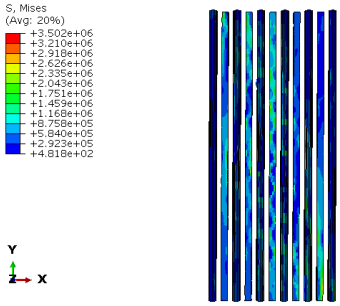

(d) S_{22}, grout view

Figure D.66: Reinforced CSEB slender wall, fixed-fixed, low pre-compression: grout response at V_{80}.

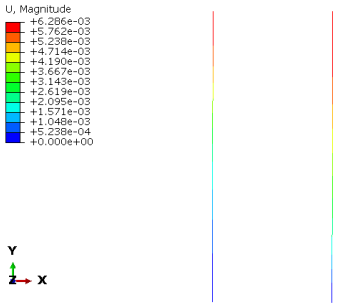

(a) U (Displacement)

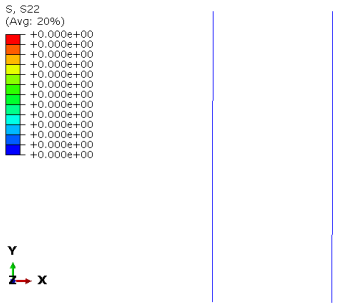

(b) S_{22}

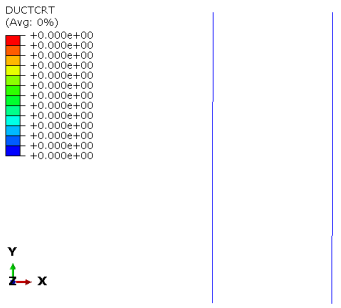

(c) Ductile damage (DUCTCRT)

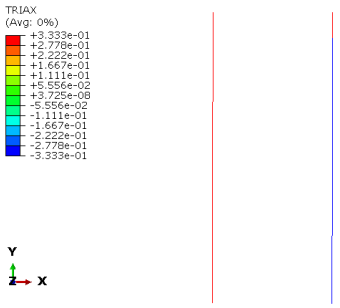

(d) T_x (steel axial response)

Figure D.67: Reinforced CSEB slender wall, fixed-fixed, low pre-compression: reinforcement response at V_{80}.

High Pre-Compression

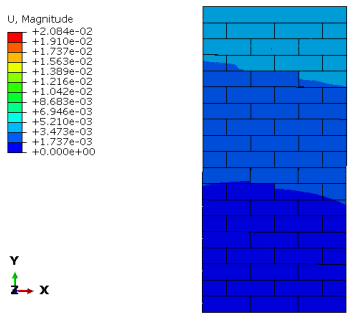

(a) U (Displacement)

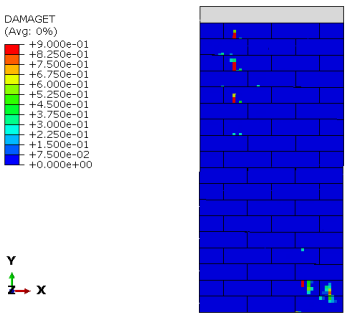

(b) d_t (DAMAGET)

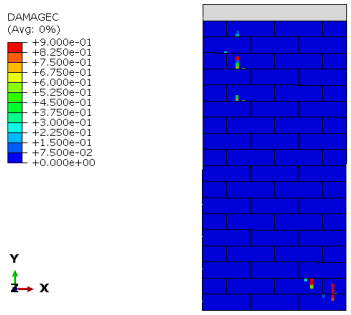

(c) d_c (DAMAGEC)

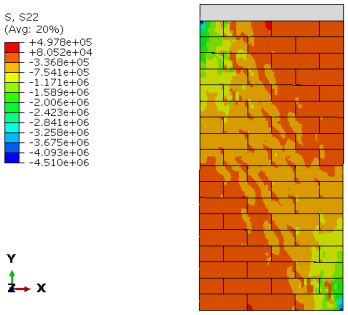

(d) S_{22}

Figure D.68: Reinforced CSEB slender wall, fixed-fixed, high pre-compression: peak state ($V_{\max}$).

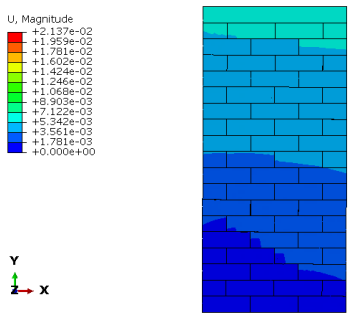

(a) U (Displacement)

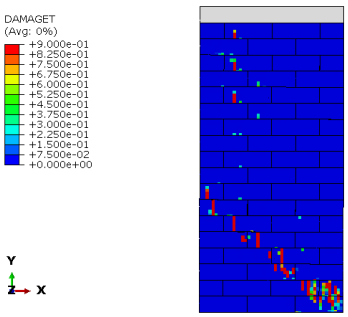

(b) d_t (DAMAGET)

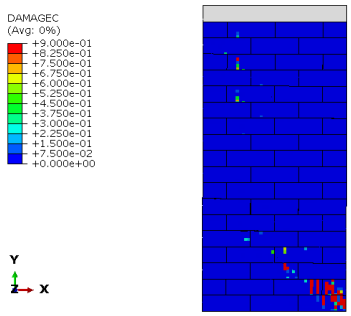

(c) d_c (DAMAGEC)

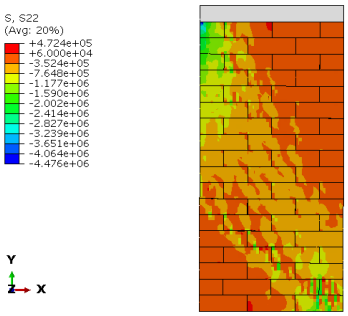

(d) S_{22}

Figure D.69: Reinforced CSEB slender wall, fixed-fixed, high pre-compression: V_{80}.

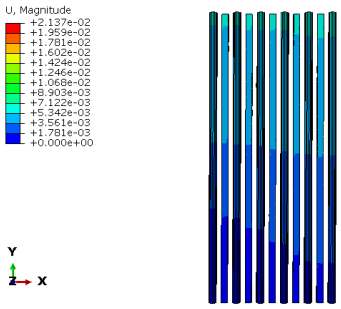

(a) U (Displacement), grout view

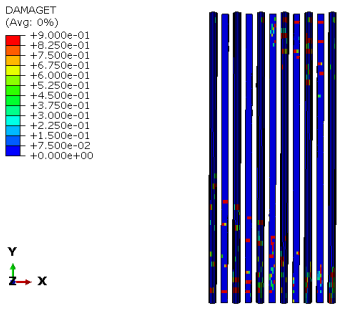

(b) d_t (DAMAGET), grout view

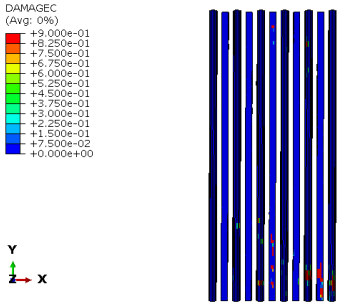

(c) d_c (DAMAGEC), grout view

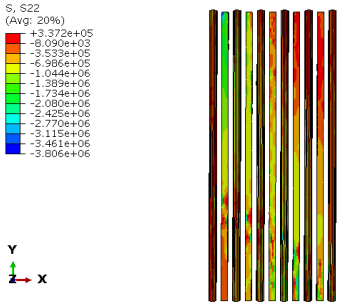

(d) S_{22}, grout view

Figure D.70: Reinforced CSEB slender wall, fixed-fixed, high pre-compression: grout response at V_{80}.

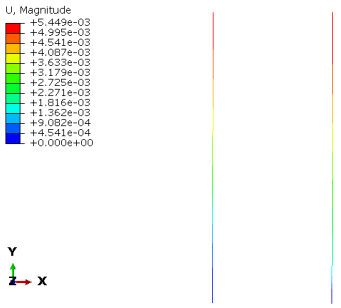

(a) U (Displacement)

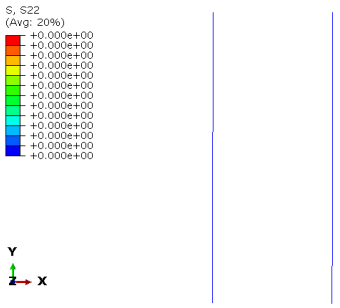

(b) S_{22}

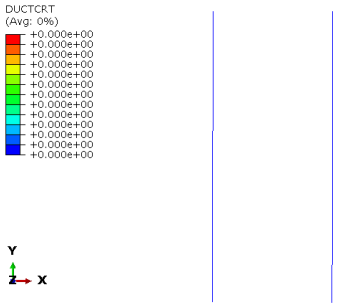

(c) Ductile damage (DUCTCRT)

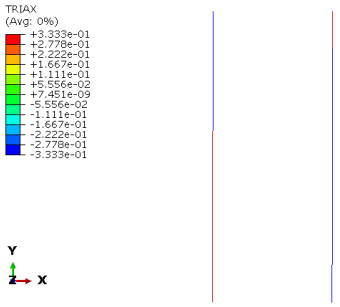

(d) T_x (steel axial response)

Figure D.71: Reinforced CSEB slender wall, fixed-fixed, high pre-compression: reinforcement response at V_{80}.

Cantilever

Low Pre-Compression

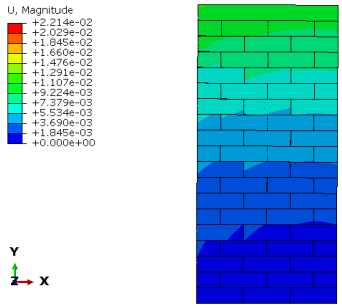

(a) U (Displacement)

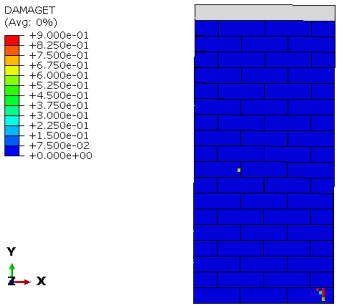

(b) d_t (DAMAGET)

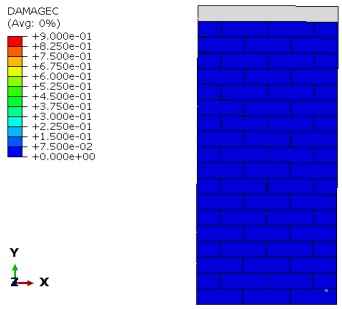

(c) d_c (DAMAGEC)

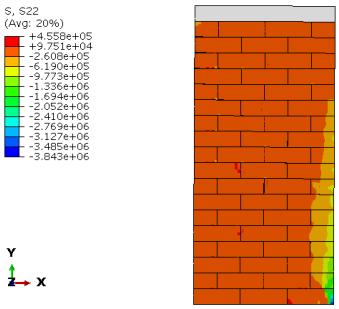

(d) S_{22}

Figure D.72: Reinforced CSEB slender wall, cantilever, low pre-compression: peak state ($V_{\max}$).

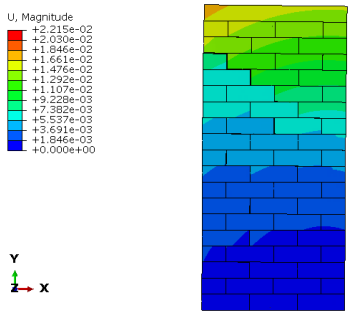

(a) U (Displacement)

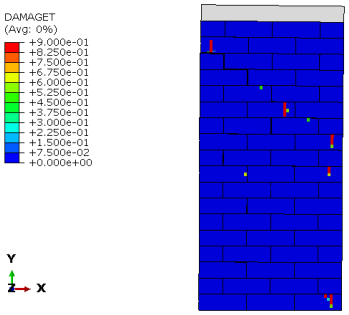

(b) d_t (DAMAGET)

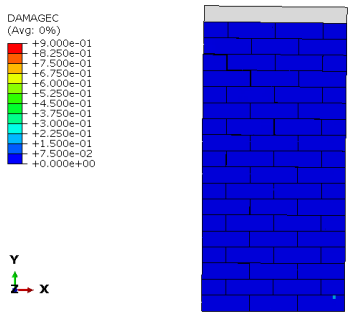

(c) d_c (DAMAGEC)

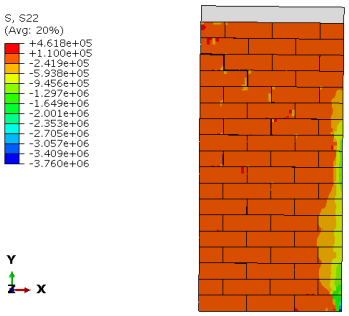

(d) S_{22}

Figure D.73: Reinforced CSEB slender wall, cantilever, low pre-compression: V_{80}.

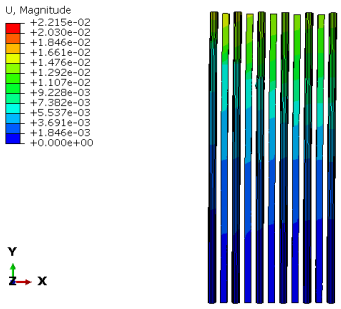

(a) U (Displacement), grout view

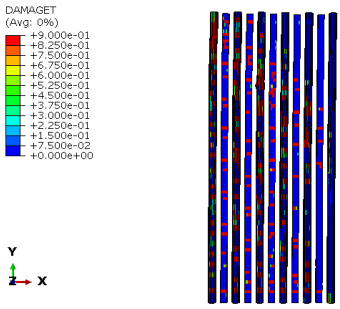

(b) d_t (DAMAGET), grout view

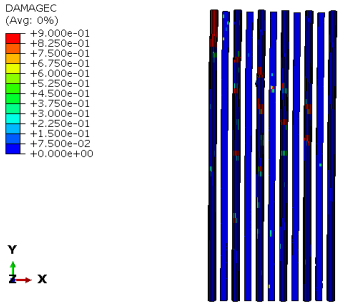

(c) d_c (DAMAGEC), grout view

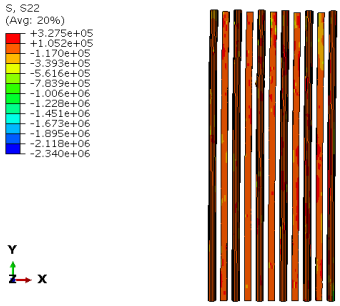

(d) S_{22}, grout view

Figure D.74: Reinforced CSEB slender wall, cantilever, low pre-compression: grout response at V_{80}.

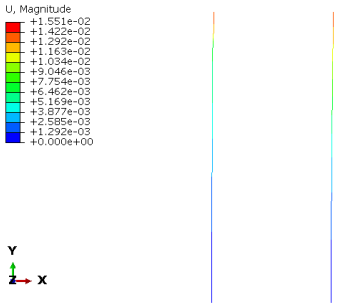

(a) U (Displacement)

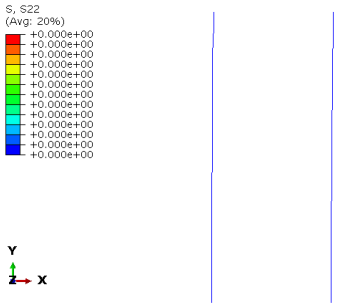

(b) S_{22}

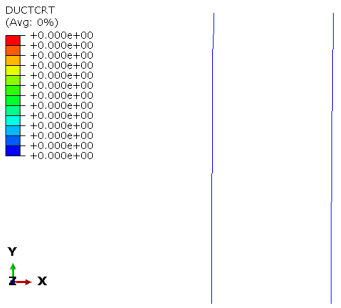

(c) Ductile damage (DUCTCRT)

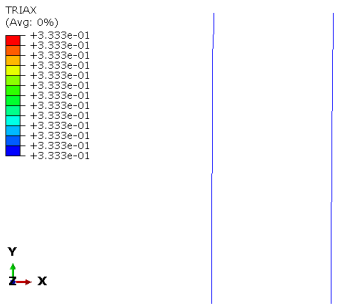

(d) T_x (steel axial response)

Figure D.75: Reinforced CSEB slender wall, cantilever, low pre-compression: reinforcement response at V_{80}.

High Pre-Compression

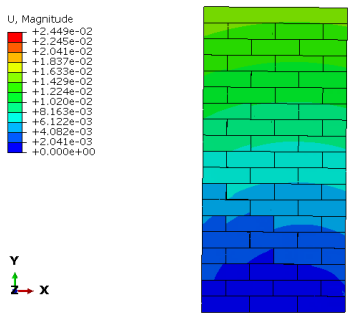

(a) U (Displacement)

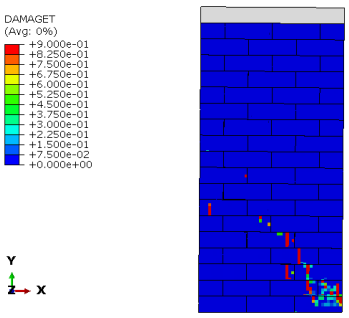

(b) d_t (DAMAGET)

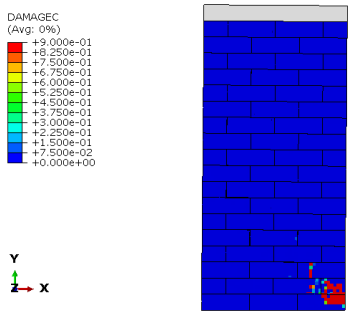

(c) d_c (DAMAGEC)

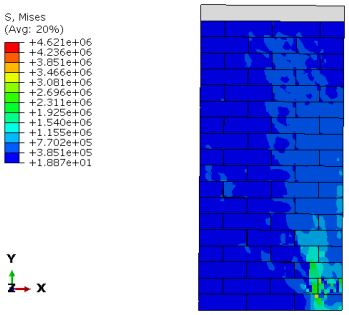

(d) S_{22}

Figure D.76: Reinforced CSEB slender wall, cantilever, high pre-compression: peak state ($V_{\max}$).

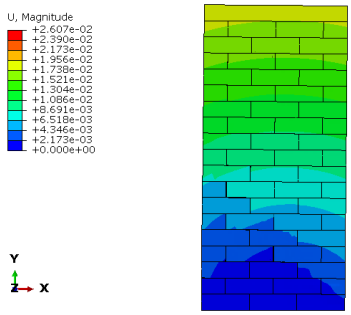

(a) U (Displacement)

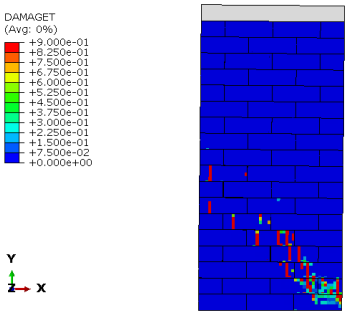

(b) d_t (DAMAGET)

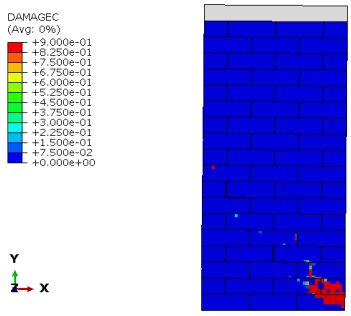

(c) d_c (DAMAGEC)

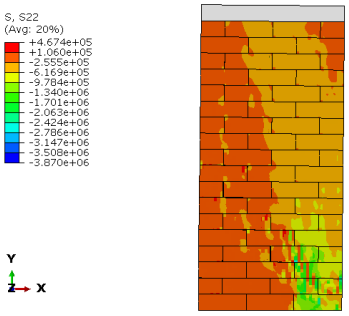

(d) S_{22}

Figure D.77: Reinforced CSEB slender wall, cantilever, high pre-compression: V_{80}.

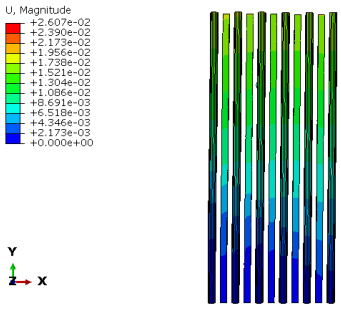

(a) U (Displacement), grout view

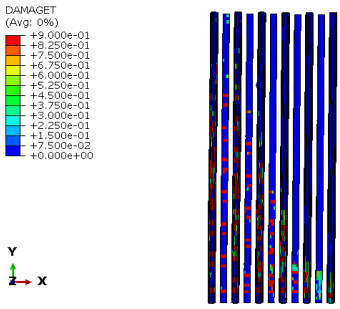

(b) d_t (DAMAGET), grout view

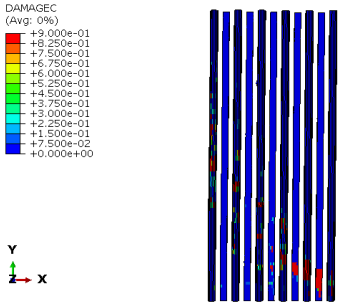

(c) d_c (DAMAGEC), grout view

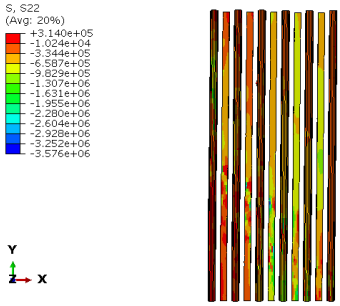

(d) S_{22}, grout view

Figure D.78: Reinforced CSEB slender wall, cantilever, high pre-compression: grout response at V_{80}.

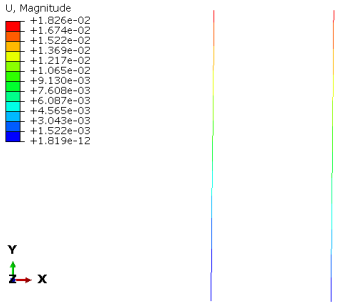

(a) U (Displacement)

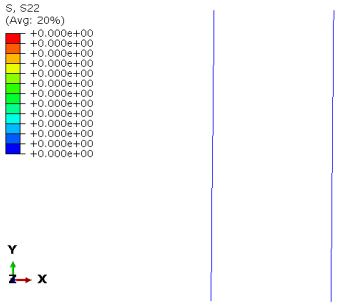

(b) S_{22}

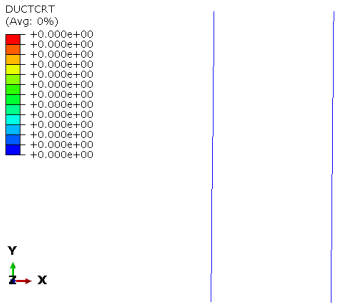

(c) Ductile damage (DUCTCRT)

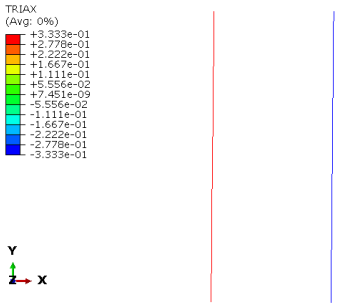

(d) T_x (steel axial response)

Figure D.79: Reinforced CSEB slender wall, cantilever, high pre-compression: reinforcement response at V_{80}.